



**Attitude Control of a Satellite Simulator Using Reaction Wheels and a PID
Controller**

THESIS

Ryan E. Snider, Captain, USAF

AFIT/GAE/ENY/10-M24

DEPARTMENT OF THE AIR FORCE
AIR UNIVERSITY

AIR FORCE INSTITUTE OF TECHNOLOGY

Wright-Patterson Air Force Base, Ohio

APPROVED FOR PUBLIC RELEASE; DISTRIBUTION UNLIMITED.

The views expressed in this thesis are those of the author and do not reflect the official policy or position of the United States Air Force, Department of Defense, or the United States Government. This material is declared a work of the U.S. Government and is not subject to copyright protection in the United States.

AFIT/GAE/ENY/10-M24

ATTITUDE CONTROL OF A SATELLITE SIMULATOR USING REACTION WHEELS AND
A PID CONTROLLER

THESIS

Presented to the Faculty
Department of Aeronautics and Astronautics
Graduate School of Engineering and Management
Air Force Institute of Technology
Air University
Air Education and Training Command
In Partial Fulfillment of the Requirements for the
Degree of Master of Science in Aeronautical Engineering

Ryan E. Snider, BS
Captain, USAF

March 2010

APPROVED FOR PUBLIC RELEASE; DISTRIBUTION UNLIMITED.

AFIT/GAE/ENY/10-M24

ATTITUDE CONTROL OF A SATELLITE SIMULATOR USING REACTION WHEELS AND
A PID CONTROLLER

Ryan E. Snider, BS
Captain, USAF

Approved:



Lt Col Eric Swenson (Chairman)

16 Mar 10

Date



Lt Col Frederick Harmon (Member)

16 Mar 10

Date



Dr. Jonathan Black (Member)

16 MAR 2010

Date

Abstract

Attitude requirements of a satellite are determined by its mission: telecommunications, optical imagery, and meteorology to name a few. A satellite's ability to orient its mission critical hardware (solar arrays, attitude sensors, etc.), as well as its mission specific payload, is incumbent upon the performance of the satellite's attitude control system (ACS). For a highly accurate ACS and for moderately fast maneuverability, reaction wheels are preferred because they allow continuous and smooth control while inducing the smallest possible disturbance torques.

The objective of this research is to design, build, test, and evaluate the performance of a reaction wheel ACS on-board the Air Force Institute of Technology's (AFIT) second-generation satellite simulator, SimSat II. The reaction wheel ACS is evaluated against performance measures set forth by AFIT faculty; specifically, the ability to perform rest-to-rest maneuvers and withstand worst case disturbance torques.

In all, the reaction wheel ACS proves it is capable of performing rest-to-rest maneuvers and withstanding disturbance torques. However, results conclude that theoretical predicted performance is presently unattainable.

The performance of the reaction wheel ACS hinges upon its ability to command the reaction wheels at fixed interval timing. The inability of the test bed to execute fixed interval timing caused performance degradation.

Acknowledgements

First and foremost I would like to thank the Department of Aeronautics and Astronautics and my thesis advisor, Lt Col Eric Swenson, for allowing someone with the background that I do, a B.S. in mechanical engineering completing an M.S. in aeronautical engineering, to pursue a thesis topic more closely related to astronautical engineering. Overall, this thesis research experience has been challenging yet gratifying and has left an indelible mark on my AFIT education.

The sum total of this effort could never have been completed by me alone. Along the way, many individuals have contributed to the advancement of this research. Whenever frustrated or stumped Lt Col Eric Swenson was there to advise. Sir, I particularly found your lectures that related my troubles to acquisition programs and the contractor–government relationship to be encouraging. I also appreciate the insight you shared on how to troubleshoot hardware and software; the knowledge I acquired is sure to payoff time and time again. Additional thanks goes to Captains Doug McFarland and Chris McChesney. Whether assembling hardware, conducting experiments, or brainstorming on difficult matters, your assistance has enhanced this effort. Last but not least, the men of AFIT/ENWM deserve recognition for making me feel welcome in their machine shop and for educating me on the difficulties of fabricating my engineering designs.

On a personal note, much love and support was provided away from the academic environment that aided in seeing this research through to fruition. To my wife, editor-in-chief, who taught me a thing or two about research writing; I love you and thank you for doing or doing without what I normally take care of. To my son, who was always a great diversion from the stresses of academia; I found pushing a “chooch” round and round the track with you to be highly therapeutic. I’d like to thank my parents for instilling within me the joy of learning and for never saying I wasn’t capable of accomplishing something. Also, I’d like to acknowledge my mother- and father-in-law who helped to make crazy moments in life manageable and for looking after my family at times so that I could have peace and quite to concentrate on my studies. Thank you.

Ryan E. Snider

Table of Contents

	Page
Abstract	iii
Acknowledgements	iv
List of Figures	vii
List of Tables	xi
List of Abbreviations	xii
 I. Introduction	 1
1.1 Background	1
1.2 Problem Statement	2
1.3 Research Objectives	3
1.4 Methodology	3
1.5 Assumptions	4
1.6 Preview	4
 II. Background	 6
2.1 Satellite Simulators	6
2.1.1 Planar Air-Bearing	7
2.1.2 Spherical Air-Bearings	8
2.2 AFIT Satellite Simulators	11
2.3 Spacecraft Dynamics	13
2.3.1 Rigid Body Dynamics	13
2.3.2 Rotation Sequences in \mathbb{R}^3	24
2.3.3 Satellite Three-Axis Control	31
2.4 PID Attitude Control	34
2.5 Summary	36
 III. Methodology	 37
3.1 SimSat II Hardware	37
3.1.1 Ground Station	37
3.1.2 Air Bearing	38
3.1.3 SimSat II	39
3.2 SimSat II Software	45
3.2.1 EPOS User Interface [®]	45
3.2.2 SIMULINK [®]	49
3.2.3 dSPACE ControlDesk [®]	51
3.3 System Interface	52

	Page
3.4 System Characterization	52
3.4.1 Reaction Wheel Sizing	53
3.4.2 Velocity Controller Tuning	57
3.4.3 System Safety Measures	60
3.4.4 Velocity Commanded Schema	63
3.4.5 Center of Mass	71
3.4.6 Mass Moment of Inertia	74
3.4.7 Inertial Measurement Bias	78
3.4.8 PID Tuning	80
3.5 Summary	81
IV. Results and Analysis	82
4.1 Positioning Accuracy	83
4.2 Rest-to-Rest Maneuvers	85
4.2.1 1-Axis Reorientation	86
4.2.2 2-Axis Reorientation	87
4.2.3 3-Axis Reorientation	89
4.2.4 Rest-to-Rest Summary	91
4.3 The Inconsistency of Δt	92
4.4 Disturbance Torques	93
4.4.1 1-Axis Disturbance Torque	94
4.4.2 2-Axis Disturbance Torque	96
4.4.3 3-Axis Disturbance Torque	98
4.4.4 Disturbance Torque Summary	100
V. Conclusions and Recommendations	103
5.1 Conclusions	103
5.2 Recommendations	105
Appendices	107
Appendix A. SimSat II Subsystems	108
A.1 Reaction Wheel Assembly	108
A.1.1 Maxon EC 45 Brushless Motor	108
A.1.2 Maxon HEDL 9140 Encoder	109
A.1.3 Maxon EPOS 70/10 Controller	110
A.2 Northrop Grumman LN-200 IMU	111
Appendix B. Experimental Data	113
B.1 Positioning Accuracy	113
B.2 Rest-to-Rest Maneuvers	115
B.3 Disturbance Torques	129
Bibliography	147

List of Figures

Figure	Page
1.1. SimSat II with Reaction Wheel ACS	3
1.2. SimSat II Assumptions	4
2.1. Two-Link Manipulator Testbed at Stanford University's ARL [43]	7
2.2. Spherical Air-Bearing Motion Constraints Due to Pedestal	8
2.3. Spherical Air-Bearing Styles	10
2.4. SimSat I [19]	12
2.5. SimSat II with Fan Thruster ACS [40]	12
2.6. Definition of \vec{r}_{com}	15
2.7. Distribution of Mass with Respect to Axes and Planes	16
2.8. SimSat II Body-Fixed Reference Frame and Principal Axes Alignment	18
2.9. Definition of Point O	21
2.10. SimSat II Body-Fixed Reference Frame	21
2.11. Orthonormal Coordinate Frame [25]	25
2.12. Euler Angles	27
2.13. Aerospace Euler Sequence [25]	28
2.14. SimSat II Momentum and Torque Vectors	33
2.15. PID Controller Block Diagram	35
3.1. SimSat II Groundstation	37
3.2. Space Electronics, Inc. Tri-Axis Spherical Air-Bearing	38
3.3. SimSat II Tabletop Deck Fastenings	39
3.4. SimSat II	40
3.5. Mini-box PC	41
3.6. dSPACE MicroAutoBox	42
3.7. Northrup Grumman LN-200 Fiber Optic Gyroscope IMU	42
3.8. Maxon Motor Reaction Wheel Assembly	43
3.9. Reaction Wheel Assembly Bracket	44
3.10. EPOS User Interface Wizards	45
3.11. EPOS User Interface Velocity Modes	46
3.12. EPOS Systems Inspection Checklist	48
3.13. SimSat II Root-Level SIMULINK Model	50
3.14. Example dSPACE ControlDesk Layout	51

	Page
3.15. SimSat II Communications Diagram	52
3.16. SimSat II Reaction Wheel Designs	56
3.17. EPOS 70/10 Velocity Controller	57
3.18. Electric Motor Open-Loop Transfer Function	59
3.19. SIMULINK Software Interrupt Block	62
3.20. dSPACE RTI CAN Block	63
3.21. EPOS 70/10 Angular Velocity Measurements	65
3.22. Disturbance Torque of 0.090 N · m Applied about X-Axis	66
3.23. RTI CAN Two-to-One Multiplexer	67
3.24. CAN Bus Time-Division Multiplexing	68
3.25. RTI CAN Time-Division Multiplexing	70
3.26. Non-Coinciding COM and COR	72
3.27. Horizontal COM Location of Reaction Wheel Assembly	73
3.28. Principal Axes of SimSat II	73
3.29. Measuring MOI of Spacecraft [4]	74
3.30. Hanging Mass MOI Measurement for Spacecraft Body	76
3.31. Error in Disturbance Torque Due to Cosine Losses	76
3.32. SimSat II MOI Measurement— I_{xx}	77
3.34. SimSat II on Test Stand	78
3.33. LN 200 Bias Measurements	79
4.1. Experimental Data Collections	83
4.2. Attitude Hold	84
4.3. Settling Time for Rest-to-Rest Maneuvers about 1-Axis	86
4.4. Residual Angular Velocity ψ_{w_1} for Rest-to-Rest Maneuver about 1-Axis	87
4.5. Settling Time for Rest-to-Rest Maneuvers about 2-Axis	88
4.6. Measured Angular Velocity ψ_{w_2} for Rest-to-Rest Maneuver about 2-Axis	88
4.7. Commanded Torque M_{w_2} for Rest-to-Rest Maneuver about 2-Axis	89
4.8. Settling Time for Rest-to-Rest Maneuvers about 3-Axis	90
4.9. Positive 30° Rest-to-Rest Maneuver about 3-Axis	90
4.10. Rest-to-Rest Maneuvers Performance Summary	91
4.11. Angular Velocity of SimSat II for Rest-to-Rest Maneuvers	92
4.12. EPOS 70/10 Command Intervals	93
4.13. Disturbance Torque Evaluation	94
4.14. Positive Torque about 1-Axis Using 75 g Mass	95

	Page
4.15. Positive Torque about 1-Axis Using 40 g Mass	95
4.16. Positive Torque about 1-Axis Using 20 g Mass	95
4.17. Positive Torque about 2-Axis Using 75 g Mass	97
4.18. Positive Torque about 2-Axis Using 40 g Mass	97
4.19. Positive Torque about 2-Axis Using 20 g Mass	97
4.20. Negative Torque about 3-Axis Using 145 g Mass	99
4.21. Negative Torque about 3-Axis Using 100 g Mass	99
4.22. Negative Torque about 3-Axis Using 50 g Mass	99
4.23. Effect of Δt on Measured Torque	101
B.1. Attitude Hold (1 of 2)	113
B.2. Attitude Hold (2 of 2)	114
B.3. Positive 10° Rest-to-Rest Maneuver about 1-Axis (1 of 2)	115
B.4. Positive 10° Rest-to-Rest Maneuver about 1-Axis (2 of 2)	116
B.5. Positive 20° Rest-to-Rest Maneuver about 1-Axis (1 of 2)	117
B.6. Positive 20° Rest-to-Rest Maneuver about 1-Axis (2 of 2)	118
B.7. Positive 10° Rest-to-Rest Maneuver about 2-Axis (1 of 2)	119
B.8. Positive 10° Rest-to-Rest Maneuver about 2-Axis (2 of 2)	120
B.9. Positive 20° Rest-to-Rest Maneuver about 2-Axis (1 of 2)	121
B.10. Positive 20° Rest-to-Rest Maneuver about 2-Axis (2 of 2)	122
B.11. Positive 10° Rest-to-Rest Maneuver about 3-Axis (1 of 2)	123
B.12. Positive 10° Rest-to-Rest Maneuver about 3-Axis (2 of 2)	124
B.13. Positive 20° Rest-to-Rest Maneuver about 3-Axis (1 of 2)	125
B.14. Positive 20° Rest-to-Rest Maneuver about 3-Axis (2 of 2)	126
B.15. Positive 30° Rest-to-Rest Maneuver about 3-Axis (1 of 2)	127
B.16. Positive 30° Rest-to-Rest Maneuver about 3-Axis (2 of 2)	128
B.17. Positive Torque about 1-Axis Using 20 g Mass (1 of 2)	129
B.18. Positive Torque about 1-Axis Using 20 g Mass (2 of 2)	130
B.19. Positive Torque about 1-Axis Using 40 g Mass (1 of 2)	131
B.20. Positive Torque about 1-Axis Using 40 g Mass (2 of 2)	132
B.21. Positive Torque about 1-Axis Using 75 g Mass (1 of 2)	133
B.22. Positive Torque about 1-Axis Using 75 g Mass (2 of 2)	134
B.23. Positive Torque about 2-Axis Using 20 g Mass (1 of 2)	135
B.24. Positive Torque about 2-Axis Using 20 g Mass (2 of 2)	136
B.25. Positive Torque about 2-Axis Using 40 g Mass (1 of 2)	137

	Page
B.26. Positive Torque about 2-Axis Using 40 g Mass (2 of 2)	138
B.27. Positive Torque about 2-Axis Using 75 g Mass (1 of 2)	139
B.28. Positive Torque about 2-Axis Using 75 g Mass (2 of 2)	140
B.29. Negative Torque about 3-Axis Using 50 g Mass (1 of 2)	141
B.30. Negative Torque about 3-Axis Using 50 g Mass (2 of 2)	142
B.31. Negative Torque about 3-Axis Using 100 g Mass (1 of 2)	143
B.32. Negative Torque about 3-Axis Using 100 g Mass (2 of 2)	144
B.33. Negative Torque about 3-Axis Using 145 g Mass (1 of 2)	145
B.34. Negative Torque about 3-Axis Using 145 g Mass (2 of 2)	146

List of Tables

Table		Page
2.1.	AFIT Satellite Simulator Research	13
3.1.	SimSAT II Ground Station PC Specifications	38
3.2.	Mini-Box PC Specifications	41
3.3.	Northrop Grumman LN-200 IMU	43
3.4.	SimSAT II Measured MOI Values	78
3.5.	SimSAT II's Reaction Wheel Measured MOI Values	78
3.6.	LN-200 Bias Measurements	79
3.7.	LN-200 Bias Correction	80
3.8.	SimSat II PID Gain Settings	80
4.1.	Positioning Accuracy of the Reaction Wheel ACS	85
4.2.	Rest-to-Rest Maneuvers Performance Summary	91
4.3.	Disturbance Torques Performance Summary	100

List of Abbreviations

Abbreviation		Page
ACS	Attitude Control System	1
PI	Proportional-plus-Integral	2
PD	Proportional-plus-Derivative	2
PID	Proportional-Integral-Derivative	2
AFIT	Air Force Institute of Technology	2
SimSat	Satellite Simulator	2
MOI	Moment of Inertia	4
POI	Product of Inertia	4
COM	Center of Mass	4
COR	Center of Rotation	4
DOF	Degree of Freedom	7
CMG	Control Moment Gyroscope	11
EOM	Equations of Motion	15
ODE	Ordinary Differential Equation	24
ECI	Earth-Centered Inertial	24
NASA	National Aeronautics and Space Administration	31
IMU	Inertial Measurement Unit	36
RDC	Remote Desktop Connection	37
FOG	Fiber Optic Gyro	42
SDLC	Synchronous Data Link Control	43
CAN	Control Area Network	45
RTI	Real-Time Interface	63
TDM	Time-Division Multiplexing	67
TX	Transmit	68
RX	Receive	68

ATTITUDE CONTROL OF A SATELLITE SIMULATOR USING REACTION WHEELS AND A PID CONTROLLER

I. Introduction

1.1 *Background*

The orientation requirements of a satellite (also referred to as spacecraft throughout this research) are determined by its mission: telecommunications, optical imagery, scientific research, and meteorology to name a few. The mission also dictates the orientation of various satellite hardware components. Solar arrays are oriented toward the sun, thermal radiators are pointed at deep space, and antennas are pointed at their intended targets. A satellite's ability to orient its mission critical hardware components, as well as its payload, are all incumbent upon the performance of the spacecraft's attitude control system (ACS).

Active attitude determination, in short, is the satellite's attitude measurement compared to a mission driven desired value. The difference between the attitude measurement and the desired value is the satellite's attitude error. The purpose of the ACS is to generate a corrective torque that will null this error. Because external disturbances will occur, and because both measurements and corrections will be imperfect, the corrective cycle will continue indefinitely.

Reaction wheels are a common choice for active spacecraft attitude control. For accuracy and moderately fast maneuverability, reaction wheels are the preferred ACS because they allow continuous and smooth control while inducing the lowest possible disturbance torques [48]. In this mode of control, an electric motor mounted to the spacecraft spins a freely rotating wheel; as the reaction wheel changes its rate of rotation in one direction it causes the spacecraft to rotate in the opposite direction. The electric motor rotates the wheel in response to a correction command computed as part of the spacecraft's feedback control loop.

The control torque inputs are generally a function of attitude errors. A spacecraft can be modeled as a rigid body and its dynamics as second-order systems where damping control must be provided for improved stability. Proportional-plus-integral (PI) control eliminates error and can provide good steady-state behavior for both corrective and disturbance inputs. The dynamic response, however, is much slower than that of proportional-plus-derivative (PD) control. To achieve favorable steady-state and dynamic responses one can combine PI and PD control into one controller via proportional-integral-derivative (PID) control [7].

1.2 Problem Statement

The Air Force Institute of Technology's (AFIT) second-generation satellite simulator (SimSat), SimSat II, provides a means to simulate spacecraft attitude control. In 2009, McFarland used a fan thruster ACS on-board SimSat II to investigate near real-time closed-loop optimal control. The fan thruster ACS could not provide smooth torques without generating disturbance torques of its own from excessive vibrations. McFarland also encountered characterization difficulties with the fan thruster ACS because torque was dependent on the spacecraft's angular velocity. McFarland attempted three different approaches to characterize the thrust generated from the fan thruster ACS, yet none were void of inaccuracies [33].

AFIT faculty have requested that an improved reaction wheel ACS be implemented on-board SimSat II. The ACS must be capable of attaining the following performance specifications:

1. Reaction wheels shall generate sufficient torque to perform the fastest slew maneuvers.
 - (a) Positioning accuracy shall be $\pm 0.01^\circ$.
 - (b) A $\pm 10^\circ$ rest-to-rest maneuver about the 1- and 2-axis shall be demonstrated within 10 seconds.
 - (c) A $\pm 30^\circ$ rest-to-rest maneuver about the 3-axis shall be demonstrated within 10 seconds.

- (d) SimSat II's angular velocity shall not exceed $180^\circ/\text{s}$.
- 2. Reaction wheel torque shall equal the worst case anticipated disturbance torque.
- 3. Reaction wheels must have sufficient momentum storage.

1.3 Research Objectives

The objective of this research is to design, build, test, and evaluate the performance of a reaction wheel ACS on-board SimSat II, pictured in Figure 1.1. The end result of this research objective will produce a satellite simulator capable of maintaining position accuracy within $\pm 0.01^\circ$ and performing $\pm 10^\circ$ rest-to-rest maneuvers within 10 s about the 1- and 2-axis and $\pm 30^\circ$ within 10 s about the 3-axis; all while overcoming the worst case anticipated disturbance inputs.

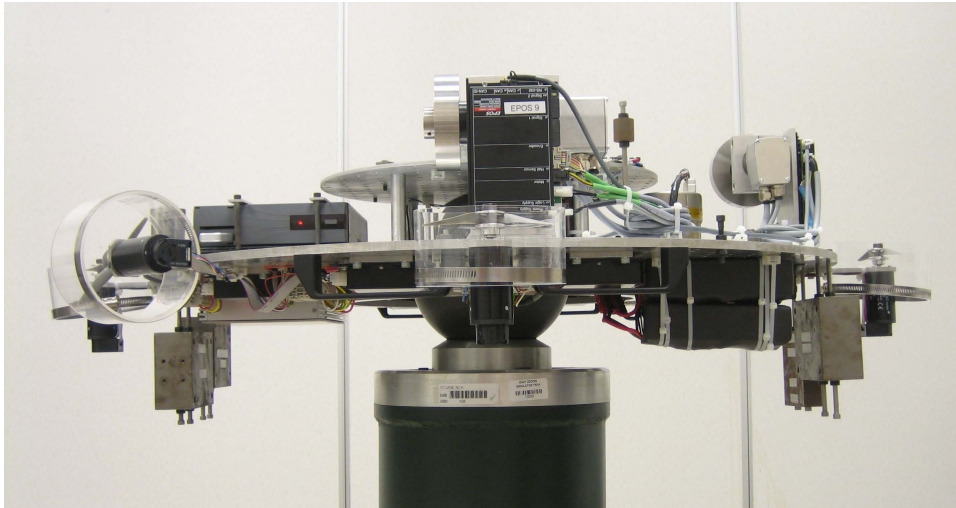


Figure 1.1: SimSat II with Reaction Wheel ACS

1.4 Methodology

The methodology of this research followed in concordance with the research objectives in Section 1.3. First, a preliminary design of one reaction wheel assembly was created. Then, improving upon the lessons learned from the preliminary design, an ACS consisting of three reaction wheel assemblies was built along with the necessary SIMULINK control logic. Following the build phase of this research, the software logic underwent

extensive testing. Lastly, with SimSat II in its best possible set-up, the reaction wheel ACS was evaluated in a series of experiments.

1.5 Assumptions

Several assumptions were made throughout the course of this research. The first assumption is that SimSat II is a rigid body that uses a body-fixed reference frame aligned with its principal axes (see Figure 1.2(a)); therefore, its moment of inertia (MOI) matrix is void of product of inertia (POI) terms. The POI of SimSat II's reaction wheels are also assumed to equal zero. The SimSat II MOI values used in the design phase of this research were assumed to be those previously measured by McFarland [33]. Lastly, it is assumed that SimSat II's center of mass (COM) is coincident with its center of rotation (COR) (see Figure 1.2(b)) since prior to each series of experiments, SimSat II's COM was repositioned.

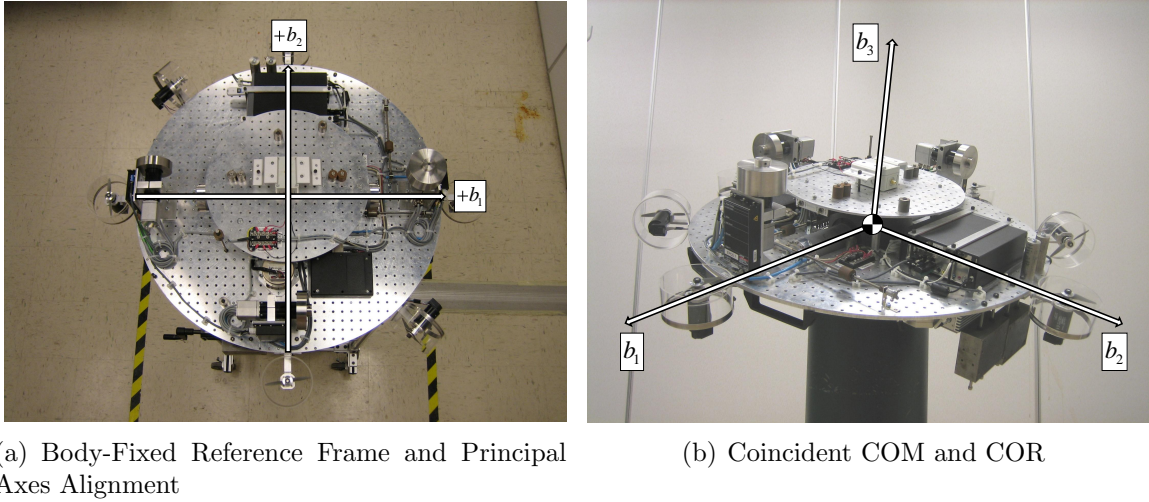


Figure 1.2: SimSat II Assumptions

1.6 Preview

Chapter II presents a review of relevant literature pertaining to the topics concerning this thesis. Here, an overview of satellite simulator styles is given as well as several satellite simulator research efforts conducted across academia; specifically, the type of ACS used for each satellite simulator research effort is highlighted. Also, previous satellite simulator research efforts conducted by AFIT are presented. Literature on spacecraft

dynamics and PID attitude control is also presented in Chapter II. The methodology used to design, build, and test the reaction wheel ACS is then presented in Chapter III. Chapter IV follows by evaluating the performance of the reaction wheel ACS based upon analysis of the resultant experimental data. Finally, Chapter V discusses conclusions and recommendations garnered from this research effort.

II. Background

2.1 *Satellite Simulators*

An unprecedented degree of pointing accuracy is required for space missions such as formation flying, cross-link communications, and proximity and rendezvous operations. Over the years, many forms of satellite control logic have been developed to address the challenges of satellite attitude control i.e., stabilizing the satellite, reorienting the satellite, rejecting disturbance inputs to the satellite, etc. A low-torque environment is often central to the success of high-precision systems. Space systems are often times both high-visibility and high-risk. Programs that can benefit from hardware demonstration and experimental validation of attitude control logic on satellites typically forego these stages because the influence of gravity and friction on Earth render one-g experimentation unrealistic. Be that as it may, simulating a torque-free environment for purposes of satellite testing is not trivial [23, 44].

One method that does not lend itself well to satellite testing is neutral buoyancy. Astronauts will often times prepare for space walks by donning a wet suit and submerging themselves into a tank of water. Needless to say, the idea of submerging a satellite into a tank of water presents itself with major challenges. Doing so would require encapsulation of the satellite, and as a result exhaust gases would be trapped. Even if exit orifices for the thruster exhaust gases were constructed, the viscosity of the water would alter the thruster effects and subsequent rotational drag of the satellite.

A second method that does not lend itself well to satellite testing is the use of drop towers; dropping a satellite from some vertical distance and catching it in a soft net while high-speed cameras capture the free-fall event. Afterwards, the attitude control test event can be analyzed using the captured images. Limitations associated with this method include the effects of air drag and the danger of damaging the fragile satellite as it is caught in a net [3].

A method of simulating the torque free environment that does lend itself well to satellite testing is the use of an air-bearing. Air-bearings cannot provide an environment void of gravity, but an air-bearing offers a nearly torque-free environment, and for this reason, it is the preferred technology for ground-based research in spacecraft attitude

dynamics and control. Air-bearings pass pressurized air through small holes located in the stator which then generate a thin cushion of air that supports the weight of the rotor. An air-bearing capable of supporting several thousand pounds may require air pressurized to about 100 psi with a flow rate of only a few cubic feet per minute [45]. Depending on the type of air-bearing, some combination of nearly force-free translational motion and nearly torque-free rotational motion can be achieved.

2.1.1 Planar Air-Bearing . Space applications of interest for planar air-bearings include proximity and rendezvous operations. Planar air-bearing systems allow for one rotational and two translational degrees of freedom (DOF). The remaining two rotational DOFs and one out-of-plane translational DOF are arguably less important in the investigation of relative orbital dynamics [45]. In almost all planar air-bearing cases, the test body carries its own air supply. With this on-board air supply the test body is capable of producing its own cushion of air allowing it to hover upon or traverse a polished flat surface.

There are many planar air-bearing testbeds in use by universities to explore topics in proximity and rendezvous operations. Stanford University’s Aerospace Robotics Laboratory (ARL) has used a planar air-bearing to investigate the challenges inherent in the use of robotics for on-orbit construction. As seen in Figure 2.1, this testbed consists of a large two-link manipulator carrying two smaller two-link arms. The combination of

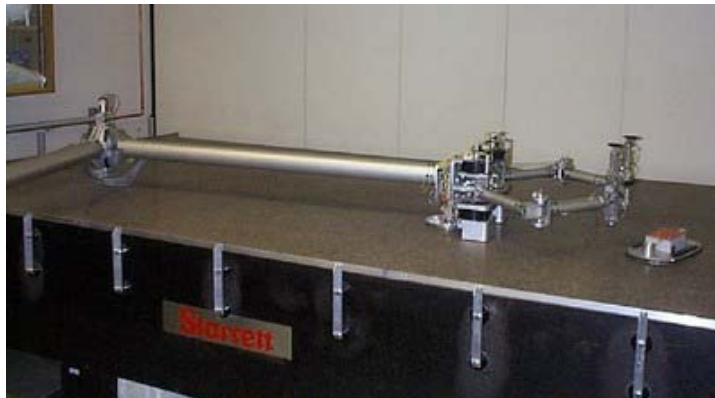


Figure 2.1: Two-Link Manipulator Testbed at Stanford University’s ARL [43]

linkages was developed to be representative of manipulators already used in space such as the Space Station Remote Manipulator System (SSRMS) [43].

The Tokyo Institute of Technology examined capturing methods for a damaged satellite using dual-manipulators. Solving this problem is significantly more difficult than that of construction because the target may be incapable of commanding its attitude control system. The chaser is therefore required to approach and grip the target while also eliminating the relative motion between both objects [26].

Lastly, the University of Victoria in British Columbia, Canada used a planar air-bearing to study the reduction of vibration excitation in point-to-point maneuvers of flexible manipulators therefore, determining an optimal trajectory for the maneuver [38].

2.1.2 Spherical Air-Bearings . Space applications of interest for spherical air-bearings center around spacecraft dynamics and control. The ideal spherical air-bearing testbed would allow its payload 360° motion about the yaw, pitch, and roll axes. As seen in Figure 2.2, unconstrained motion about all three axes is not possible due to interference from the pedestal upon which the spherical air-bearing rests. Constrained motion due to the pedestal is limited to angles less than $\pm 90^\circ$. Spherical air-bearing testbeds come in many shapes and sizes, and they are classified into three primary styles: dumbbell, tabletop, and umbrella which are represented in Figure 2.3.

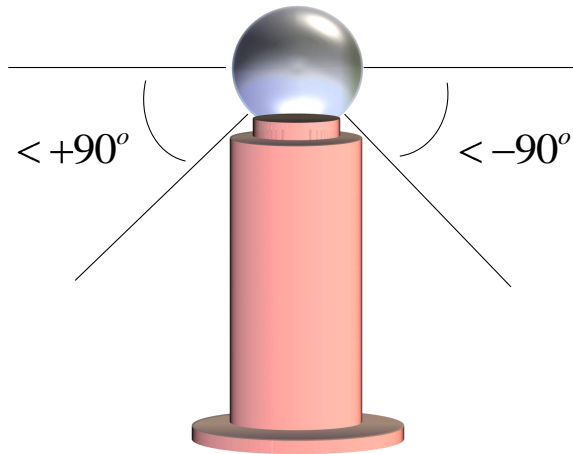
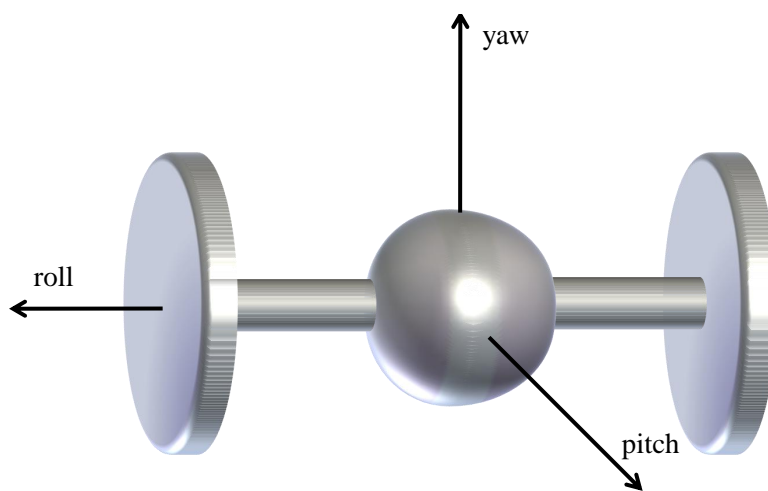


Figure 2.2: Spherical Air-Bearing Motion Constraints Due to Pedestal

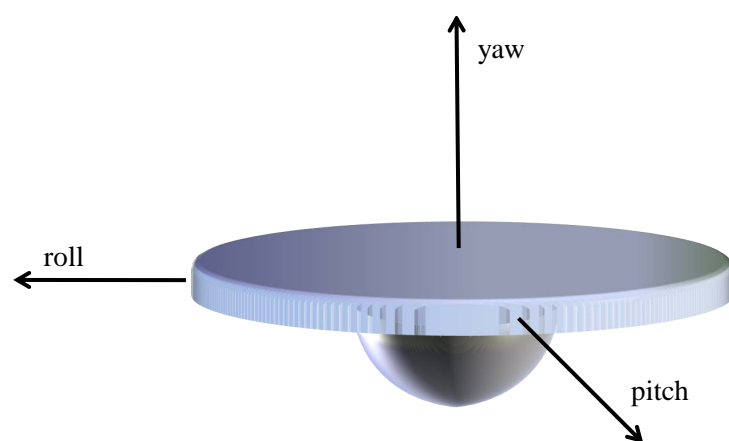
2.1.2.1 Dumbbell . Dumbbell-style spherical air-bearings offset the mounting surfaces away from the COR by means of two opposing extension rods. This style of testbed also allows for 360° motion about the roll and yaw axes (see Figure 2.3(a)). Bernstein *et al.* of the Department of Aerospace Engineering at the University of Michigan used their Triaxial Air Bearing Testbed equipped with reaction wheel and thruster ACS to investigate the identification of satellite mass properties [2]. Virginia Polytechnic Institute and State University (Virginia Tech) developed its Distributed Spacecraft Attitude Control System Simulator (DSACSS) to experimentally demonstrate formation flying of two satellites: one dumbbell-style and one tabletop-style spherical air-bearing. The dumbbell is outfitted with a reaction wheel plus thruster ACS whereas the tabletop is solely controlled by reaction wheels [44]. AFIT has also conducted research using a dumbbell-style spherical air-bearing which is discussed in greater detail in Section 2.2.

2.1.2.2 Tabletop . Tabletop-style spherical air-bearings possess a mounting surface that mounts directly onto the flat face of a hemispherical air-bearing (see Figure 2.3(b)). This style of air-bearing allows for 360° motion about the yaw-axis and limited motion about the pitch and roll axes. They are favorable for validating various spacecraft control strategies on Earth prior to launch, can be fabricated rather inexpensively, and typically require very little floor space [22]. Tabletop testbeds are ideal in university settings for faculty to demonstrate the concepts of spacecraft dynamics and attitude control. The Georgia Institute of Technology (Georgia Tech) constructed a hemispherical tabletop-style air-bearing testbed with a reaction wheel ACS for the experimental validation of theoretically developed attitude control algorithms [23]. As mentioned in Section 2.1.2.1, Virginia Tech uses a tabletop-style air-bearing in its DSACSS testbed to experimentally demonstrate formation flying of two satellites [44]. AFIT possesses a hybrid tabletop/umbrella air-bearing for research purposes. As with their dumbbell-style air-bearing in Section 2.1.2.1, AFIT's use of their tabletop air-bearing is discussed in greater detail in Section 2.2.

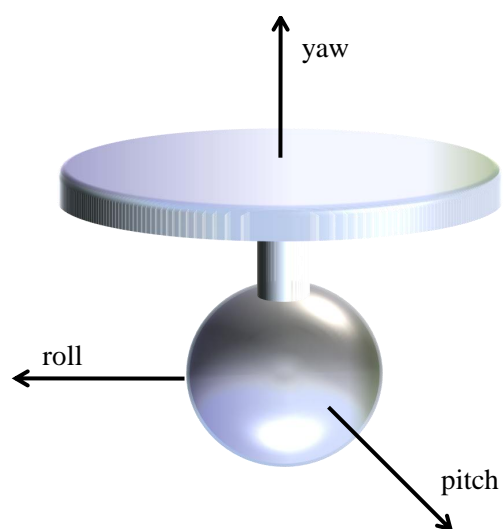
2.1.2.3 Umbrella . Similar to that of the tabletop-style air-bearing, umbrella-style testbeds allow for 360° motion about the yaw-axis and limited motion



(a) Dumbbell



(b) Tabletop



(c) Umbrella

Figure 2.3: Spherical Air-Bearing Styles

about the pitch and roll axes. Umbrella-style spherical air-bearings are assembled by extruding a rod from a fully spherical bearing. A flat plate similar to the tabletop air-bearing can be mounted at the end of this rod (see Figure 2.3(c)). Moreover, a much larger structure extending outward and down (like an umbrella) can be mounted to the end of this rod. The Honeywell, Inc. Momentum Control System and Line of Sight (MCS/LOS) umbrella-style spherical air-bearing offers structural control by means of active vibration isolation and payload-steering platforms and discrete high-performance structural dampers. Equipped with six control moment gyroscopes (CMG), MCS/LOS also offers high-agility slew and scan capability [37]. The United States Air Force Research Laboratory (AFRL) has used its propellant actuated Advanced Space Structure Technology Research Experiments (ASTREX) facility as a test bed for validation and integration of controls/structure interaction technologies [10]. Lastly, the Naval Postgraduate School (NPS) has used its umbrella-style spherical air-bearing equipped with an ACS consisting of reaction wheels, cold-gas thrusters, and rate gyros to validate attitude stabilization control together with laser jitter rejection [41].

2.2 *AFIT Satellite Simulators*

In 1998-99, the systems engineering team of Colebank, Jones, Nagy, Pollak, and Mannebach broke ground on the design and construction of AFIT's first-generation satellite simulator, SimSat I. This dumbbell-style testbed equipped with reaction wheel ACS (see Figure 2.4) was assembled with the intent to support experimentation in the areas of attitude control, precision pointing, and vibration suppression [8]. The efforts of Colebank *et al.* were continued into 2000 whereupon SimSat I became fully operational. In addition to being fully operational, a multimedia lesson plan on satellite dynamics was developed to reinforce AFIT classroom instruction [18]. SimSat I was later used to investigate hybrid control strategies for rapid satellite pointing [17]. From a national security perspective, SimSat I aided in a study that explored the feasibility for parasitic microsatellites to autonomously loiter about a target satellite to rendezvous, dock, and then disrupt, degrade, disable, or destroy the system [9, 24]. SimSat I was used to determine whether the attitude of a satellite can be determined from telemetry data

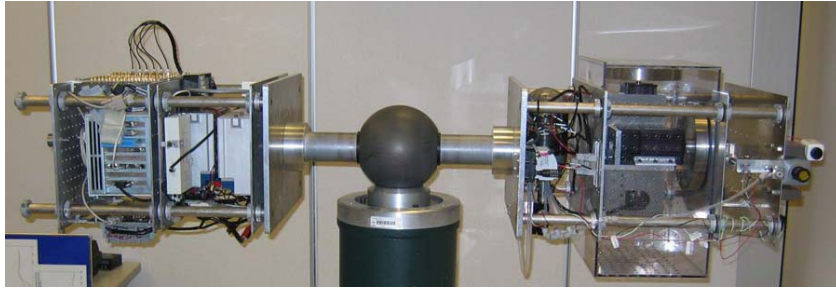


Figure 2.4: SimSat I [19]

and an accurate satellite model [49]. Lastly, SimSat I aided students in the exploration of measuring MOI using the change in the satellite's fuel mass [19, 21]. In all, AFIT's first-generation satellite simulator, SimSat I, was in use from 1999 until 2007.

Over the duration of its use, SimSat I revealed several limitations. Due to its large mass and inertia, SimSat I was not able to conduct rapid slew maneuvers nor was it able to attain the necessary angular velocity about the body to achieve spin stabilization. Its momentum wheel ACS quickly saturated while performing reorientation maneuvers. Furthermore, the dumbbell experienced structural flexing which caused the satellite's COM to move. The aging hardware, especially the electronics, on SimSat I became out-of-date and needed to be replaced. As a result of these limitations, AFIT faculty requested that an improved satellite simulator be designed [40].

SimSat I was subsequently dismantled and cannibalized for parts by the systems engineering team of Roach, Rohe, and Welty in the development of AFIT's second-generation satellite simulator, SimSat II [40]. Instead of building another dumbbell-style spherical air-bearing, Roach *et al.* constructed a hybrid tabletop- and umbrella-

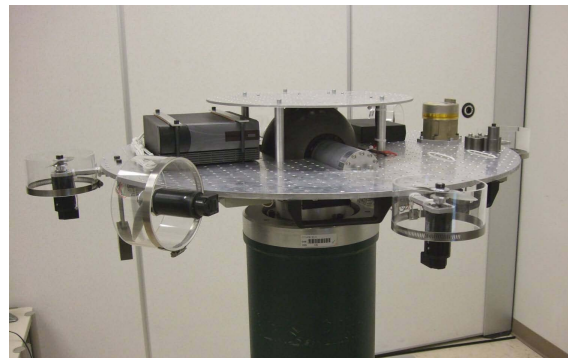


Figure 2.5: SimSat II with Fan Thruster ACS [40]

style system equipped with an external fan thruster ACS (see Figure 2.5). Although a hybrid, SimSat II functions more like a tabletop-style. SimSat II was constructed with the intent that it meet the research needs of AFIT faculty in the area of spacecraft dynamics and control. In 2009, McFarland

gave SimSat II its first test-drive with his inquiry into optimal control for spacecraft reorientation maneuvers [33]. In total, AFIT's spacecraft simulators have afforded many opportunities for graduate students to explore challenging topics. Table 2.1 summarizes past AFIT research.

Table 2.1: AFIT Satellite Simulator Research

Student(s)	Year	Style	Advisor	Research Topic
Colebank <i>et al.</i>	1999	Dumbbell	Lt Col Kramer	Satellite Simulator Design and Assembly
Fulton	2000	Dumbbell	Capt Agnes	Attitude Control and Multimedia Representation
Dabrowski	2003	Dumbbell	Maj Cobb	Detection of Parasitic Satellite
French	2003	Dumbbell	Maj Cobb	Control Strategies for Rapid, Large-Angle Maneuvers
Kimsal	2004	Dumbbell	Maj Cobb	Autonomous Infrared Tracking
Smith	2005	Dumbbell	Dr. Cobb	Attitude Control using Reaction Wheels and Thrusters
Geitgey	2006	Dumbbell	Dr. Cobb	Measuring Remaining Propellant using Measured MOI
Hines	2007	Dumbbell	Lt Col Titus	Fuel Estimation Using Dynamic Response
Roach <i>et al.</i>	2008	Tabletop	Dr. Black	Satellite Simulator Design and Assembly
McFarland	2009	Tabletop	Lt Col Swenson	Optimal Control of Spacecraft Reorientation Maneuvers

2.3 *Spacecraft Dynamics*

2.3.1 Rigid Body Dynamics . A system of particles in which the distance between any two particles is constant is defined as a rigid body. The motion of a rigid body in space is typically separated into the translational motion of its COM and the rotational motion of the body about its COR. Therefore, a rigid body is a dynamic system consisting of six DOF: three translational and three rotational [51].

The foundation for rigid body dynamics is the concept of particle dynamics as described by Sir Isaac Newton. Sellers summarizes Newton's three laws of particle motion as [46]:

1. A body continues in its state of rest, or of uniform motion in a straight line, unless compelled to change that state by forces impressed upon it.
2. The time rate of change of an object's momentum equals the applied force.
3. When body A exerts a force on body B, body B will exert an equal, but opposite, force on body A.

These three laws of mechanics coupled with Newton's law for gravitational attraction form the basis of translation and rotational motion.

2.3.1.1 Translational Motion .

A particle can be described as a body whose entire mass acts at a single point—also referred to as a point mass. When an external force acts upon the particle, it can exhibit up to three translational DOFs: one in the x-direction, one in the y-direction, and one in the z-direction. The behavior of that particle will follow Newton's 1st law. Likewise, the external force will cause the particle to experience Newton's 2nd law. In modern vector notation, Newton's 2nd law takes the form

$$\vec{F} = m\vec{a} \quad (2.1)$$

where \vec{F} is the total force on a particle with mass m , and \vec{a} is the particle's acceleration with respect to the inertial reference frame.

When an external force acts on a rigid body the external force is said to act upon one of the many constituent particles that comprise the rigid body. With the exception of the pure spin case, when one particle accelerates then all other particles must also accelerate.

Newton's 2nd law, previously written in vector notation for a particle, can be expressed as a summation for each particle of a rigid body

$$\vec{F}_i = \vec{f}_{ie} + \sum_{i \neq j}^N \vec{f}_{ij} = m_i \vec{a}_i \quad (2.2)$$

where \vec{F}_i is the total force and \vec{f}_{ie} is the external force acting on particle i . The vector sum of \vec{f}_{ij} is the internal rigid body force from particle i acting on the j^{th} constituent particle, and $m_i \vec{a}_i$ is the mass and resultant acceleration of particle i . When the number of constituent particles in a rigid body equals four or more, a rigid body possesses six DOFs [52]. If Equation (2.2) is summed over N particles the following results

$$\sum_{i=1}^N \vec{F}_i = \sum_{i=1}^N \vec{f}_{ie} + \sum_{i=1}^N \sum_{i \neq j}^N \vec{f}_{ij} = \sum_{i=1}^N m_i \vec{a}_i . \quad (2.3)$$

Newton's 3rd law states that when body i exerts a force \vec{f}_{ij} on body j , body j will exert an equal, but opposite, force $-\vec{f}_{ij}$ on body i . Therefore, Equation (2.3) reduces to

$$\vec{F}_e = \sum_{i=1}^N \vec{f}_{ie} = \sum_{i=1}^N m_i \vec{a}_i . \quad (2.4)$$

If a position vector \vec{r}_{com} is defined as extending from the origin of an inertial reference frame to the COM of the rigid body as shown in Figure 2.6 and M_T is defined as the total mass of the rigid body, \vec{r}_{com} can be computed from

$$\vec{r}_{com} = \frac{1}{M_T} \sum_{i=1}^N m_i \vec{r}_i . \quad (2.5)$$

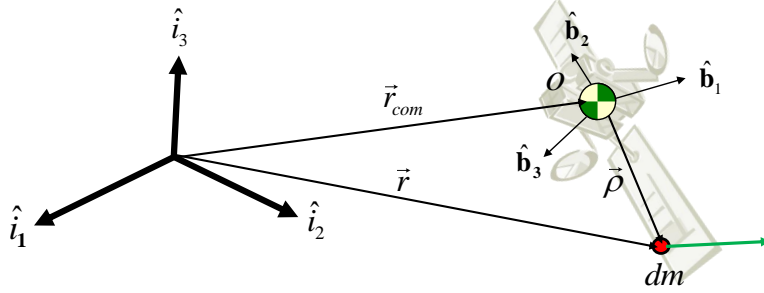


Figure 2.6: Definition of \vec{r}_{com}

The acceleration of the rigid body can be found by differentiating \vec{r}_{com} two times transforming Equation (2.5) into

$$M_T \frac{d^2}{dt^2} \vec{r}_{com} = \sum_{i=1}^N m_i \vec{a}_i . \quad (2.6)$$

Equations (2.4) and Equation (2.6) can then be equated such that

$$\vec{F}_e = M_T \frac{d^2}{dt^2} \vec{r}_{com} . \quad (2.7)$$

In other words, the sum of all external forces must equal the total mass of the rigid body times the acceleration of the COM. Equations (2.2), (2.5), and (2.7) are the three translational equations of motion (EOM).

2.3.1.2 *Rotational Motion* . The COM of a body provides no insight into how the mass is distributed about the body. The COM simply conveys its location relative to some reference frame. A body's resistance to rotation can be described provided the distribution of mass about the body is known. Using the x - y - z coordinate frame in Figure 2.7, there are two quantities which describe the mass distribution of a rigid body. The first is the distribution of mass with respect to an axis i.e., x -, y -, or z -axis. The second is the distribution of mass with respect to a plane i.e., xy , yz , or xz planes.

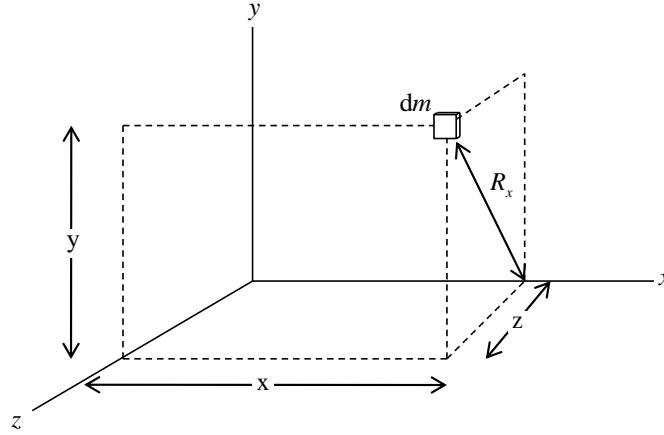


Figure 2.7: Distribution of Mass with Respect to Axes and Planes

A rigid body's MOI about an axis is relative to the amount of mass displaced from that axis. The MOI of a rigid body about an axis of rotation is described mathematically by Equation (2.8)

$$I_{xx} = \sum_{i=1}^N m_i (y_i^2 + z_i^2) \quad (2.8a)$$

$$I_{yy} = \sum_{i=1}^N m_i (x_i^2 + z_i^2) \quad (2.8b)$$

$$I_{zz} = \sum_{i=1}^N m_i (x_i^2 + y_i^2) . \quad (2.8c)$$

The implication of Equation (2.8) is two fold: either increasing the mass or increasing the mass' distance from the axis of rotation enlarges the body's MOI about that axis.

A rigid body's POI are a measure of how much of its mass is displaced relative to a particular plane. The POI are defined from the xy , xz , and yz planes respectively and expressed mathematically in Equation (2.9) as

$$I_{xy} = - \sum_{i=1}^N m_i x_i y_i = I_{yx} \quad (2.9a)$$

$$I_{xz} = - \sum_{i=1}^N m_i x_i z_i = I_{zx} \quad (2.9b)$$

$$I_{yz} = - \sum_{i=1}^N m_i y_i z_i = I_{zy} . \quad (2.9c)$$

The POI describes symmetrical properties of a rigid body with respect to a reference frame's plane. Symmetry about the xy plane yields I_{xz} and I_{yz} equal to zero; the xz plane, I_{xy} and I_{yz} equal zero; and for the yz plane, I_{xy} and I_{xz} equal zero. In matrix form, the POI and MOI of a rigid body about an axis of rotation appear as follows

$$\mathbf{I} = \begin{bmatrix} I_{xx} & I_{xy} & I_{xz} \\ I_{yx} & I_{yy} & I_{yz} \\ I_{zx} & I_{zy} & I_{zz} \end{bmatrix} . \quad (2.10)$$

If a rigid body is symmetric about an axis then it must have symmetry about at least two planes. Thus for a body that has an axis of symmetry, all products of inertia vanish when one of the coordinate axes is along the symmetry axis. It should be noted that a body need not have planes or axes of symmetry for the products of inertia to vanish. A proper orientation of the [coordinate axes] leads to the same result...If the coordinate axes are selected such that the products of inertia vanish, the coordinate axes are referred to as principal axes and the corresponding MOI are called principal MOI [1].

The inertia matrix of the principal MOI is

$$\mathbf{I} = \begin{bmatrix} I_{xx} & 0 & 0 \\ 0 & I_{yy} & 0 \\ 0 & 0 & I_{zz} \end{bmatrix} = \begin{bmatrix} A & 0 & 0 \\ 0 & B & 0 \\ 0 & 0 & C \end{bmatrix} . \quad (2.11)$$

By definition, the mass of a rigid body does not change over time. The MOI matrix only needs to be recalculated if there is a change in the rigid body's mass or its distribution. Roach *et al.* estimated the MOI matrix of SimSat II using SolidWorks® computer aided design (CAD) software; the estimated MOI values are

$$\mathbf{I} = \begin{bmatrix} I_{xx} & I_{xy} & I_{xz} \\ I_{yx} & I_{yy} & I_{yz} \\ I_{zx} & I_{zy} & I_{zz} \end{bmatrix} = \begin{bmatrix} 4.474 & 0.083 & -0.006 \\ 0.083 & 4.133 & 0.004 \\ -0.006 & 0.004 & 6.786 \end{bmatrix} \text{kg} \cdot \text{m}^2 .$$

To simplify analysis, SimSat II uses a body-fixed reference frame assumed to be aligned with the satellite's principal axes as seen in Figure 2.8.

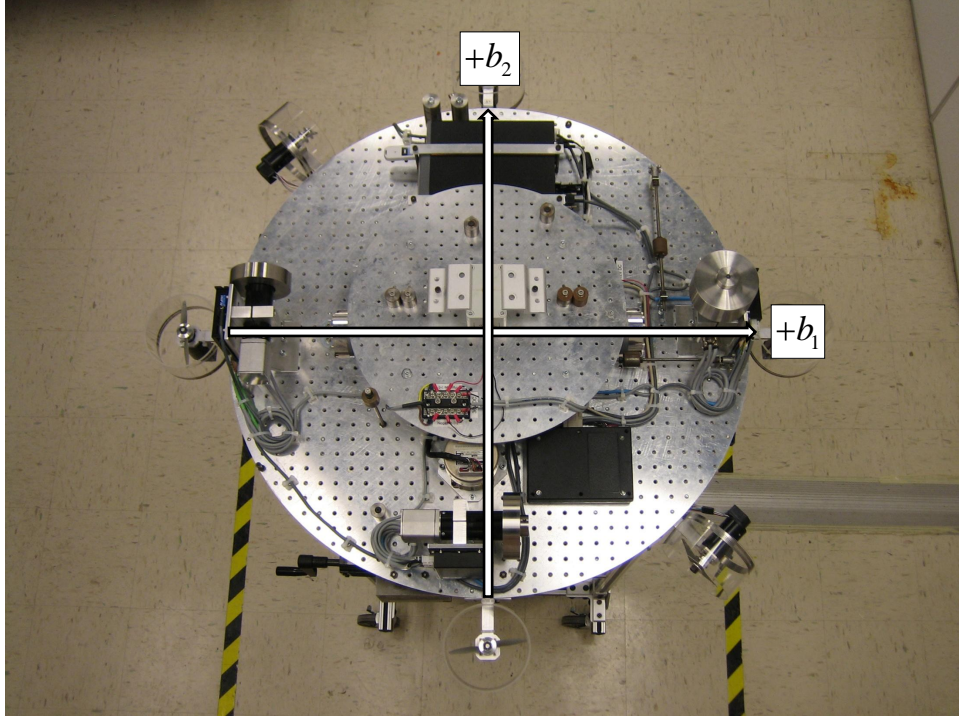


Figure 2.8: SimSat II Body-Fixed Reference Frame and Principal Axes Alignment

This research, as did McFarland's, assumes SimSat II's MOI matrix to be a matrix of principal moments. McFarland experimentally measured SimSat II's MOI matrix to be

$$\mathbf{I} = \begin{bmatrix} A & 0 & 0 \\ 0 & B & 0 \\ 0 & 0 & C \end{bmatrix} = \begin{bmatrix} 3.8 & 0 & 0 \\ 0 & 3.2 & 0 \\ 0 & 0 & 5.0 \end{bmatrix} \text{ kg} \cdot \text{m}^2 .$$

The attributes in which we can assume that a rigid body has an MOI matrix of principal moments and the experimental method used for determining SimSat II's principal MOI matrix is presented in Section 3.4.6 along with the results. Having discussed MOI and its effects on a rigid body's resistance to motion, discussions on rotational kinematics can now proceed followed by rotational kinetics.

For rotational motion about a fixed axis, the simplest accelerated motion to analyze is motion under constant angular acceleration α . The associated kinematic relationships must first be developed.

The instantaneous angular speed ω of a particle is defined as the change in the particle's angular position $\Delta\beta$ divided by the change in time Δt as Δt approaches zero

$$\omega \equiv \lim_{\Delta t \rightarrow 0} \frac{\Delta\beta}{\Delta t} = \frac{d\beta}{dt} . \quad (2.12)$$

The instantaneous angular acceleration α of a particle is defined as the limit of the change in the particle's angular velocity $\Delta\omega$ divided by the change in time Δt as Δt approaches zero

$$\alpha \equiv \lim_{\Delta t \rightarrow 0} \frac{\Delta\omega}{\Delta t} = \frac{d\omega}{dt} . \quad (2.13)$$

Rewriting Equation (2.13) in the form

$$d\omega = \alpha dt \quad (2.14)$$

and integrating both sides while maintaining α as a constant, it is found that

$$\omega = \omega_o + \alpha(t - t_o) . \quad (2.15)$$

Variables with the subscript o denote the initial condition of that variable. Often times, initial conditions are established for when time t equals zero. Choosing to substitute Equation (2.12) into Equation (2.15) and integrating once more the angular position of the particle β can be expressed as

$$\beta = \beta_o + \omega_o(t - t_o) + \frac{1}{2}\alpha(t - t_o)^2 . \quad (2.16)$$

Eliminating $(t - t_o)$ from Equations (2.15) and (2.16), an expression relating angular position β , velocity ω , and acceleration α is formulated such that

$$\omega^2 = \omega_o^2 + 2\alpha(\beta - \beta_o) . \quad (2.17)$$

The kinematic expressions of Equations (2.12)–(2.17) are for rotational motion assuming constant angular acceleration α . In addition to being valid for rotational particle motion, Equations (2.12)–(2.17) are also valid for rigid-body rotation about a fixed axis (rotational kinetics) [47].

The EOM for rotational kinetics are found in a similar manner as the translational EOM in Section 2.3.1.1. It is necessary to develop the associated kinetic relationships starting with the rotational equation analogous to Newton's 2nd Law that relates moments (also referred to as torque) M and angular acceleration α . If a point O is chosen, as in Figure 2.9, with respect to an inertial frame and located at the COM of the rigid body then the analogous rotational equation can be expressed as Equation (2.18) [52]

$$\vec{M} = \dot{\vec{H}} . \quad (2.18)$$

The vector quantity \vec{M} is an applied external moment and $\dot{\vec{H}}$ is the time rate of change for the angular momentum of the rigid body. If the applied external moment \vec{M} is equal

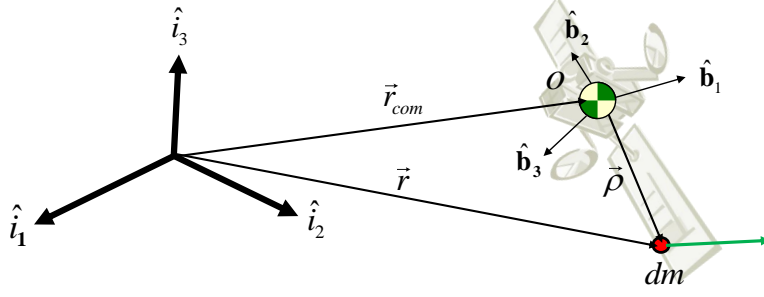


Figure 2.9: Definition of Point O

to zero, then the angular momentum vector \vec{H} becomes a constant. That is, the angular momentum of the rigid body is conserved. This relation is known as the *principle of conservation of angular momentum*. For this reason, the COM is often selected as a reference point O of the rigid body [51].

For this research, torque and angular momentum are computed with respect to SimSat II's COM. The origin of SimSat II's body-fixed reference frame is fixed to its COM (see Figure 2.10).

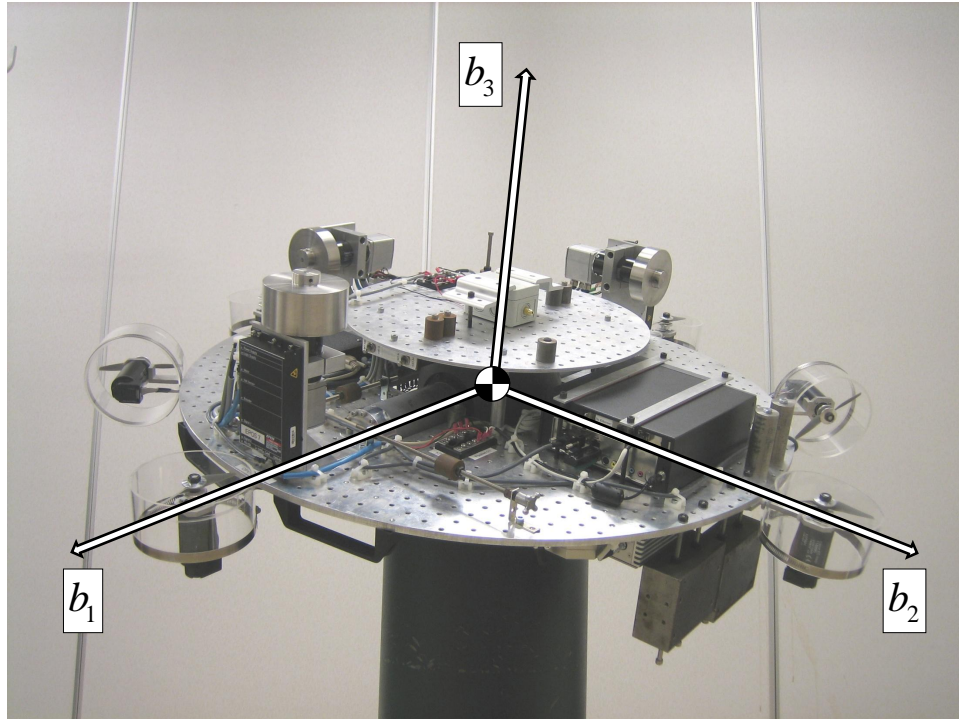


Figure 2.10: SimSat II Body-Fixed Reference Frame

The angular momentum relative to the COM can be written as

$$\vec{H} = \mathbf{I}\vec{\omega} \quad (2.19)$$

where \mathbf{I} is the MOI matrix and ω is the angular velocity of the spacecraft. Substituting Equation (2.19) into Equation (2.18), with respect to the inertial frame $\{\hat{i}\}$, the applied moment can be expressed as

$$\vec{M} = \mathbf{I}\dot{\vec{\omega}} \quad (2.20a)$$

$$= \mathbf{I}\vec{\alpha} . \quad (2.20b)$$

Using the transport theorem, the inertial derivative of Equation (2.19) given in the body frame $\{\hat{b}\}$ is

$$\dot{\vec{H}} = \mathbf{I}\dot{\vec{\omega}} + \vec{\omega} \times \mathbf{I}\vec{\omega} . \quad (2.21)$$

Equation (2.18) can then be expressed in the body frame as

$$\vec{M} = \mathbf{I}\dot{\vec{\omega}} + \vec{\omega} \times \mathbf{I}\vec{\omega} . \quad (2.22)$$

It is assumed that \mathbf{I} is of the principal axis form described in Equation (2.11). By also defining

$$[\vec{\omega}] = \begin{bmatrix} \omega_1 \\ \omega_2 \\ \omega_3 \end{bmatrix} , \quad (2.23)$$

and noting that \mathbf{I} is constant with respect to the body-fixed frame, Equation (2.22) can be written as

$$\begin{bmatrix} M_1 \\ M_2 \\ M_3 \end{bmatrix} = \begin{bmatrix} A\dot{\omega}_1 \\ B\dot{\omega}_2 \\ C\dot{\omega}_3 \end{bmatrix} + \begin{bmatrix} \omega_1 \\ \omega_2 \\ \omega_3 \end{bmatrix} \times \begin{bmatrix} A\omega_1 \\ B\omega_2 \\ C\omega_3 \end{bmatrix} . \quad (2.24)$$

After carrying out the cross product and algebraically manipulating Equation (2.24), three scalar equations remain,

$$M_1 = A\dot{\omega}_1 - (B - C)\omega_2\omega_3 \quad (2.25a)$$

$$M_2 = B\dot{\omega}_2 - (C - A)\omega_1\omega_3 \quad (2.25b)$$

$$M_3 = C\dot{\omega}_3 - (A - B)\omega_1\omega_2 . \quad (2.25c)$$

Equation (2.25) is referred to as Euler's EOM for a rigid body. Had the COM not been chosen as the reference point, Euler's equations would not have simplified so nicely. As a matter of fact, with POI terms present, Euler's equations are of the form

$$M_1 = I_{xx}\dot{\omega}_1 - I_{xy}(\dot{\omega}_2 - \omega_1\omega_3) - I_{xz}(\dot{\omega}_3 + \omega_1\omega_2) \quad (2.26a)$$

$$- (I_{yy} - I_{zz})\omega_2\omega_3 - I_{yz}(\omega_2^2 - \omega_3^2)$$

$$M_2 = I_{zz}\dot{\omega}_3 - I_{yz}(\dot{\omega}_3 - \omega_1\omega_2) - I_{xy}(\dot{\omega}_1 + \omega_2\omega_3) \quad (2.26b)$$

$$- (I_{zz} - I_{xx})\omega_1\omega_3 - I_{xz}(\omega_3^2 - \omega_1^2)$$

$$M_3 = I_{zz}\dot{\omega}_3 - I_{xz}(\dot{\omega}_1 - \omega_2\omega_3) - I_{yz}(\dot{\omega}_2 + \omega_1\omega_3) \quad (2.26c)$$

$$- (I_{xx} - I_{yy})\omega_1\omega_2 - I_{xy}(\omega_1^2 - \omega_2^2) .$$

Euler's equations describe the components of the angular velocity vector as seen from the body frame. Rearranging Equation (2.25), the body's angular velocity is presented as a function of time and applied torques; however, Equation (2.27) only represents one-half of the solution

$$\dot{\omega}_1 = \frac{M_1}{A} + \left(\frac{B - C}{A} \right) \omega_2 \omega_3 \quad (2.27a)$$

$$\dot{\omega}_2 = \frac{M_2}{B} + \left(\frac{C - A}{B} \right) \omega_1 \omega_3 \quad (2.27b)$$

$$\dot{\omega}_3 = \frac{M_3}{C} + \left(\frac{A - B}{C} \right) \omega_1 \omega_2 . \quad (2.27c)$$

The second half of the solution is the body's orientation with respect to inertial space. To obtain the second half of the solution set, angular velocity in the body frame must be related to changes in the orientation of the body.

2.3.2 Rotation Sequences in \mathbb{R}^3 . In Section 2.3.1, three scalar equations were found—Euler's equations—which are coupled, nonlinear, first-order ordinary differential equations (ODE). Euler's equations define the rotational dynamics of a rigid body in reference to a body-fixed reference frame. SimSat II's attitude is always expressed in the Earth-centered inertial (ECI) non-rotating reference frame. Therefore, a mathematical relationship must be derived to express the body-fixed angular position, velocity, and acceleration with respect to the ECI reference frame. This relationship is defined using rotation operators. Two widely used methods for identifying rotational motion are rotation matrices and Euler-angles.

2.3.2.1 Rotation Matrices . Given a vector \vec{b} in an orthonormal coordinate frame $\{\hat{i}\}$ as illustrated in Figure 2.11, the direction cosines for \vec{b} are the cosines of the angles ϕ , θ , and ψ between the vector \vec{b} and the coordinate axes defined by the basis vectors $\{\hat{i}_1 \ \hat{i}_2 \ \hat{i}_3\}$, respectively.

If the vector \vec{b} is expressed as a unit vector \hat{b} , the dot product allows the direction cosines to be expressed as

$$\cos \phi = \hat{i}_1 \cdot \hat{b} \quad (2.28a)$$

$$\cos \theta = \hat{i}_2 \cdot \hat{b} \quad (2.28b)$$

$$\cos \psi = \hat{i}_3 \cdot \hat{b} . \quad (2.28c)$$

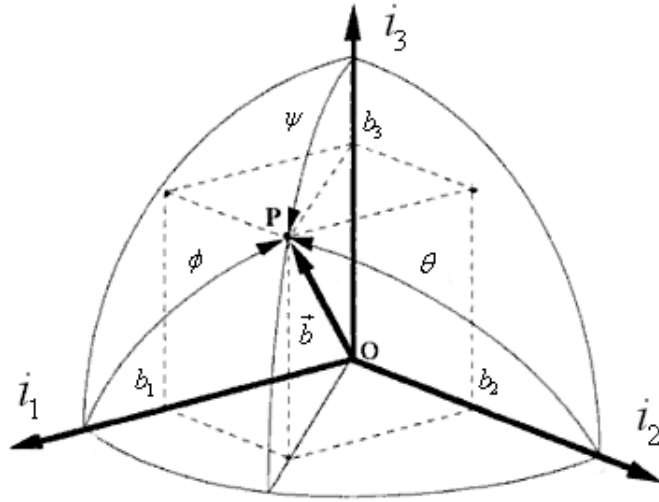


Figure 2.11: Orthonormal Coordinate Frame [25]

Choosing to express the unit vector \hat{b} in its component form \hat{b}_1 , \hat{b}_2 , and \hat{b}_3 a set of nine relational operators is revealed

$$\left\{ \begin{array}{ccc} \hat{i}_1 \cdot \hat{b}_1 & \hat{i}_1 \cdot \hat{b}_2 & \hat{i}_1 \cdot \hat{b}_3 \\ \hat{i}_2 \cdot \hat{b}_1 & \hat{i}_2 \cdot \hat{b}_2 & \hat{i}_2 \cdot \hat{b}_3 \\ \hat{i}_3 \cdot \hat{b}_1 & \hat{i}_3 \cdot \hat{b}_2 & \hat{i}_3 \cdot \hat{b}_3 \end{array} \right\} . \quad (2.29)$$

Thus, the rotation matrix \mathbf{R}^{ib} from the body frame $\{\hat{b}\}$ to the inertial frame $\{\hat{i}\}$ can be written as

$$\mathbf{R}^{\text{ib}} = \begin{bmatrix} \hat{i}_1 \cdot \hat{b}_1 & \hat{i}_1 \cdot \hat{b}_2 & \hat{i}_1 \cdot \hat{b}_3 \\ \hat{i}_2 \cdot \hat{b}_1 & \hat{i}_2 \cdot \hat{b}_2 & \hat{i}_2 \cdot \hat{b}_3 \\ \hat{i}_3 \cdot \hat{b}_1 & \hat{i}_3 \cdot \hat{b}_2 & \hat{i}_3 \cdot \hat{b}_3 \end{bmatrix} \quad (2.30)$$

or

$$\mathbf{R}^{\text{ib}} = \begin{bmatrix} R_{11} & R_{12} & R_{13} \\ R_{21} & R_{22} & R_{23} \\ R_{31} & R_{32} & R_{33} \end{bmatrix} \quad (2.31)$$

where

$$R_{ij} = \hat{i}_i \cdot \hat{b}_j = \cos \beta_{ij} \quad (2.32)$$

and β_{ij} is the angle ϕ , θ , or ψ defined in Figure 2.11 and solved for using Equation (2.28). Since the dot product is a scalar projection, \mathbf{R} can be referred to as a rotation matrix, a change of basis, or a projection of one orthonormal coordinate frame onto another.

At any given point in time, the rotation matrix can simply be used to convert from one reference frame to another. However, dynamically speaking, it is necessary to evaluate the motion of the body over a period of time. Looking at Equations (2.30)–(2.32), it is recognized that the orientation of the body at any given moment in time requires nine separate calculations—nine computationally expensive trigonometric calculations. Needless to say, rotation matrices are not the most efficient way to determine a spacecraft’s attitude. Therefore, alternate methods must be investigated.

2.3.2.2 Euler Angles . In the 18th century, Leonhard Euler (1707-1778) proved a theorem which guarantees the existence of sequences of three rotations which relate two independent coordinate frames:

Any two independent orthonormal coordinate frames can be related by a sequence of rotations (not more than three) about coordinate axes, where no two successive rotations may be about the same axis [15].

Euler angles are a sequence of three angles upon which a reference coordinate system’s axes are rotated. The final result is that the reference coordinate system has been transformed into some other basis. The axes of rotation are commonly referred to as the 1-, 2-, and 3- axis. Figure 2.12 illustrates a reference coordinate system $\{i_1 \ i_2 \ i_3\}$ that has undergone a 3-2-1 Euler rotation sequence. A preliminary rotation about the 3-axis generates the $\{a'_1 \ a'_2 \ a'_3\}$ basis, a penultimate 2-axis rotation generates the $\{a''_1 \ a''_2 \ a''_3\}$ basis, and finally the 1-axis rotation generates the transformed $\{b_1 \ b_2 \ b_3\}$ basis.

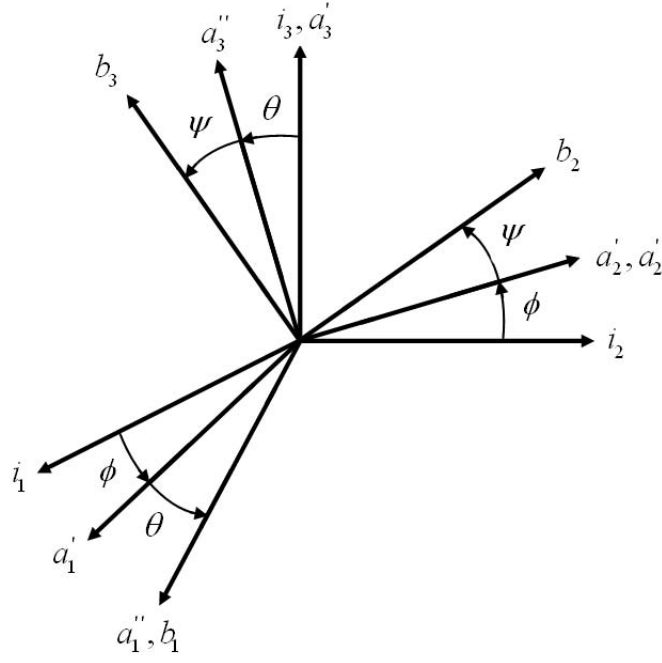


Figure 2.12: Euler Angles

Both the magnitude of the angles and the sequence of rotations are critical. If a different sequence is used, an entirely different solution can be obtained. After applying the limitation that no two successive rotations may be about the same axis, it is shown in Equation (2.33) that 12 possible Euler angle rotation sequences exist

$$\left\{ \begin{array}{ccc} 1-2-3 & 2-3-1 & 3-1-2 \\ 1-3-2 & 2-1-3 & 3-2-1 \\ 1-2-1 & 2-3-2 & 3-1-3 \\ 1-3-1 & 2-1-2 & 3-2-3 \end{array} \right\}. \quad (2.33)$$

A commonly used Euler rotation sequence in aerospace applications is the 3-2-1 rotation sequence [25]. The first rotation is about the 3-axis, followed by the 2-axis, then culminating with a rotation about the 1-axis. Figure 2.13 illustrates the 3-2-1 rotation sequence in three-dimensional space.

The aerospace Euler sequence is symbolically denoted by

$$\mathbf{R}_3(\phi) \longleftarrow \mathbf{R}_2(\theta) \longleftarrow \mathbf{R}_1(\psi)$$

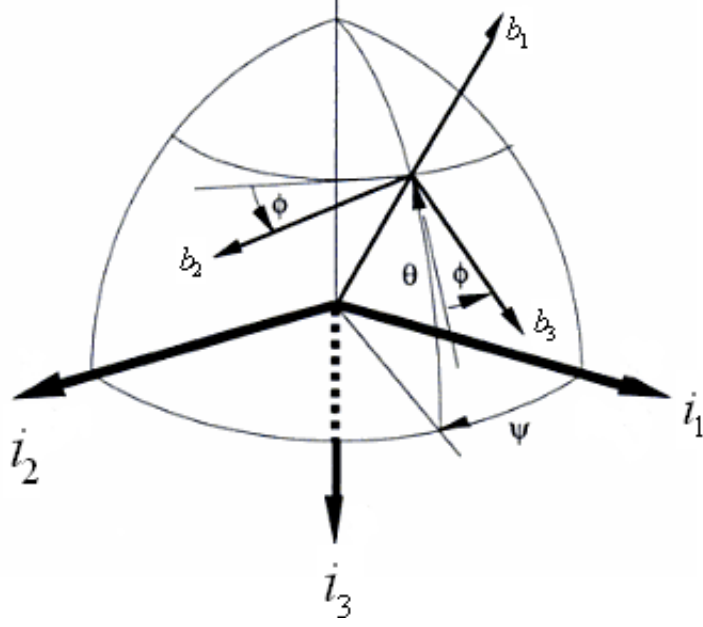


Figure 2.13: Aerospace Euler Sequence [25]

and mathematically denoted by Equation (2.34). For brevity, the trigonometric functions cos, sin, and tan are expressed as C , S , and T , respectively

$$\mathbf{R}_3(\phi)\mathbf{R}_2(\theta)\mathbf{R}_1(\psi) = \begin{bmatrix} 1 & 0 & 0 \\ 0 & C\phi & S\phi \\ 0 & -S\phi & C\phi \end{bmatrix} \begin{bmatrix} C\theta & 0 & -S\theta \\ 0 & 1 & 0 \\ -S\theta & 0 & C\theta \end{bmatrix} \begin{bmatrix} C\psi & S\psi & 0 \\ -S\psi & C\psi & 0 \\ 0 & 0 & 1 \end{bmatrix}. \quad (2.34)$$

By performing the matrix product, we can rewrite Equation (2.34) as

$$\mathbf{R}(\psi, \theta, \phi) = \begin{bmatrix} C\theta C\psi & C\theta S\psi & -S\theta \\ -C\phi S\psi + S\phi S\theta C\psi & C\phi C\psi + S\phi S\theta S\psi & S\phi C\theta \\ S\phi S\psi + C\phi S\theta C\psi & -S\phi C\psi + C\phi S\theta S\psi & C\phi C\theta \end{bmatrix}. \quad (2.35)$$

Equation (2.35) has now taken the form of a rotation matrix as mentioned in Section 2.3.2.1. If needed, the Euler angles can be extracted from Equation (2.35) as follows [6]:

$$\phi = T^{-1} \left(\frac{R_{23}}{R_{33}} \right) \quad (2.36a)$$

$$\theta = T^{-1} \left(\frac{-R_{13}}{\sqrt{1 - R_{13}^2}} \right) \quad (2.36b)$$

$$\psi = T^{-1} \left(\frac{R_{12}}{R_{11}} \right) . \quad (2.36c)$$

When attitude determination involves very small angles, the small-angle approximation can be made while simultaneously ignoring higher order terms, yielding

$$\mathbf{R}(\psi, \theta, \phi) = \begin{bmatrix} 1 & \psi & -\theta \\ -\psi & 1 & \phi \\ \theta & -\phi & 1 \end{bmatrix} . \quad (2.37)$$

To perform attitude control of SimSat II, one must know the orientation of the body-fixed reference frame relative to the ECI reference frame at any moment in time. Euler's equations, expressed as the time rate of change of the Euler angles, provide the tool to investigate the body-fixed reference frame's orientation at any moment in time. Again, consider the aerospace 3-2-1 Euler sequence.

The time derivatives of Euler angles, ϕ , θ , and ψ , called Euler rates, are denoted by $\dot{\phi}$, $\dot{\theta}$, and $\dot{\psi}$. This successive rotation is symbolically denoted by

$$\vec{\omega}_1 (\dot{\phi}) \longleftarrow \vec{\omega}_2 (\dot{\theta}) \longleftarrow \vec{\omega}_3 (\dot{\psi})$$

and is also represented mathematically as the angular velocity vector $\vec{\omega}$,

$$\begin{bmatrix} \omega_1 \\ \omega_2 \\ \omega_3 \end{bmatrix} = \begin{bmatrix} \dot{\phi} \\ 0 \\ 0 \end{bmatrix} + \mathbf{R}_1(\phi) \begin{bmatrix} 0 \\ \dot{\theta} \\ 0 \end{bmatrix} + \mathbf{R}_1(\phi) \mathbf{R}_2(\theta) \begin{bmatrix} 0 \\ 0 \\ \dot{\psi} \end{bmatrix} \quad (2.38a)$$

$$= \begin{bmatrix} 1 & 0 & -S\theta \\ 0 & C\phi & S\phi C\theta \\ 0 & -S\phi & C\phi C\theta \end{bmatrix} \begin{bmatrix} \dot{\phi} \\ \dot{\theta} \\ \dot{\psi} \end{bmatrix} . \quad (2.38b)$$

After inverting Equation (2.38), the Euler rates of the aerospace 3-2-1 Euler sequence can be expressed as Equation (2.39)

$$\begin{bmatrix} \dot{\phi} \\ \dot{\theta} \\ \dot{\psi} \end{bmatrix} = \frac{1}{\cos \theta} \begin{bmatrix} \cos \theta & S\phi S\theta & C\phi S\theta \\ 0 & C\phi C\theta & -S\phi C\theta \\ 0 & S\phi & C\phi \end{bmatrix} \begin{bmatrix} \omega_1 \\ \omega_2 \\ \omega_3 \end{bmatrix}. \quad (2.39)$$

If ω_1 , ω_2 , and ω_3 are known as functions of time, then the orientation of SimSat II's body-fixed reference frame relative to the ECI reference frame can be determined by solving Equation (2.39). A note of caution: Equation (2.39) becomes singular when θ equals $\pm(\pi/2)(n+1)$ where n is an even integer. Such singularities can be avoided by selecting an alternate Euler rotation sequence; however, all Euler rotation sequences experience a singularity of some form or another. Alternatively, the 3-1-3 Euler rotation sequence shall be examined. Its Euler rate is presented as

$$\begin{bmatrix} \dot{\phi} \\ \dot{\theta} \\ \dot{\psi} \end{bmatrix} = \frac{1}{\sin \theta} \begin{bmatrix} S\psi & C\psi & 0 \\ C\psi S\theta & -S\psi S\theta & 0 \\ -S\psi C\theta & -C\psi C\theta & 0 \end{bmatrix} \begin{bmatrix} \omega_1 \\ \omega_2 \\ \omega_3 \end{bmatrix}. \quad (2.40)$$

The 3-1-3 Euler rotation sequence experiences a singularity when θ equals $\pm\pi n$ where n is any whole number. In all, the Euler angle rotation sequences listed in Equation (2.33) fall into either one of two categories, symmetric or asymmetric. The symmetric Euler angle sequences (1-2-1, 2-3-2, 3-1-3, etc.) incur a singularity when θ equals $\pm\pi n$. The asymmetric Euler angle sequences (1-2-3, 2-3-1, 3-2-1, etc.) incur a singularity when θ equals $\pm\pi/2$. Rotation sequence singularities are a disadvantage of using Euler angles for large-angle reorientation maneuvers.

As previously described in Section 2.2, the design of SimSat II affords it unconstrained, 360° motion about the 3-axis. Its motion is constrained about the 1- and 2-axes to angles less than approximately $\pm 30^\circ$ measured from horizontal. Whereas symmetric Euler angle sequences make SimSat II vulnerable to singularities, the $\pm 30^\circ$ constrained motion about the 1- and 2-axis allow asymmetric Euler angle sequences to perform

without singularities. Needless to say, an asymmetric Euler sequence was chosen for SimSat II. French used SIMULINK to develop and implement the 3-2-1 Euler sequence for SimSat I [17]; the model has proven to be reliable throughout multiple AFIT master’s studies and was used for this research effort.

Ultimately, Euler angles still require computationally expensive trigonometric expressions to be solved. However, the advantage to Euler angles is that they provide a method in which one coordinate reference frame can be transformed into another while avoiding possible singularities.

2.3.3 Satellite Three-Axis Control . Satellite three-axis control requirements can be extraordinarily stringent. For example, the Hubble Telescope requires a pointing accuracy of two-millionths of a degree [4]. The level of control torque that can be achieved with reaction thruster systems is almost unbounded; however, no smooth control can be achieved with reaction thruster systems due to their inherent impulsive nature [48]. For spacecraft outfitted with an ACS that generates reaction forces produced by the expulsion of gas, disturbance torques cause a steady drain on the finite fuel supply. When the fuel tank expends its fuel, refilling is not an option. Fuel consumption was the cause of death of every National Aeronautics and Space Administration (NASA) Mariner and Viking deep-space probe [52]. There are, however, attitude control devices capable of controlling the attitude of a spacecraft without using a spacecraft’s finite fuel supply. The reaction wheel is one such commonly used device.

2.3.3.1 Reaction Wheels . For a highly accurate ACS and moderately fast maneuverability, reaction wheels are preferred because they allow continuous and smooth control while inducing the lowest possible parasitic disturbance torques. The amount of torque that can be achieved with reaction wheels is on the order of 0.05–2 N · m [48]. Torque is not generated due to the instantaneous angular rate of the reaction wheel ψ_w , rather it is because of the instantaneous change in angular rate $\dot{\psi}_w$.

Reaction wheels are momentum exchange devices. They trade angular momentum back and forth with their host spacecraft by leveraging the principle of conservation of momentum, which states that the total momentum of a closed system is constant,

$$\vec{H}_{tot} = \vec{H}_b + \vec{H}_w = \text{constant} , \quad (2.41)$$

where \vec{H}_b is the angular momentum of the spacecraft and \vec{H}_w is the angular momentum of the reaction wheels. Using Equation (2.19) the angular momentum of the spacecraft body can be expressed as

$$\vec{H}_b = \mathbf{I}\vec{\omega} \quad (2.42)$$

and the angular momentum of the reaction wheels as

$$\vec{H}_w = D_w \vec{\psi}_w \quad (2.43)$$

where \mathbf{I} is the MOI matrix of the spacecraft body, $\vec{\omega}$ is the angular rotation rate of the spacecraft body, and D_w is the principal MOI of the reaction wheel with respect to its axis of rotation. The applied torque about the reaction wheel \vec{M}_w can therefore be expressed as

$$\vec{M}_w = \dot{\vec{H}}_w \quad (2.44a)$$

$$= D_w \dot{\vec{\psi}}_w . \quad (2.44b)$$

The maximum amount of angular momentum \vec{H}_{max} a spacecraft is capable of storing within its closed system occurs when the angular rate ψ_w of its reaction wheel ACS reaches its rotational rate limit $\psi_{w_{max}}$. When this condition is met the reaction wheel is deemed saturated, incapable of generating an input torque to counteract a given disturbance torque. To restore the reaction wheel's capability of producing instantaneous changes in angular rate (torque), the reaction wheel must be aided by an external momentum device in a procedure referred to as *momentum dumping*.

At least three reaction wheels are required for controlling a spacecraft's attitude about all three axes in space. If the minimum number of reaction wheels are used, they

must be configured orthogonally for three-axis control. For full redundancy however, this configuration has the disadvantage of requiring two wheels per body axis. With each additional reaction wheel, a penalty in power, weight, and expense to field the system is incurred. A more common approach to achieving redundancy is to assemble four reaction wheels into a tetrahedron configuration [20]. SimSat II is equipped with three reaction wheels configured orthogonally. The momentum \vec{H} and torque \vec{M} vectors generated by the reaction wheels with respect to the SimSat II body axes are illustrated in Figure 2.14.

Incorporating the reaction wheel ACS into Euler's EOM for a rigid body, Equation (2.25) becomes

$$M_1 = A\dot{\omega}_1 + (D_w\dot{\psi}_w)_1 + (C - B)\omega_2\omega_3 - (D_w\psi_w)_2\omega_3 + (D_w\psi_w)_3\omega_2 \quad (2.45a)$$

$$M_2 = B\dot{\omega}_2 + (D_w\dot{\psi}_w)_2 + (A - C)\omega_1\omega_3 + (D_w\psi_w)_1\omega_3 - (D_w\psi_w)_3\omega_1 \quad (2.45b)$$

$$M_3 = C\dot{\omega}_3 + (D_w\dot{\psi}_w)_3 + (B - A)\omega_1\omega_2 - (D_w\psi_w)_1\omega_2 + (D_w\psi_w)_2\omega_1 . \quad (2.45c)$$

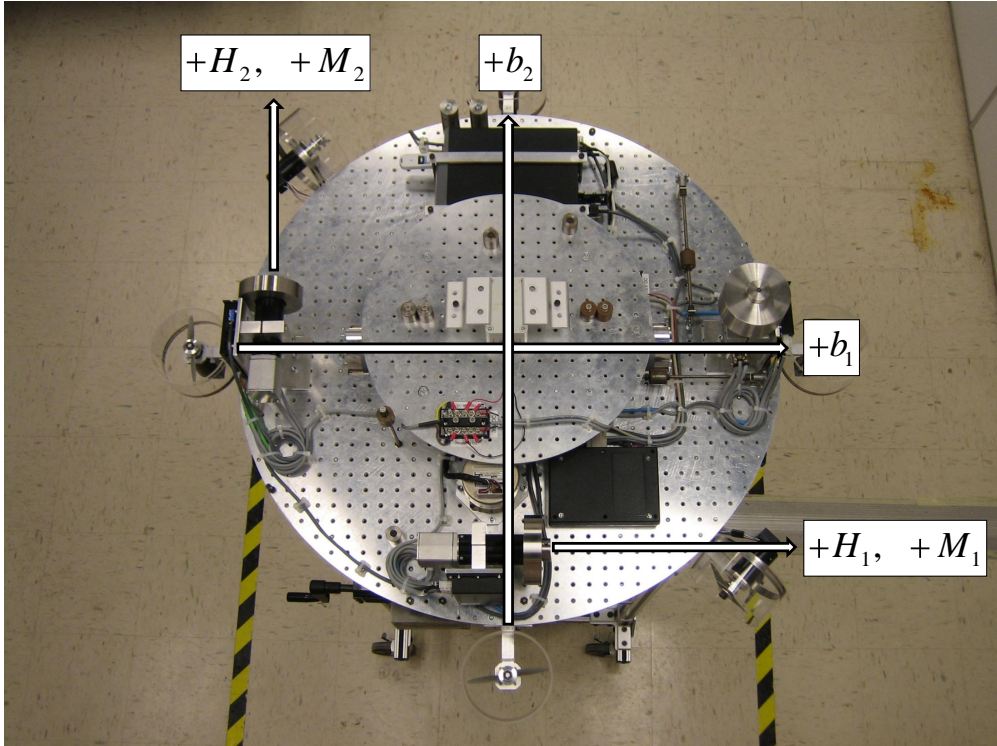


Figure 2.14: SimSat II Momentum and Torque Vectors

Equation (2.45) is the general case of a satellite having a principal MOI matrix and possessing three reaction wheels in which the axes of rotation are parallel to the 1, 2, and 3 spacecraft body axes.

Once again, visiting the principle of conservation of angular momentum, the torque generated by the reaction wheels M_w will cause an equal and opposite reaction torque from the spacecraft $-M_b$. Typically, the MOI of the reaction wheel is much smaller than that of the spacecraft. Therefore, it requires a large change in the angular velocity of the reaction wheel $\Delta\vec{\psi}_w$ to produce a moderate opposing angular velocity of the spacecraft $\Delta\vec{\omega}$. This ratio of delta angular rates is what gives the reaction wheel ACS its sensitivity, which in turn allows the reaction wheels to eliminate small, unwanted spacecraft rotational rates with ease.

2.4 *PID Attitude Control*

The inherent usefulness of PID controls is their general applicability to most control systems. In particular, when the transfer function of the plant is unknown, and therefore, analytical controller design methods are not applicable, PID controls have proven to be most helpful. In the field of process control systems, it is well known that PID control has established a reputation of providing satisfactory control, although in many given situations it may not provide optimal control. PID control has the noteworthy distinction of comprising more than one-half of the industrial controllers in use today [34].

PI control eliminates error $err(s)$ and gives good steady-state behavior for both reference $\beta_{com}(s)$ and disturbance $D(s)$ inputs. The dynamic response, however, is much slower than that of PD control. To achieve favorable steady-state and dynamic responses $\beta(s)$ one can combine PI and PD control into one controller via PID control (see Figure 2.15) [7].

Generally speaking, satellite attitude dynamics EOM are three second-order non-linear equations—Euler’s equations (Equation (2.25)). Automatic control theory does not provide exact analytical solutions and design procedures for such dynamic plants, so linearization of these equations is necessary if standard automatic control techniques are to be used [48].

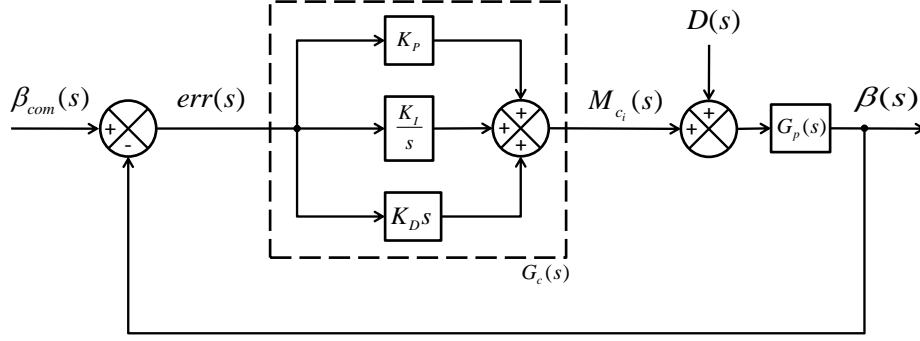


Figure 2.15: PID Controller Block Diagram

Remembering that angular velocity ω is the time derivative of angular position β , Equation (2.25) shows that the plant $G_p(s)$ with respect to a single satellite body axis, consists of two integrators. Control torque inputs M_c are necessary to control such a system. These torques can be produced passively (e.g., gravity) or in SimSat II's case, actively using controller hardware.

Control torque inputs are generally a function of attitude errors. Since SimSat II is modeled as a second-order system, damping control must be provided for improved stability. This means the control torques must include a derivative term that is dependent upon the attitude rates being measured. In addition, if steady-state error is to be nulled, an integral term is necessary in the control logic. The control torque equations of a PID controller expressed in the time domain are written as:

$$M_{c_i} = K_{P_i} (\beta_{com} - \beta) + K_{D_i} \frac{d}{dt} (\beta_{com} - \beta) + K_{I_i} \int (\beta_{com} - \beta) dt \quad (2.46a)$$

$$= K_{P_i} (\beta_{err}) + K_{D_i} \frac{d}{dt} (\beta_{err}) + K_{I_i} \int (\beta_{err}) dt \quad (2.46b)$$

where i denotes 1, 2, or 3 for each of the three body axes. The variables K_{p_i} , K_{i_i} , and K_{D_i} are the proportional, integral, and derivative gain settings, respectively. The transfer function of a PID controller expressed in the complex-frequency domain is written as

$$G_c(s) = K_P + \frac{K_I}{s} + K_D s. \quad (2.47)$$

Tuning K_{p_i} , K_{i_i} , and K_{D_i} for SimSat II's PID controller is discussed in further detail in Section 3.4.8.

Hines designed a linearized PID controller using SIMULINK and implemented his model on SimSat I [21]. This framework has since remained intact and has been incorporated for use upon SimSat II. The PID controller is used within this research to demonstrate reorientation response as well as position accuracy. Due to the linearization of the PID controller, SimSat II cannot rotate about the 3-axis any more than approximately $\pm 40^\circ$ without exceeding its controllable limits. The physical rotational constraints about the 1- and 2-axis of SimSat II, less than $\pm 30^\circ$, prevent the instance of instability from occurring. One minor change was performed to Hines' PID controller. During the build phase of this research, the LN-200 inertial measurement unit (IMU) was reoriented on SimSat II's tabletop deck. The PID controller now accounts for the IMU's reorientation.

2.5 Summary

Chapter II presented a review of relevant literature pertaining to the topics concerning this thesis. Here, an overview of satellite simulator styles was given as well as several satellite simulator research efforts conducted across academia. The type of ACS used for each satellite simulator research effort was highlighted and, specifically, previous satellite simulator research efforts conducted by AFIT was presented. Literature on spacecraft dynamics and PID attitude control was also presented in this chapter.

III. Methodology

Chapter III will first introduce the hardware and software on-board SimSat II. Subsequent discussion items include the purposes of the hardware and software subsystems and the interfaces among them. Also presented in Chapter III are the system characterization efforts performed throughout the design, build, and test objectives of this research.

3.1 *SimSat II Hardware*

The SimSat II spacecraft dynamics and control testbed designed and built by Roach *et al.* consists of three major hardware systems [40]:

1. A ground station (Figure 3.1)
2. A tri-axial air-bearing (Figure 3.2)
3. SimSat II satellite simulator (Figure 3.4)

3.1.1 Ground Station . A custom built personal computer (PC) runs the Windows XP® 32-bit operating system. Analogous to any satellite command and control setup, the PC functions as the ground station within the SimSat II testbed construct. Its primary purpose is to administer control inputs to the satellite simulator. The ground station PC communicates wirelessly to the Mini-box PC aboard SimSat II using a Linksys wireless-G broadband router. From the ground station, an operator can log onto the Mini-box PC remotely through the Windows remote desktop connection (RDC) resident to Windows XP; whereupon, commands can be issued, data can be uploaded to SimSat II's on-board computer, and measurements collected by SimSat II can be downlinked to the



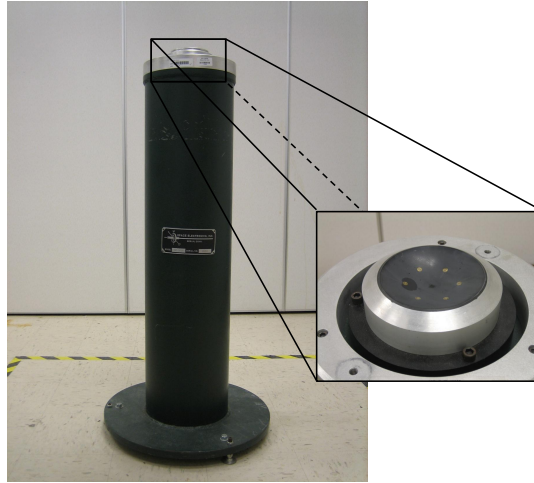
Figure 3.1: SimSat II Groundstation

ground station for post-processing. The operating specifications of the ground station PC are presented in Table 3.1.

Table 3.1: SimSAT II Ground Station PC Specifications

Operating System	Windows XP 32-bit
Processor	Intel Core i7 2.66GHz Quad-Core Processor
Motherboard	BIOSTAR Intel X58 ATX Motherboard
Memory	4GB DDR3 SDRAM
Hard Disk Space	240 GB
Video	Radeon x850 Series
Wireless	Linksys Wireless-G Broadband Router

3.1.2 Air Bearing . SimSat II uses the Space Electronics, Inc. model SE-9791 tri-axis spherical air-bearing. This model of air-bearing consists of a precision rotor and stator that are of equal radii of curvature and separated by a cushion of air that is less than 0.0005 in thick. The cushion of air is maintained through jewel orifices that meter the air flow and provide dynamic centering of the rotor [3]. The system specifications and stator, housing the jewel orifices atop the pedestal, are shown in Figure 3.2.



Ball Bearing Diameter	22.00	cm
Pedestal Cup Diameter	5.72	cm
Unloaded Ball Bearing Mass	19.05	kg
Maximum Loading	136.08	kg

Figure 3.2: Space Electronics, Inc. Tri-Axis Spherical Air-Bearing

The tabletop-style deck of SimSat II is attached to the precision rotor by two metallic rod extrusions as shown in Figure 3.3. SimSat II is restricted to approximately $\pm 30^\circ$ rotation about the 1- and 2-axis whereas it has unconstrained 360° rotational DOF about the 3-axis.

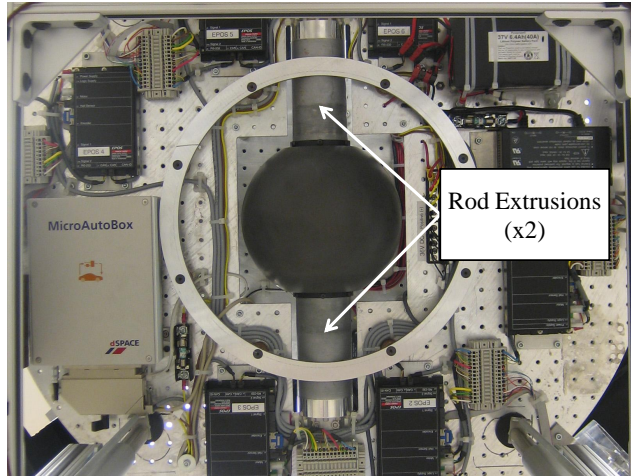
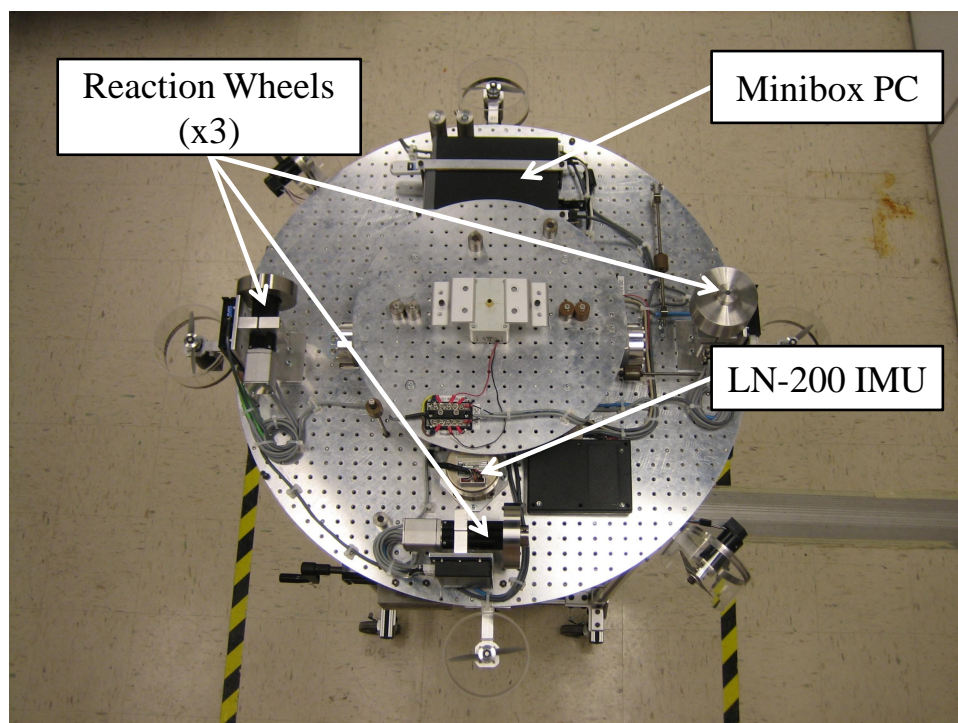


Figure 3.3: SimSat II Tabletop Deck Fastenings

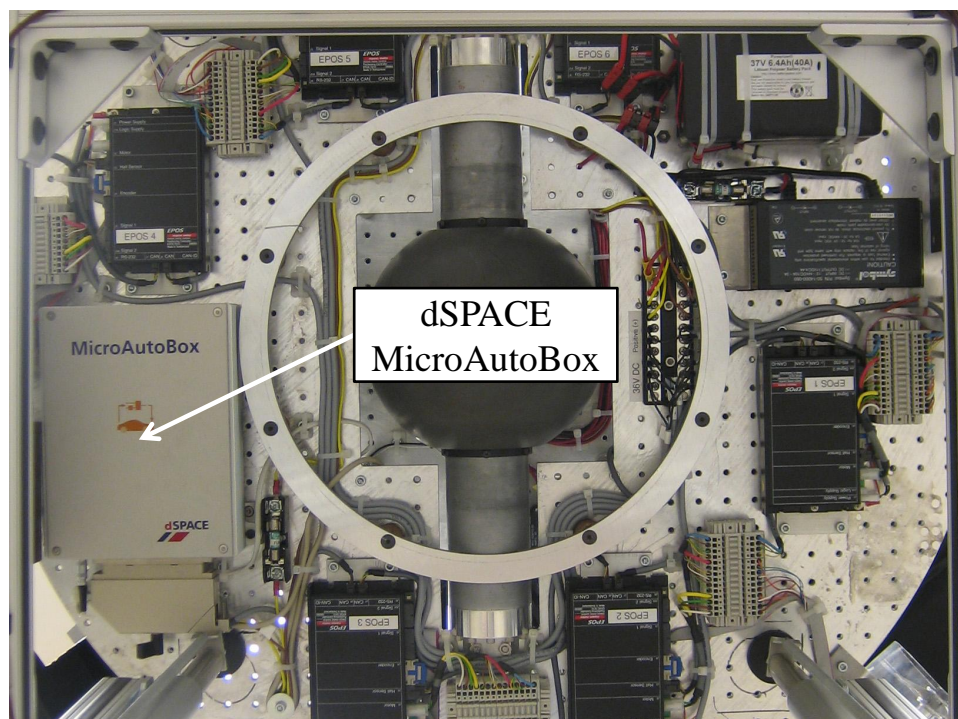
3.1.3 SimSat II. The SimSat II satellite simulator is comprised of four major subsystems:

1. Mini-Box PC (Figure 3.5)
2. dSPACE MicroAutoBox (Figure 3.6)
3. Northrop Grumman LN-200 Fiber Optic Gyroscope IMU (Figure 3.7)
4. Maxon Motor Reaction Wheel Assembly (Figure 3.8)

Each of these subsystems are identified in Figure 3.4 and discussed in detail in the remaining subsections of Section 3.1.3. For information pertaining to any subsystems not mentioned, refer to the thesis work of Roach *et al.* [40].



(a) SimSat II from Above



(b) SimSat II from Below

Figure 3.4: SimSat II

3.1.3.1 Mini-Box PC[®] . Sim-

Sat II's Mini-box PC is mounted to the top-side of the tabletop deck as seen in Figure 3.4(a). The Mini-box PC serves two functions. In its primary role, the Mini-box PC controls the SIMULINK software used to develop command and control algorithms for SimSat II. This particular license of SIMULINK is special because of its interoperability with previous AFIT students' theses. The sec-

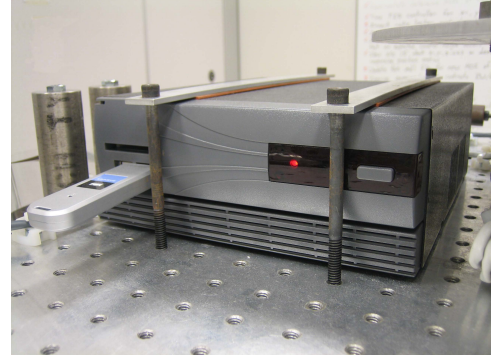


Figure 3.5: Mini-box PC

ondary role of the Mini-box PC is that of go-between from the ground station to the dSPACE MicroAutoBox. The operator communicating wirelessly from the ground station to the Mini-box PC via the Linksys 802.11 router constructs a SIMULINK .mdl model file and compiles it into a C-coded file format agreeable with the dSPACE MicroAutoBox. The operator is then able to transfer the C-coded file to the dSPACE MicroAutoBox for simulation testing. The system specifications for the Mini-box PC are listed in Table 3.2.

Table 3.2: Mini-Box PC Specifications

Operating System	Windows XP 32-bit
Processor	x86 1500 MHz
Motherboard	Jetway Hybrid MicroATX
Memory	1024 MB
Hard Disk Space	40 GB
Wireless	Linksys Compact Wireless USB Network Adapter

3.1.3.2 dSPACE MicroAutobox . The dSPACE MicroAutoBox is mounted

to the bottom-side of the tabletop deck as seen in Figure 3.4(b); it exclusively executes SIMULINK model files that have been previously compiled into a C-coded format. The dSPACE MicroAutoBox is connected directly to the Mini-box PC, therefore, providing real-time control of SimSat II's controllable hardware via dSPACE ControlDesk software. Hardware characteristics of the dSPACE MicroAutoBox can be seen in Figure 3.6.



Weight	2.15	kg
Width	182	mm
Length	192.6	mm
Height	50	mm
Power Consumption	30	W

Figure 3.6: dSPACE MicroAutoBox

3.1.3.3 LN-200 Fiber Optic Gyroscope

IMU . Northrop Grumman's LN-200 IMU pictured in Figure 3.7 is mounted to the top-side of the tabletop deck as seen in Figure 3.4(a). The LN-200 is used to collect angular acceleration measurements $\vec{\alpha}$ of the spacecraft body. These measurements are then used to determine the spacecraft's attitude. The LN-200 consists of three fiber optic gyros (FOG). An FOG consists of a spool of fiber optic cable. A laser diode is used to transmit light from either end of the fiber optic cable. The LN-200 uses the principles of ring interferometry and the Sagnac effect [42] to measure its angular velocity. By mounting the LN-200 to SimSat II the angular acceleration of the spacecraft can be accurately measured. Hardware specifications for the LN-200 IMU are presented in Table 3.3.



Figure 3.7: Northrup Grumman LN-200 Fiber Optic Gyroscope IMU

The LN-200 cannot send its angular acceleration measurements directly to the dSPACE MicroAutoBox because of a data protocol mismatch. The data protocol native to the LN-200 is RS-485, and SimSat II can only read RS-232. To convert the RS-485 data to RS-232 the LN-200 connects to an interface board manufactured by SkEyes Unlimited Corporation. The interface board performs an integration of the measured

acceleration, converts the synchronous data link control (SDLC) analog signal from the LN-200 into a 21-byte data packet, and then transmits the resultant angular velocity $\vec{\omega}$ value over RS-232 to the dSPACE MicroAutoBox.

Table 3.3: Northrop Grumman LN-200 IMU

Weight	700	g
Diameter	8.9	cm
Height	8.5	cm
Power Consumption	10	W
Bias Repeatability	1-10	hr ⁻¹
Random Walk	0.04-0.1	° hr ^{1/2} power spectral density
Data Latency	<1	ms

3.1.3.4 Maxon Motor Reaction Wheel Assembly . The reaction wheel assembly consists of a reaction wheel and electric motor with encoder, a mounting bracket that anchors the electric motor to SimSat II's tabletop deck, and a controller that commands angular rates to the electric motor (see Figure 3.8).

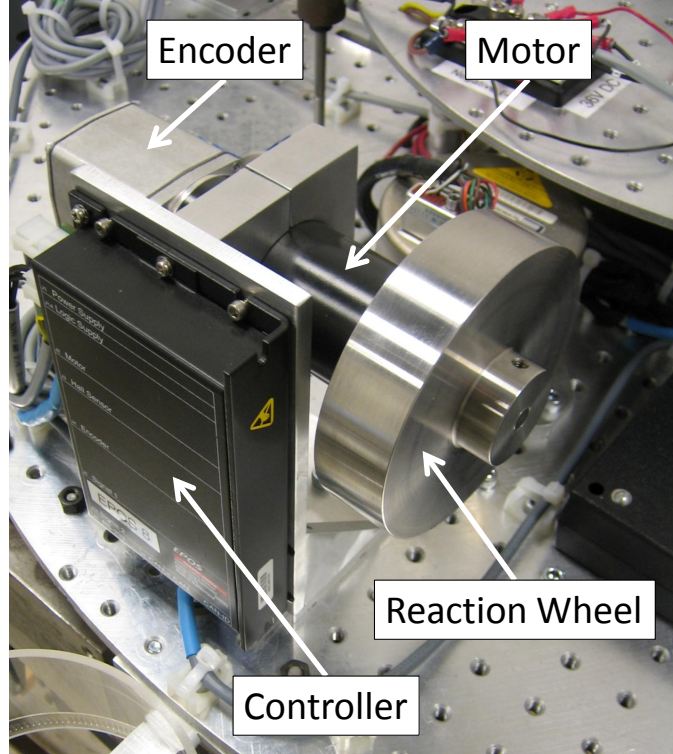


Figure 3.8: Maxon Motor Reaction Wheel Assembly

First, a preliminary bracket was designed to attach the electric motor and reaction wheel to SimSat II. As seen in Figure 3.9(a), the preliminary bracket consists of (A) a motor mount, (B) a vertical plate, and (C) a base plate. The motor mount is a two-piece compression clasp that can be oriented either parallel or perpendicular to SimSat II's tabletop deck for attitude control about the 1-, 2- or 3-axis. The backside of the vertical plate is where the controller is attached, and the base plate is where the bracket is affixed to SimSat II.

After a trial build was completed, two design changes were made to the bracket. The resultant bracket design is shown in Figure 3.9(b). The material thickness of the motor mount (A) was increased from 0.5 in to 1.0 in to improve the orthogonal trueness between the motor mount and electric motor. Additionally, 45° wedges of material were inserted between the vertical plate (B) and base plate (C) to increase the rigidity of the bracket and decrease the possibility of flexing.

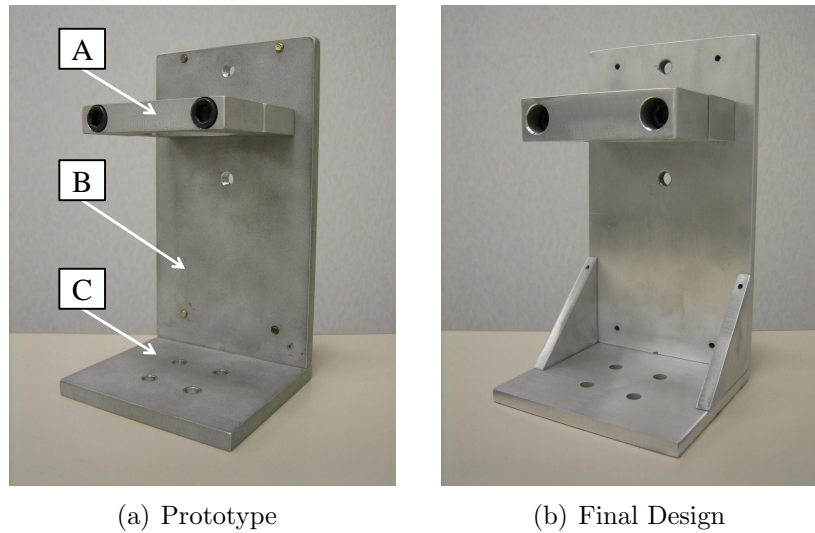


Figure 3.9: Reaction Wheel Assembly Bracket

Lastly, the reaction wheel assembly was outfitted with a device to send control inputs to the electric motor (controller) and a separate device used in the measurement of the rotation rate of the electric motor shaft (encoder). The Maxon EPOS 70/10 controller was selected for control authority of the electric motor [31]. In 2008, while constructing SimSat II, Roach *et al.* selected the Maxon EPOS 70/10 controller to control the fan thruster ACS. The EPOS 70/10 operates in velocity mode with precise

motor speed control and supports the control area network (CAN) interface necessary to communicate with the dSpace MicroAutoBox. The encoder chosen for the reaction wheel assembly is the Maxon HEDL 9140. It is the only encoder available for the EC 45 electric motor.

3.2 *SimSat II Software*

For this research, the SimSat II spacecraft dynamics and control testbed relied primarily upon three software applications:

1. EPOS User Interface[®]
2. SIMULINK[®]
3. dSPACE Control Desk[®]

3.2.1 EPOS User Interface[®] . The EPOS User Interface is resident on the Mini-box PC. It is a proprietary software application provided by Maxon Motor for use with their EPOS line of controllers. The software application is used to configure the EPOS controller to the user's specifications. After connecting the EPOS 70/10 to SimSat II's CAN, the user must first select the Firmware Download Wizard and install the proper firmware so that the integrated controller is compatible with the six EPOS 70/10 controllers previously installed by Roach *et al.* [40]. The correct firmware file is Epos.2022h_6410h_0000h_0000h.bin located on the Mini-box PC.



Figure 3.10: EPOS User Interface Wizards

Upon conclusion of the firmware installation, the user must then run the Startup Wizard to input the specifications of the motor and encoder. These specifications can easily be found on the catalog pages for the motor and encoder [30, 32].

The last step in the EPOS 70/10 configuration process is accessed through the Regulation Tuning Wizard. The user has the option of tuning the EPOS' current, velocity, or position controller settings. This research only used the velocity controller. Methods for tuning the controller can be found in the EPOS 70/10 *Getting Started* document [28].

If the user chooses to operate the velocity controller then there are two operating modes from which to choose. As seen in Figure 3.11, the user can choose either *Profile Velocity Mode* or *Velocity Mode*. The difference being that Profile Velocity Mode provides the user with the ability to select the acceleration curve profile and limit the acceleration and deceleration rate of the controlled actuation device. This research exclusively used Velocity Mode. The software defined default acceleration rate in Velocity Mode is 10,000 rpm/s.

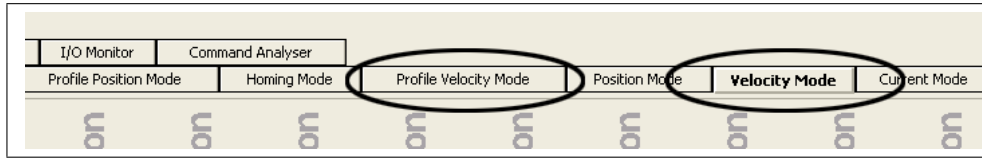


Figure 3.11: EPOS User Interface Velocity Modes

An alternate method to Profile Velocity Mode for setting acceleration rates is to use SIMULINK. The benefit of imposing acceleration rates using SIMULINK presents itself during testing. If the user were to command an acceleration limit to the EPOS 70/10 controller using Profile Velocity Mode, the possibility exists that the acceleration limit value(s) is not received. Limits established in SIMULINK are definite—meaning that the EPOS 70/10 controller will not command greater acceleration rates than those declared. The convenience of declaring acceleration rates in SIMULINK easily mitigates possible communications errors and consequent hardware failures.

Lastly, before performing attitude control of SimSat II, the user must first launch the EPOS User Interface and perform a systems inspection checklist. If this is not addressed, the user will experience inexplicable behavior from the actuating devices because their initial states can be arbitrary i.e., a mode other than Velocity Mode. Figure 3.12 aids in understanding the checklist procedure.

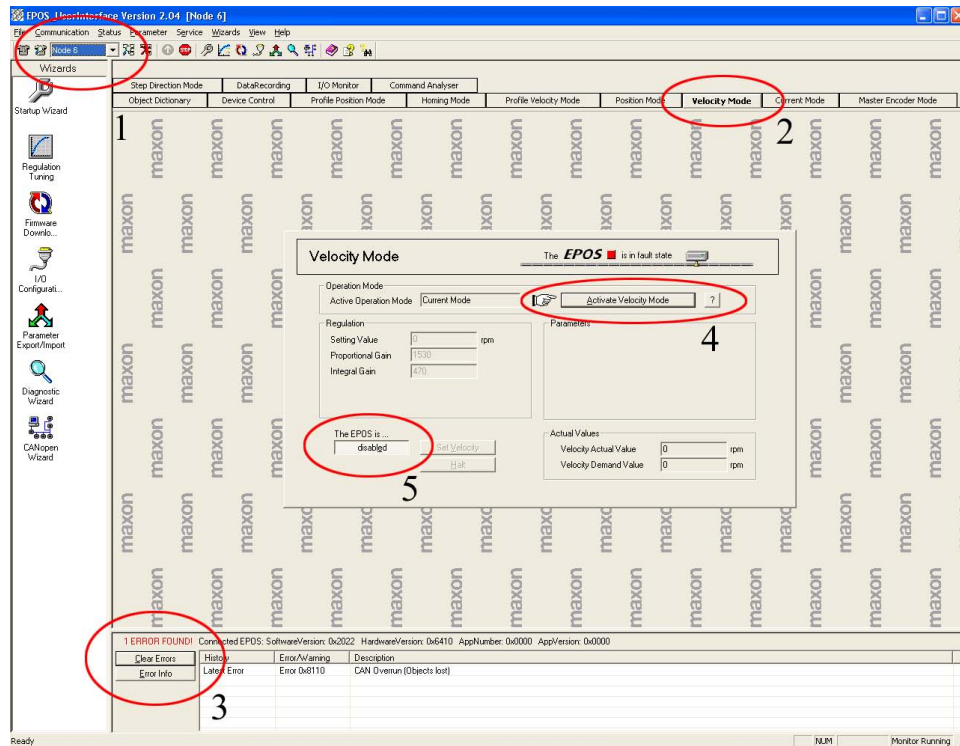
Item 1 of Figure 3.12(a) is the drop-down selector for all the nodes included on the CAN bus. A best practice is that items 2–5 of Figure 3.12(a) be addressed for every node included in the drop-down selector. Item 2 addresses which mode the selected controller will operate in. The mode tab that is appropriate for the particular application of the EPOS 70/10 controller should be selected. Item 3, the *clear errors* button, is located in the lower-left corner of Figure 3.12(a). The EPOS 70/10 controllers cannot be commanded if errors exist. Although item 2 addressed which mode the selected controller will operate in, the mode itself is not active until item 4 is depressed.

Item 5 enables the EPOS controller. Velocity inputs can be commanded directly from the EPOS User Interface or via SIMULINK when the controllers are enabled. Using the EPOS User Interface to command velocity inputs is particularly useful to test whether or not the hardware has been assembled correctly if SimSat II's SIMULINK model is not functioning properly.

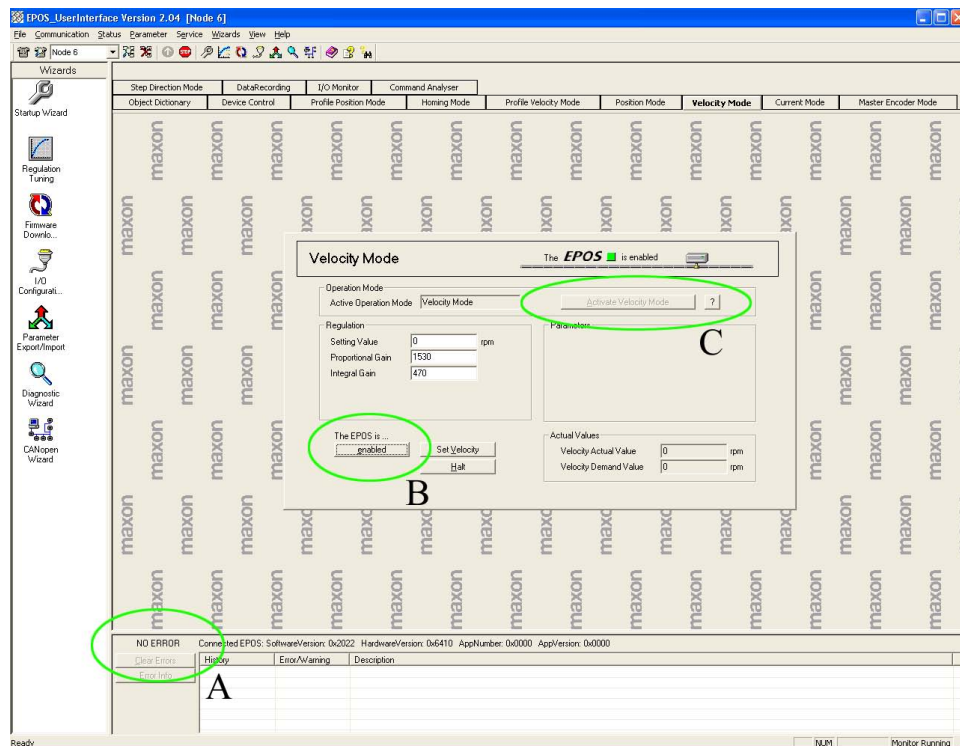
The EPOS User Interface affords the operator the ability to save all configuration parameters; however, for unknown reasons the selected operating mode is not captured. Upon opening the EPOS User Interface, the user will likely discover that the mode(s) previously in use have since been deactivated or changed to another mode. The ability to activate a mode using SIMULINK is unknown at this time. No literature was discovered that either confirmed or denied this capability.

When issuing a SIMULINK velocity command to the EPOS 70/10 controller, the operating mode is embedded in the issued command. However, if the mode presently activated in the EPOS User Interface does not match that of the issued SIMULINK command, actuation does not occur. The issuance of SIMULINK commands is covered further in Section 3.2.2.

After completing the systems inspection checklist, each node on the CAN bus is in a ready operating state. As seen in Figure 3.12(b), item A indicates there are zero errors, item B reveals that the node has been enabled, and the greyed out status of item C confirms that the node's mode is active.



(a) Before



(b) After

Figure 3.12: EPOS Systems Inspection Checklist

3.2.2 SIMULINK® . SIMULINK is a commercial tool for design and simulation of dynamic systems. Version 6.2 is installed on the Mini-box PC. SIMULINK uses a graphical interface accompanied by a customizable set of block libraries that allow the user to design, simulate, implement, and test a variety of time-varying systems—including controls. SIMULINK offers compatibility with the MATLAB® environment. Both SIMULINK and MATLAB are produced by the MathWorks™ software development company.

SIMULINK provides an environment in which a dynamic model of SimSat II can be created. After developing a working model, the SIMULINK Real-Time Workshop® toolbox is used to compile the model into stand-alone C code for development and testing. The stand-alone C code is then manipulated in a real-time environment using the dSPACE ControlDesk software application discussed in Section 3.2.3. Figure 3.13 shows a root-level view of the SIMULINK model used to command and control SimSat II.

SimSat II's SIMULINK model provides six basic functions:

1. Collect angular velocity measurements from by the LN-200 FOG IMU interface board.
2. Translate LN-200 angular velocity measurements into angular position.
3. Execute angular position and angular velocity user inputs.
4. Render PID control of the SimSat II satellite testbed.
5. Perform precautionary emergency shutdown of the reaction wheel ACS.
6. Issue angular velocity inputs to the reaction wheel ACS.

This research focused on the development of items 5–6; which are discussed in greater detail in Sections 3.4.3.4 and 3.4.4.

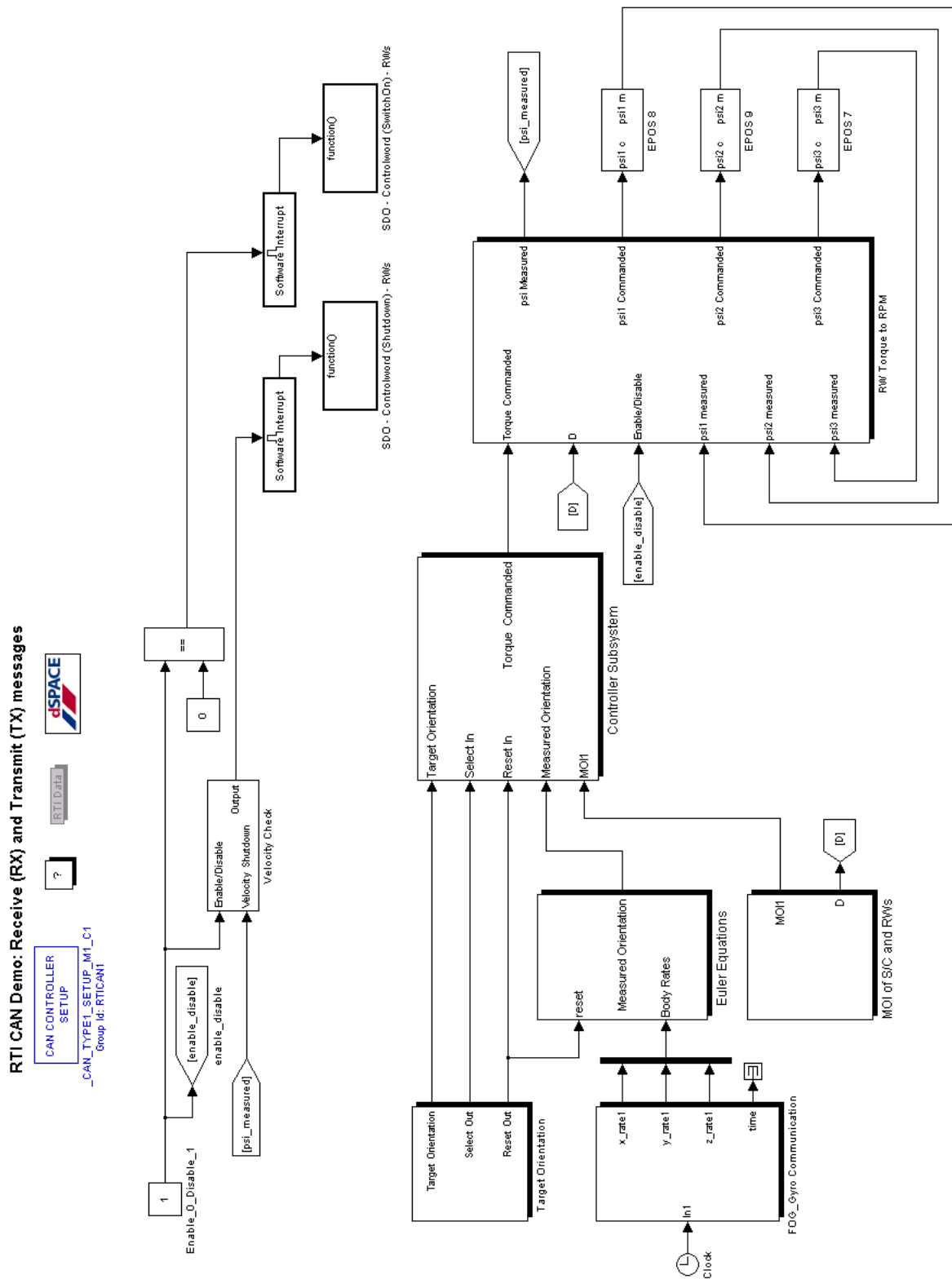


Figure 3.13: SimSat II Root-Level SIMULINK Model

3.2.3 *dSPACE ControlDesk*[®]. dSPACE ControlDesk is used to manage and instrument real-time SIMULINK models. The graphical user interface of the dSPACE ControlDesk allows the user to construct experiments and instrumentation layouts that aid in the test and evaluation of their SIMULINK model [12, 13]. dSPACE ControlDesk is installed on the Mini-box PC and is the means by which the stand-alone SIMULINK C code is uploaded to the dSPACE MicroAutoBox. Figure 3.14 is an example layout used during this research. Section 3.4.8 highlights a specific example of how the dSPACE ControlDesk was used to test and evaluate the SimSat II satellite simulator.

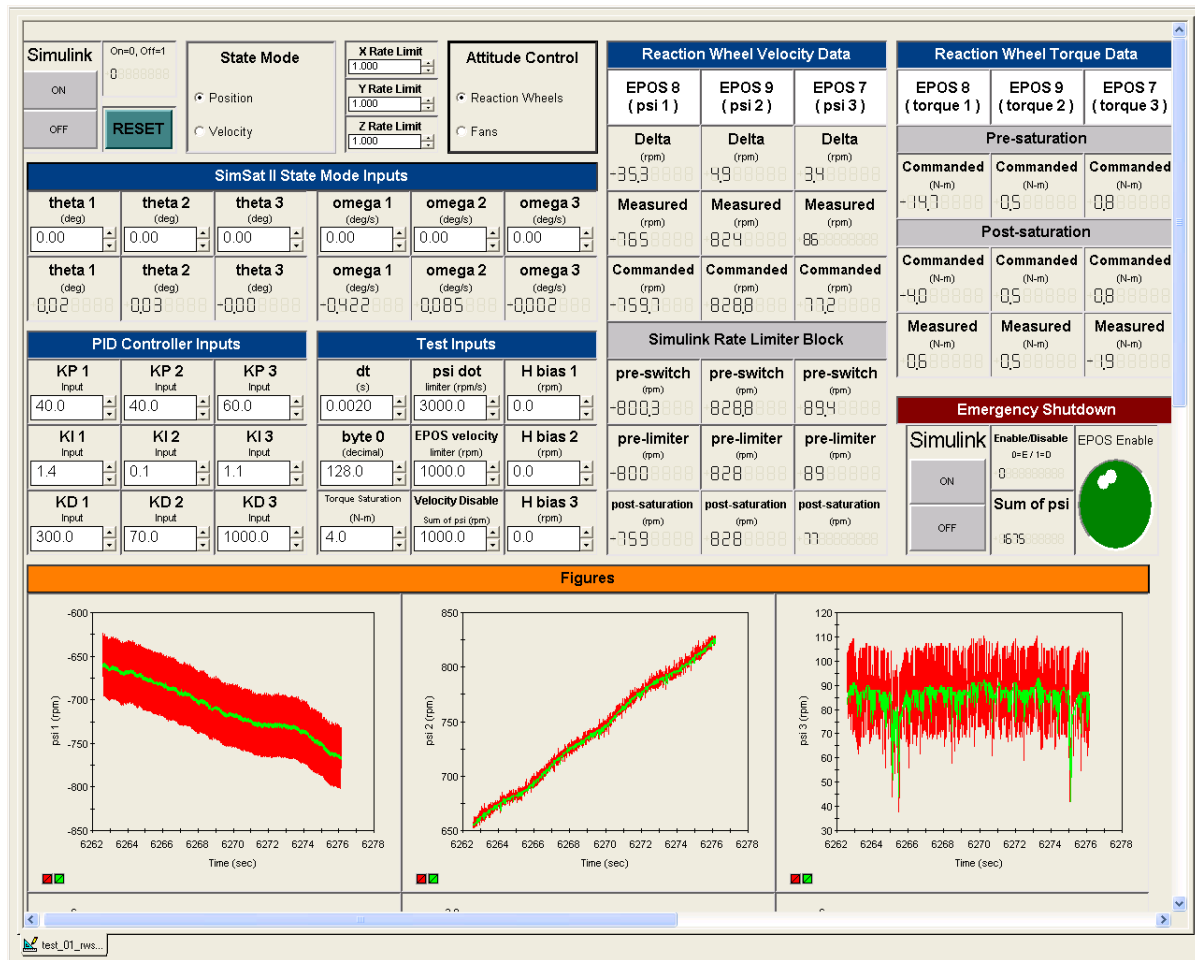


Figure 3.14: Example dSPACE ControlDesk Layout

3.3 System Interface

The hardware and software architecture of SimSat II includes both hardwired and wireless interfaces. Figure 3.15 illustrates the interfaces between the hardware and software components described in Sections 3.1 and 3.2. Hardwired interfaces are represented by solid lines whereas wireless interfaces are represented by dashed lines.

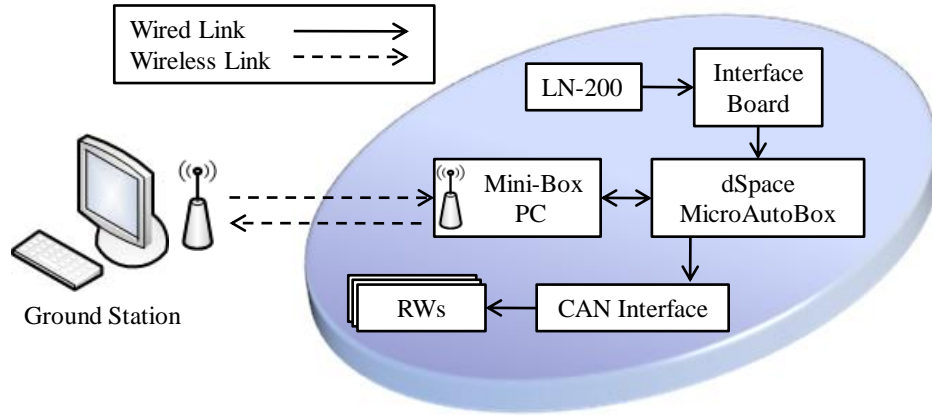


Figure 3.15: SimSat II Communications Diagram

3.4 System Characterization

Although previous research efforts had equipped SimSat II with a fan thruster ACS, integrating a reaction wheel ACS required an altogether separate focus. Modifications were made to hardware and software alike throughout the design, build, and test phases of this research. To fully understand the effects of these modifications it is essential to apply technical rigor to the system characterization of SimSat II. Aspects of SimSat II that require characterization include:

1. Reaction wheel sizing
2. Velocity controller tuning
3. System safety measures
4. Velocity commanded schema

5. COM location
6. MOI determination
7. PID controller tuning

3.4.1 Reaction Wheel Sizing . The change in angular rate of the reaction wheel $\Delta\psi_w$ over a predetermined amount of time Δt imparts a calculable torque upon the spacecraft. Prior to building the reaction wheel assembly, it was necessary to estimate how much torque is required to perform a $\pm 10^\circ$ rest-to-rest maneuver of SimSat II about the 1- or 2-axis and a $\pm 30^\circ$ rest-to-rest maneuver about the 3-axis—all within 10 s. This estimate would then influence the electric motor selection and reaction wheel sizing.

Future capabilities and integration with legacy components were also taken into consideration; for example, momentum dumping can be demonstrated by coupling the reaction wheel ACS with the fan thruster ACS implemented by McFarland [33]. Therefore, it was decided in advance that the electric motor and controller should come from the same manufacturer as SimSat II's legacy equipment, Maxon Motor.

The assumed principal MOI of SimSat II measured by McFarland are 3.8, 3.2, and 5.0 kg-m² about the 1-, 2-, and 3-axis, respectively [33]. After augmentation of the reaction wheel ACS, the principal MOI of SimSat II will be greater than what McFarland determined. Nonetheless, this is the starting point for the design process. To determine the necessary amount of torque needed to reorient SimSat II such that the predefined performance specifications are achieved, the background theory from Section 2.3 is used.

Equation (2.20), the formula for an applied moment, is restated below

$$\vec{M} = \mathbf{I}\vec{\alpha} \tag{3.1}$$

where torque \vec{M} and acceleration $\vec{\alpha}$ are vectors and the MOI \mathbf{I} is a matrix. Vector and matrix notation are dropped in favor of scalar representation since individual torques about single axes are being investigated.

Solving Equation (3.1) in terms of the scalar value α and substituting the result into Equation (2.16) one is able to algebraically manipulate the resulting equation into an expression for torque as seen in Equation (3.2).

$$M = \frac{2I}{(t - t_o)^2} [\beta - \beta_o - \omega_o (t - t_o)] \quad (3.2)$$

From McFarland's research $C > A > B$ is known to be true. By investigating the worst case maneuver about the 3-axis C , the reorientation specifications of the 1- and 2-axis are satisfied as well. Note that the reorientation is a rest-to-rest maneuver beginning at β_o , ω_o , and t_o equal to zero. To calculate the amount of torque that is necessary to perform a rest-to-rest maneuver, the desired angular displacement β and desired time t is halved since bang-bang control dictates that a minimum time maneuver is completed by accelerating from rest at a constant rate then decelerating to rest at a constant rate. Equation (3.2) is now expressed in terms of the 3-axis worst case scenario

$$M_3 = \frac{4\beta C}{t^2} . \quad (3.3)$$

To calculate the necessary torque M_3 of $\pm 0.062 \text{ N} \cdot \text{m}$, substitute the angular displacement requirement of $\pm 30^\circ$ occurring in 10 s or less with an assumed 3-axis MOI of $5.0 \text{ kg} \cdot \text{m}^2$ into Equation (3.3). As a result, the Maxon EC 45 was selected for SimSat II's electric motor [30]. The EC 45 possesses a continuous torque of $0.283 \text{ N} \cdot \text{m}$ —more than two times the torque necessary to reorient SimSat II per McFarland's measured principal MOI. Accordingly, so long as SimSat II's MOI does not more than quadruple in value, the EC 45 will provide enough torque input necessary to reorient the spacecraft.

Knowing the torque M_3 that must be generated by the electric motor, Equation (3.4) is used in conjunction with the principle of conservation of momentum to discern the necessary MOI $I_{zz,w}$ for the reaction wheel about its axis of rotation. Since assumed earlier that the POI terms of SimSat II equal zero, the same is assumed for the reaction wheels. Therefore, the MOI $I_{zz,w}$ is a principal MOI and henceforth, will be denoted as D_w . The torque generated by the reaction wheel can now be written as

$$M = M_w \quad (3.4a)$$

$$= I\alpha \quad (3.4b)$$

$$= D_w \dot{\psi}_w . \quad (3.4c)$$

The determination of D_w is an iterative process where D_w and the angular acceleration of the reaction wheel $\dot{\psi}_w$ are investigated simultaneously. Though there is no requirement for $\dot{\psi}_w$, too small of a value will require a reaction wheel with a very large MOI—possibly too large for installation upon SimSat II. Conversely, too large a value for $\dot{\psi}_w$ will require a reaction wheel with a very small MOI—possibly smaller than the motor shaft itself—an impossibility to implement. Somewhere in between a favorable value exists.

Simple disc-shaped reaction wheels were designed for SimSat II. The MOI D_w of these discs about their axis of rotation is denoted as

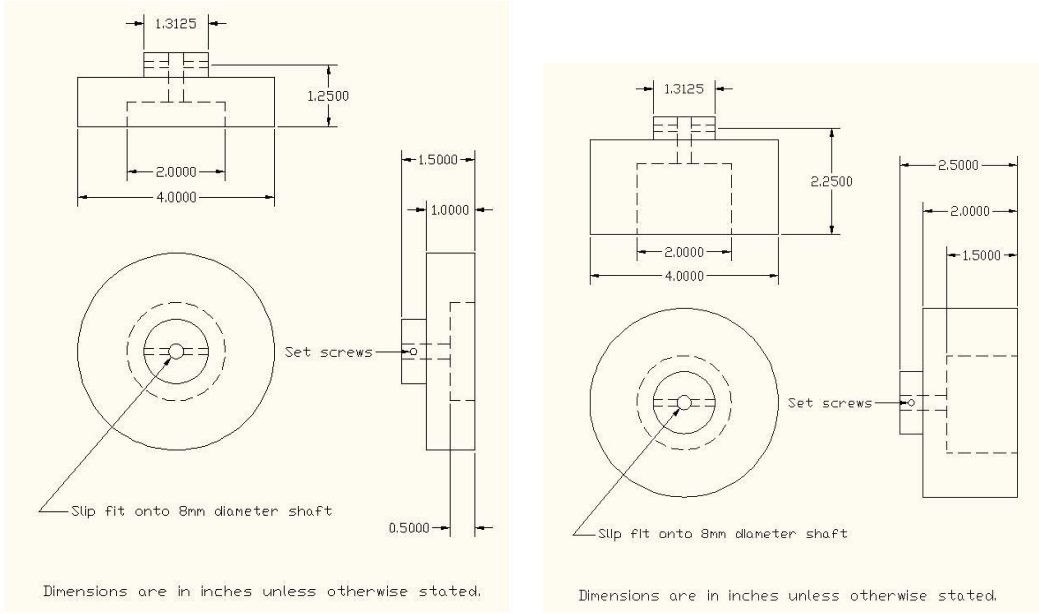
$$D_w = \frac{mr^2}{2} \quad (3.5)$$

where m is the mass and r is the radius of the reaction wheel, respectively. Recognizing that the mass of the reaction wheel can be expressed in terms of its mass density ρ and volume V by Equation (3.6)

$$m = \rho V \quad (3.6)$$

where the volume of a cylinder is

$$V = \pi r^2 h , \quad (3.7)$$



(a) Primary Reaction Wheel Design

(b) Precautionary Reaction Wheel Design

Figure 3.16: SimSat II Reaction Wheel Designs

Equation (3.5) can be rewritten as

$$D_w = \frac{\rho \pi r^4 h}{2} . \quad (3.8)$$

The reaction wheels were fabricated from 316 stainless steel because it resists oxidation, is readily attainable, and easily machined. The mass density ρ of 316 stainless steel is $8,000 \text{ kg/m}^3$. Knowing that a torque M_3 of $\pm 0.070 \text{ N} \cdot \text{m}$ must be provided, substituting Equation (3.8) into Equation (3.4) makes it possible to determine favorable reaction wheel dimensions for inclusion onto SimSat II's tabletop deck while avoiding unsuitable angular acceleration rates for the electric motor. The resultant reaction wheel has a diameter of 4 in and is 1 in thick. Its theoretical principal MOI D_w is $0.002092 \text{ kg} \cdot \text{m}^2$. A three-view drawing the 1 in thick primary reaction wheel is shown in Figure 3.16(a).

Comparing the principal MOI measured by McFarland, $C > A > B$. As an additional precaution, an optional reaction wheel was designed for 3-axis control such that it has an MOI of approximately two times that of the 1 in thick reaction wheel. If the previous exercise in sizing the reaction wheel falls short of expected, the reaction wheel with greater MOI is capable of providing increased torque. The precautionary

reaction wheel has a diameter of 4 in and is 2 in thick. Its theoretical principal MOI D_w is $0.004085 \text{ kg} \cdot \text{m}^2$. A three-view drawing of the 2 in thick precautionary reaction wheel is shown in Figure 3.16(b).

After designing, building, and testing the reaction wheel assembly aboard SimSat II it was decided that the 1 in thick reaction wheel would control the 1- and 2-axis whereas, the 2 in thick reaction wheel would command the 3-axis.

3.4.2 Velocity Controller Tuning . The closed-loop system consisting of the EPOS 70/10 velocity PI controller and electric motor are represented in block diagram notation in Figure 3.17. To tune the velocity controller one must navigate the EPOS User Interface previously discussed in Section 3.2.1. The manufacturer's instructions provided with the EPOS 70/10 guide the user through automatic and manual tuning of the EPOS 70/10 velocity controller [28]. The quickest and most convenient way to tune the velocity controller is by using the automatic tuning option. Unfortunately, after repeated attempts to automatically tune the controllers, the EPOS User Interface software was unable to determine satisfactory gain settings.

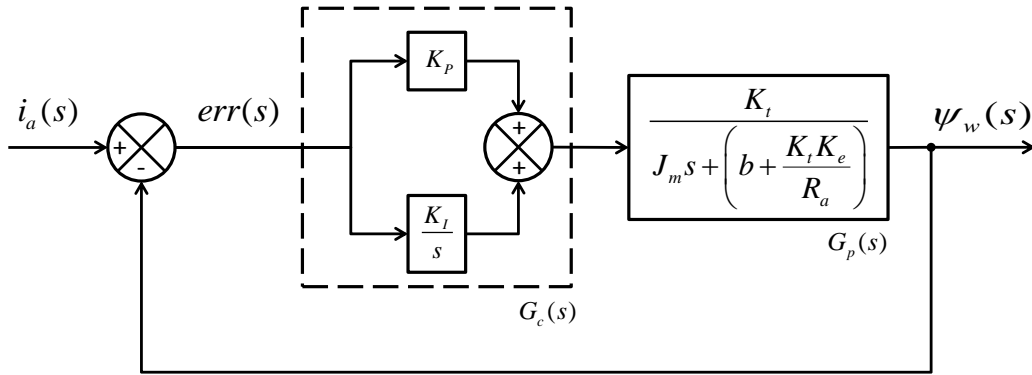


Figure 3.17: EPOS 70/10 Velocity Controller

Maxon Motor company advised that automatic tuning cannot be performed for the desired application of the EC 45 motor. The ratio of the MOI of the reaction wheel D_w to that of the armature of the electric motor $I_{armature}$ must be less than or equal to 10 for automatic tuning to be effective,

$$\frac{D_w}{I_{armature}} \leq 10 . \quad (3.9)$$

For the 1 in thick reaction wheel, the ratio represented in Equation (3.9) is calculated to be 100; for the 2 in thick reaction wheel the ratio is 194. In either case, the ratio is much too high for effective employment of the automatic tuning function. Manual tuning did not fair any better; even the order of magnitude for the proportional gain K_P and integral gain K_I could not be determined.

To help determine the magnitudes of K_P and K_I , the Ziegler-Nichols tuning method in which the automatic-reset gains are based on a decay ratio of approximately 25% was used [53]. Before using the Ziegler-Nichols tuning method however, one must first define the transfer function of the plant; in this case, the electric motor plus reaction wheel.

Prior to defining the transfer function for the plant, several assumptions were made:

- The armature is a rigid body
- The following factors are to be neglected [11]:
 - Coulomb friction and associated dead-band effects
 - Magnetic hysteresis
 - Magnetic saturation (in both stator and armature)
 - Eddy current effects
 - Nonlinear constitutive relations for magnetic induction
 - The effect of the rotor magnetic flux (armature flux) on the stator magnetic flux (field flux)

The transfer function of an electric motor $G_p(s)$ is expressed in the complex-frequency domain as its output angular velocity $\psi_w(s)$ divided by its input current $i_a(s)$. As a result of the aforementioned assumptions, the transfer function of the plant is of the form

$$G_p(s) = \frac{\psi_w(s)}{i_a(s)} = \frac{K_t}{J_m s + \left(b + \frac{K_t K_e}{R_a}\right)} . \quad (3.10)$$

The variables K_t , J_m , b , K_e , and R_a can be located using sources [30, 29] and by contacting Maxon Motor directly [35]; they are defined as follows:

K_t	torque constant of electric motor
J_m	MOI of reaction wheel, armature, and encoder about the axis of rotation
b	viscous damping of armature
K_e	electromotive force (emf) constant
R_a	armature resistance

The open-loop transfer function of the electric motor with reaction wheel can be represented in block diagram notation as seen in Figure 3.18 where $i_a(s)$ is the electric current input and $\psi_w(s)$ is the angular rotation output. Exciting the open loop transfer function with a unit step input and analyzing the reaction curve with the method developed by Ziegler and Nichols, the resultant values of K_P and K_I for the EPOS 70/10 velocity controller were determined to be unsatisfactory as well [53, 16, 39].

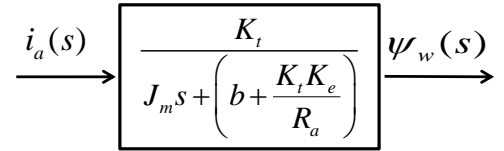


Figure 3.18: Electric Motor Open-Loop Transfer Function

Maxon Motor company advised that the applied load to the EC 45 is greater than normally intended. For this particular application the miscellaneous object identifier, accessed using the EPOS User Interface under the object dictionary tab, must be changed from its default value of 0 and set to a value of 8 instead [36]. Additional manual tuning yielded a proportional gain K_P of 15,000 and an integral gain K_I of 10. These

gains behaved nicely producing satisfactory overshoot and settling time; they remained unchanged throughout the remainder of this research.

3.4.3 System Safety Measures . Throughout test and performance evaluation of a system, safety measures are important to prevent personal injury and equipment failure. Although system safety measures had been previously implemented by McFarland and proved effective in avoiding injury, these measures did not prevent component damage while testing the reaction wheel ACS. Sections 3.4.3.1 – 3.4.3.4 discuss safety measures integrated into the SimSat II SIMULINK model.

3.4.3.1 Angular Velocity Constraints . The first step in defining a safe operating range of the Maxon EC 45 motor is to first determine its maximum commanded angular velocity. This can be determined from the following relation

$$\psi_{w_{max}} = (Applied\ Voltage)_{max} * Motor\ Speed\ Constant \quad . \quad (3.11)$$

SimSat II uses a 36 V battery power supply. The applied voltage from the EPOS 70/10 controller is 90% of the value from the power supply, and the motor speed constant of the EC 45 motor is 306 rpm/V [31, 30]. Consequently, the calculated maximum angular velocity of the EC 45 is 9,914 rpm. Within SimSat II's SIMULINK model, the angular rate limit imposed upon the EC 45 motor is $\pm 9,000$ rpm; 10% less than its maximum rate.

3.4.3.2 Angular Acceleration Constraints . The EPOS 70/10 controller has a continuous output current of 10 A and a maximum output current of 25 A [31]. Solving Equation (3.10) in terms of armature current $i_a(s)$ it is seen that

$$i_a(s) = \left[\frac{J_m}{K_t} \psi_w(s) \right] s + \left(\frac{b}{K_t} + \frac{K_e}{R_a} \right) \psi_w(s) \quad . \quad (3.12)$$

Transforming Equation (3.12) from the complex-frequency domain to the time domain, Equation (3.13) provides intuition toward the system. For instance, one readily sees which variables are not constant: the angular velocity of the electric motor ψ_w ,

viscous damping b , and the time rate of change of the electric motor's angular velocity $\dot{\psi}_w$. Equation (3.13) clearly demonstrates that the electric motor is capable of demanding more current than the 25 A limit of the EPOS 70/10 can withstand.

$$i_a(t) = \frac{J_m}{K_t} \dot{\psi}_w(t) + \left(\frac{b}{K_t} + \frac{K_e}{R_a} \right) \psi_w(t) \quad (3.13)$$

Angular velocity ψ_w has been limited to $\pm 9,000$ rpm. Equation (3.13) shows that the remaining non-constant variables are b and $\dot{\psi}_w$. Since viscous damping is inherent to the system, the only other variable that can be limited to avoid controller damage is the reaction wheel's angular acceleration $\dot{\psi}_w$.

Equation (3.13) expressed in an alternate manner is

$$i_a = \left[\frac{J_m}{K_t} \dot{\psi}_w \right] + \left[\left(\frac{b}{K_t} + \frac{K_e}{R_a} \right) \psi_w \right] \quad (3.14a)$$

$$= [LS] + [RS] \quad (3.14b)$$

where LS is the left side of the addition sign and RS the right. Maxon Motor company affirmed that the viscous damping b of the electric motor is $2.5 \text{ mN} \cdot \text{m}/1000 \text{ rpm}$ but the value has a large uncertainty of approximately 50% [35]. The J_m term communicates that LS is a greater contributor than RS toward the input current i_a of the system. Focusing attention on LS , Equation (3.15) was used to perform a back-of-the-envelope calculation to estimate an appropriate constraint value of $\dot{\psi}_w$

$$\dot{\psi}_w \leq \frac{i_a K_t}{J_m} . \quad (3.15)$$

The resultant value of $\dot{\psi}_w$ was determined to be $1,823 \text{ rpm/s}$ —much lower than the $10,000 \text{ rpm/s}$ default value of the EPOS 70/10 controller. Within SimSat II's SIMULINK model, the angular acceleration limit imposed upon the EC 45 motor is $\pm 1,500 \text{ rpm/s}$; $\approx 20\%$ less than the back of the envelope calculation.

3.4.3.3 Torque Constraints . The amount of torque generated by the reaction wheel ACS is a function of $\dot{\psi}_w$ as previously seen in Equation (3.4). Although a constraint of $\pm 1,500$ rpm/s was imposed upon $\dot{\psi}_w$, a redundant constraint is also imposed upon M_w in SimSat II's SIMULINK model.

Knowing $\dot{\psi}_w$ to be limited to $\pm 1,500$ rpm/s, the maximum torque $M_{w_{max}}$ about the 1- and 2-axis is calculated to be $0.3395 \text{ N} \cdot \text{m}$ and about the 3-axis it is $0.6590 \text{ N} \cdot \text{m}$. An upper and lower constraint value of $\pm 1 \text{ N} \cdot \text{m}$ was therefore inserted into SimSat II's SIMULINK model to limit the demanded torque from the EPOS 70/10 controller.

3.4.3.4 System Shutdown . The emergency shutdown logic in SimSat II's SIMULINK model was overhauled after hardware failure occurred due to excess current. Although an acceleration rate constraint of $\pm 1,500$ rpm/s had been imposed upon $\dot{\psi}_w$, it was discovered that this constraint is overridden when a shutdown command is sent to the EPOS 70/10 controllers. In fact, the SIMULINK software interrupt block (see Figure 3.19) overrides all other logic in the model when performing its duty. As a result, upon issuance of the shutdown command, the EC 45 motors decelerated at the Maxon Motor default rate of $10,000$ rpm/s resulting in component failure because more current was demanded than the 25 A limit of the EPOS 70/10 could withstand.

In the original SimSat II SIMULINK model developed by McFarland, system shutdown via software interrupt was not a problem due to the low MOI of the fan blades. For this research, an intermediate step was designed. After the software interrupt occurred, ψ_w would decelerate at a value of $\dot{\psi}_w$ equaling $1,500$ rpm/s. When Equation (3.16) is satisfied,

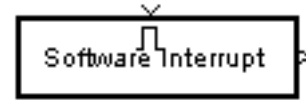


Figure 3.19: SIMULINK Software Interrupt Block

$$|\psi_{w1}| + |\psi_{w2}| + |\psi_{w3}| \leq 1,000 \text{ rpm} , \quad (3.16)$$

system shutdown is executed. Thereafter, no additional EPOS 70/10 controllers suffered from excessive current damage.

3.4.4 *Velocity Commanded Schema* . The basic premise of attitude control using reaction wheels requires an instantaneous change in the angular rates of the reaction wheels $\Delta\psi_w$ so that a resultant torque M can be imparted upon the spacecraft. In the case of SimSat II, the change in angular rate is through the EPOS 70/10 controller via the SIMULINK PID controller.

3.4.4.1 *RTI CAN Blockset* . To issue commands to the EPOS 70/10 controller, SimSat II is equipped with the dSPACE real-time interface (RTI) CAN SIMULINK blockset [14]. The RTI CAN block is capable of transmitting up to 8 bytes (64 bits) of information per message. The modern de facto standard of the number of bits per byte is 8; however, byte size can be hardware specific. The byte size of the EPOS 70/10 controller is hardware specific; allowing as many as 64 bits per byte or as few as 1 bit per byte.

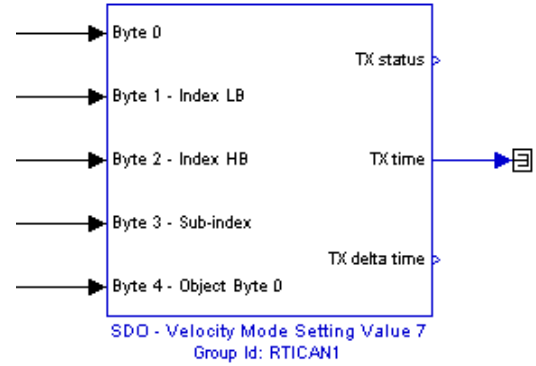


Figure 3.20: dSPACE RTI CAN Block

Figure 3.20 illustrates an RTI CAN block transmitting a 5-byte velocity command. It appears as if a command consisting of 5 bytes of data (40 bits) is being transmitted, when in fact it is 64 bits of data. With the RTI CAN blockset the user has the option of designating the start and end bit of each byte.

The typical byte structure of the EPOS 70/10 controller is as follows: byte 0 identifies the object (bytes 4–7) length in number of bits, bytes 1 and 2 are the index low byte and index high byte, respectively, byte 3 is the sub-index, and Bytes 4–7 are reserved for the commanded value [27].

One item to note is that the Maxon Motor bit sequence is transposed. Whereas binary numbers are usually expressed as

$$\underbrace{00000010}_{\text{High Byte}} \underbrace{00000110}_{\text{Low Byte}} = 518 ,$$

Maxon Motor expresses binary numbers as

$$\underbrace{00000110}_{\text{Low Byte}} \underbrace{00000010}_{\text{High Byte}} = 518 .$$

A second item to note is that all documented Maxon Motor command values are provided in hexadecimal format with 0x preceding the hexadecimal value. To send a command with the RTI CAN blockset, the hexadecimal codes must be converted to an unsigned integer. If the user wants to send a negative value (e.g., reverse the angular velocity of a reaction wheel), two's complement must be performed [50].

$$\begin{aligned} & \underbrace{11111010}_{\text{Low Byte}} \underbrace{00000000}_{\text{High Byte}} = +250 \text{ rpm} \\ & \Downarrow \quad \text{one's complement} \\ & \underbrace{00000101}_{\text{Low Byte}} \underbrace{11111111}_{\text{High Byte}} \\ & \Downarrow \quad \text{two's complement} \\ & + \underbrace{00000001}_{\text{Low Byte}} \\ & \underbrace{00000110}_{\text{Low Byte}} \underbrace{11111111}_{\text{High Byte}} = -250 \text{ rpm} \end{aligned}$$

3.4.4.2 Inundated EPOS . For PID control of SimSat II to be effective it is imperative that the EPOS 70/10 accurately measure the angular velocity of the reaction wheel ACS. Otherwise, erratic control inputs occur. To determine the validity of the measured angular rates, a sample set of data was collected. This sample set of data is represented in Figure 3.21(a). As can be seen, the controller suffered many inaccuracies. Periodically, the measured velocity value would equal zero. After much thought, a conjecture was formulated: the zero return rate is most likely due to the

confluence of the measurement and velocity commands. The EPOS 70/10 must decide which of the simultaneous commands it receives to accept. When it accepts the velocity command, the measurement command is returned an error value of zero.

To circumvent the numerous zero measurements, a rate limiter was imposed on the EPOS 70/10 velocity measurements. The SimSat II SIMULINK model was commanded to run the simulation at a fixed time step Δt of 1 ms; based on this, a rate limit of $\pm 1,000$ rpm per millisecond was selected. If the rate of change of the measurement exceeded this rate limit, the measurement would be clipped. Figure 3.21(b) displays the rate limited velocity measurements. Note how zero values are accepted at lower angular velocities. This is due to the zero value falling within the rate limiter, but at higher angular velocities the measurement is clipped at the $\pm 1,000$ rpm per millisecond limit.

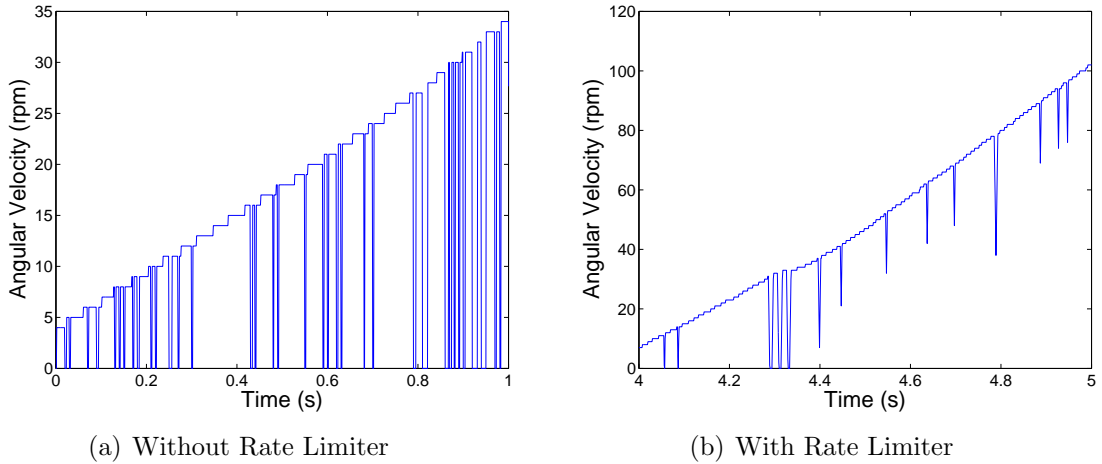


Figure 3.21: EPOS 70/10 Angular Velocity Measurements

After implementing the EPOS 70/10 velocity measurement rate limiter, a known torque of $0.090 \text{ N} \cdot \text{m}$ was applied to the perimeter of SimSat II about the 1-axis. It was expected that the reaction wheel ACS could overcome this disturbance torque and maintain SimSat II's current attitude. It was also expected that if a torque of $0.090 \text{ N} \cdot \text{m}$ was commanded of the reaction wheel situated parallel to the 1-axis, the angular velocity measurement would be similar in smoothness to that of Figure 3.21(b).

Instead, Figure 3.22(a) shows that SimSat II was not able to maintain its current attitude. The peaks in this figure are a result of SimSat II's constrained motion about the 1-axis (the satellite simulator collided with the air-bearing pedestal). The

angular velocities attained by ψ_3 in Figure 3.22(b) never exceed $\pm 1,000$ rpm therefore, the rate limiter never prevents an erroneous zero reading. But more importantly, the commanded torque exceeds $0.090 \text{ N} \cdot \text{m}$, bouncing back and forth between an arbitrarily defined torque constraint of $\pm 2 \text{ N} \cdot \text{m}$ as seen in Figure 3.22(c). The reaction wheel ACS did not command the amount of torque measured otherwise, SimSat II would have been capable of maintaining its attitude.

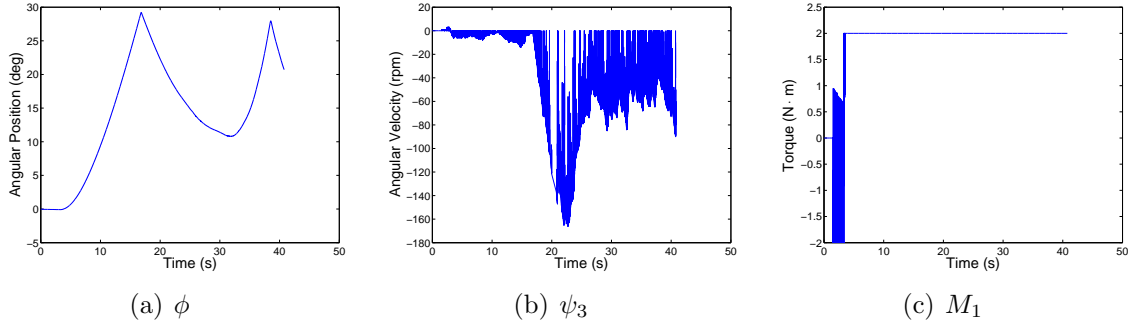


Figure 3.22: Disturbance Torque of $0.090 \text{ N} \cdot \text{m}$ Applied about X-Axis

Retreating to the principle of conservation of momentum and investigating Equation (3.4) more rigorously, one concludes that the only variable that is not constant is $\dot{\psi}_w$. In Section 3.4.3.2, $\dot{\psi}_w$ was fixed at $\pm 1,500 \text{ rpm/s}$, and in Section 3.4.4.5 $\dot{\psi}_w$ is discretized as

$$\dot{\psi}_w = \frac{\Delta\psi_w}{\Delta t} . \quad (3.17)$$

Since $\Delta\psi_w$ can be experimentally measured, it is evident that Δt requires characterization effort. After further contemplation, an alternate approach to eliminating the zero read-outs was developed: deconflict the commands sent to each EPOS controller by developing an alternating command sequence.

3.4.4.3 Two-to-One Multiplexer . Figure 3.23 illustrates the SIMULINK two-to-one multiplexer developed which switches back and forth between the velocity and measurement command inputs. The switch is toggled by a pulse generator that continuously sends a square wave of amplitude equal to one, a period of 2 ms, and pulse width that is 50% of the period. As a result, the intended controller never receives

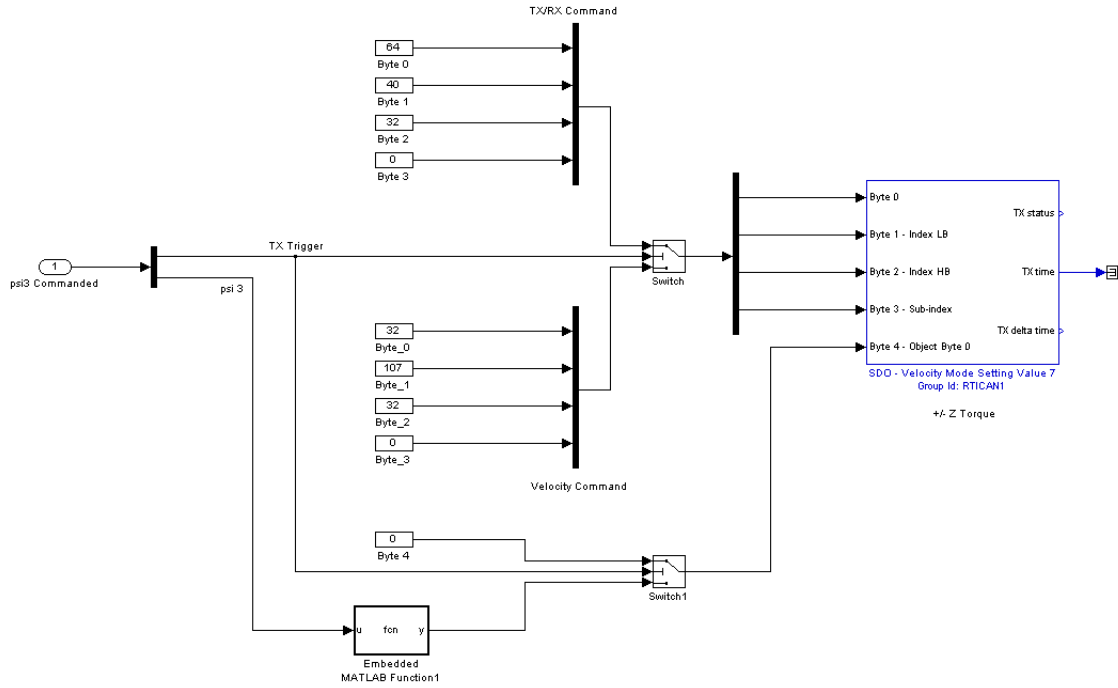


Figure 3.23: RTI CAN Two-to-One Multiplexer

more than one command at a time. Otherwise, as seen in Section 3.4.4.2 the controller experiences conflicting commands and responds unpredictably.

Again, a known torque was input, and as before in Section 3.4.4.2 the reaction wheel ACS did not command the amount of torque measured. The two-to-one multiplexer failed to characterize Δt as intended. After further pondering the dilemma of Δt , another supposition was formulated: not only must command inputs be deconflicted per EPOS controller, but they must also be deconflicted on the CAN bus. No more than one command can traverse the CAN bus at any given time. Therefore, an alternate approach to characterizing Δt must be entertained.

3.4.4.4 Time-Division Multiplexing . To ensure no more than one command exists on the CAN bus at a time, time-division multiplexing (TDM) was implemented. Using TDM, Δt can be fixed at a known quantity. Since the SimSat II SIMULINK model runs at a simulation time step of 1 ms, Δt cannot be smaller than 1 ms. After careful deliberation, Δt was fixed at a known period of 100 ms. Figure 3.24 displays the master time scheduler for the reaction wheel ACS.

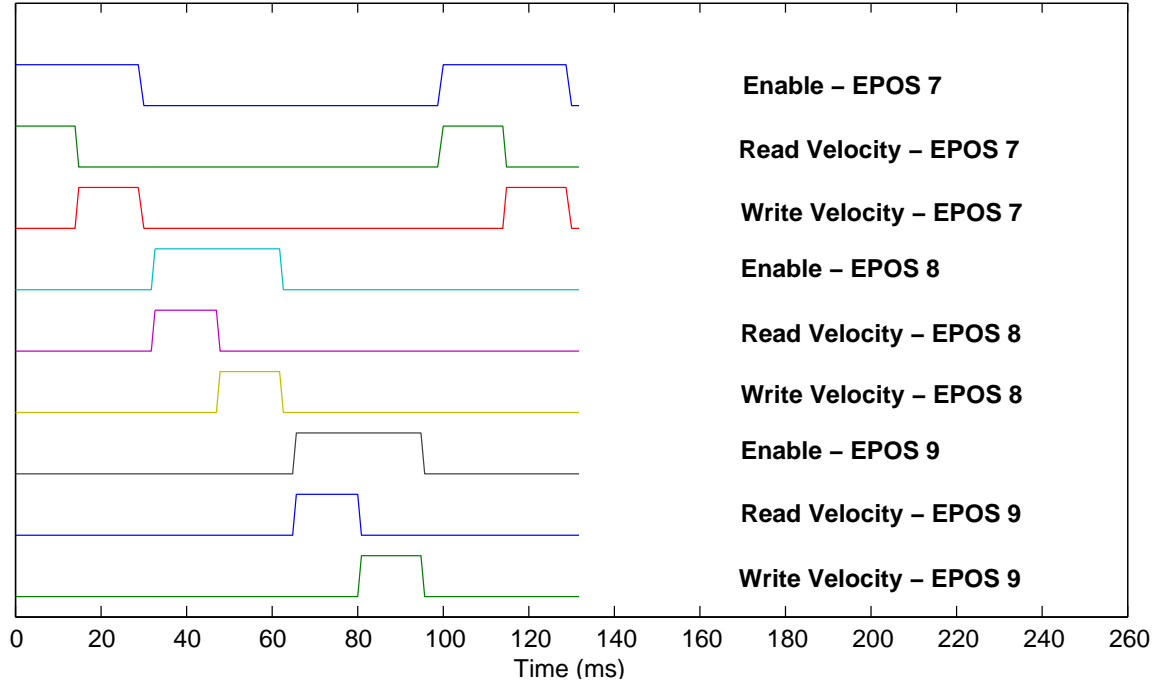


Figure 3.24: CAN Bus Time-Division Multiplexing

EPOS 7, 8 and 9 are node identifiers as mentioned in Section 3.2.1. EPOS 7 commands the 3-axis reaction wheel, EPOS 8 the 1-axis, and EPOS 9 the 2-axis. The TDM schedule begins with EPOS 7 being enabled for 30 ms. During this 30 ms window, the only EPOS controller that can be communicated with is EPOS 7. The 30 ms window for the EPOS 7 is then subdivided into two 15 ms windows. During the first 15 ms only read angular velocity commands can be transmitted, and during the second 15 ms only write angular velocity commands can be transmitted.

The EPOS controllers operate in the SIMULINK RTI environment such that they require an RTI transmit (TX) CAN block and an RTI receive (RX) CAN block. The TX block is an active block that communicates across the CAN bus. For this research, the TX block is used to send read angular velocity commands and write angular velocity commands. The RX block is a passive block that is continuously on stand-by and does not communicate across the CAN bus. Upon the TX block issuing the angular velocity measurement command, the RX block receives the measured value.

In an effort to fix Δt as best as possible, the read angular velocity commands and write angular velocity commands were then issued impulsively. Half way through the 15 ms read angular velocity window, for 1 ms, the read angular velocity command is issued. Likewise, half way through the 15 ms write angular velocity window, for 1 ms, the write angular velocity command is issued. These commands are then issued again 100 ms (Δt) later.

Like the EPOS 7, EPOS 8 and 9 are each enabled for 30 ms with 15 ms read and write windows. There is a 3 ms time gap between the EPOS 7 and 8 enable windows, 3 ms time gap between the EPOS 8 and 9 enable windows, and a 4 ms time gap between the EPOS 9 and 7 enable windows. The EPOS 8 and 9 read angular velocity commands and write angular velocity commands are also impulsively issued. Figure 3.25 shows the TDM designed in SIMULINK.

3.4.4.5 Angular Momentum Discretized . Absolute angular velocity of the reaction wheels does not have an effect on satellite position; it is the change in the reaction wheels' angular velocity that has an effect. Discretizing Equation (3.4) shows that a reaction wheel ACS can impart pure rotation about the principal axes of SimSat II by the relation

$$M_w = D_w \dot{\psi}_w \quad (3.18a)$$

$$= D_w \frac{\Delta \psi_w}{\Delta t} . \quad (3.18b)$$

Solving Equation (3.18) for $\Delta \psi_w$ demonstrates

$$\Delta \psi_w = \frac{M_w}{D_w} \Delta t . \quad (3.19)$$

As the PID controller computes the necessary control torques M_c in Equation (2.46) to overcome SimSat II's positional error, a resultant $\Delta\psi_w$ must be commanded. Performing algebra manipulation on Equation (3.18), one is able to develop the following expression for calculating $\Delta\psi_w$,

$$\Delta\psi_w = \dot{\psi}_w \Delta t . \quad (3.20)$$

The reaction wheel angular acceleration is limited to $\pm 1,500$ rpm/s in Section 3.4.3.2. The fixed time step of Δt is 100 ms is stated in Section 3.4.4.4. Therefore, the maximum $\Delta\psi_w$ the reaction wheel ACS is capable of performing is 150 rpm.

To command $\Delta\psi_w$, the EPOS 70/10 controller is first commanded to measure the present angular velocity of the reaction wheel. Then it is commanded to send a velocity value that is $\Delta\psi_w$ greater than the measured value

$$\psi_{w_{commanded}} = \psi_{w_{measured}} + \Delta\psi_w \quad (3.21a)$$

$$= \psi_{w_{measured}} + \frac{M_w}{D_w} \Delta t . \quad (3.21b)$$

3.4.5 Center of Mass . The COM of an object is the single point where the static balance moments about three mutually perpendicular axes are all zero [5]. To accurately simulate a torque-free environment, the COM of SimSat II must coincide with its COR. Otherwise, unwanted gravitational torques will persist. The COM of SimSat II can be manipulated by properly placing counterweights until all gravitational torques are eliminated. The COR of SimSat II is defined as the center point of the Space Electronics, Inc. tri-axis spherical air-bearing.

Figure 3.26 illustrates the gravitational torque effects due to the COM and COR not being coincident. If the COM has a positive height h , the hardware configuration demonstrates the behavior of an inverted pendulum; when the COM is not vertically aligned with the COR, the system is unstable. If the COM has a negative h , the hardware configuration demonstrates the behavior of a pendulum; when a disturbance input

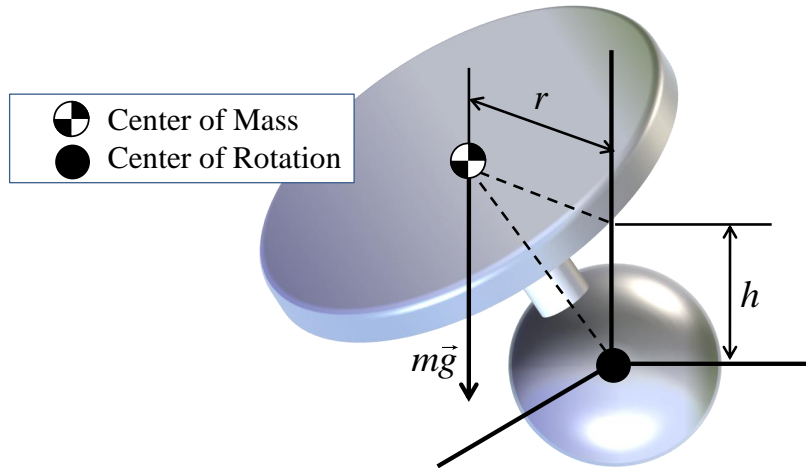


Figure 3.26: Non-Coinciding COM and COR

is experienced, the system oscillates eventually returning to a stable configuration. Likewise, if the COM is a distance r away from the COR, the COM is the disturbance input causing the system to oscillate until eventually returning to a stable configuration.

The method used in this research to manipulate the location of SimSat II's COM involved counterbalancing. Ballast was added to SimSat II with the intent of establishing a coincident COM and COR. Boynton cautions however, that ballast be added at a height that is as close as possible to the height of the COM of the spacecraft. Otherwise the addition of this weight will produce a large POI unbalance [5].

3.4.5.1 Reaction Wheel Placement . The addition of the reaction wheels added mass to SimSat II; 2.745 kg for the 2 in thick reaction wheel and 1.520 kg a piece for the two 1 in thick reaction wheels. Placement of the reaction wheel assemblies was important in maintaining the assumption that the POI of SimSat II is equal to zero.

The horizontal location of the reaction wheel assembly COM must lie upon an axis of rotation. First, the reaction wheel assembly bracket baseplate was placed on top of SimSat II's tabletop deck 1 in x 1 in hole pattern. A pencil mark was made on the baseplate indicating the location of the axis of rotation. The reaction wheel and motor were then clamped into the motor mount. A cylinder was placed under the baseplate of the reaction wheel assembly. The assembly was then rolled laterally atop the cylinder until the equilibrium point was discovered. The motor mount was loosened and

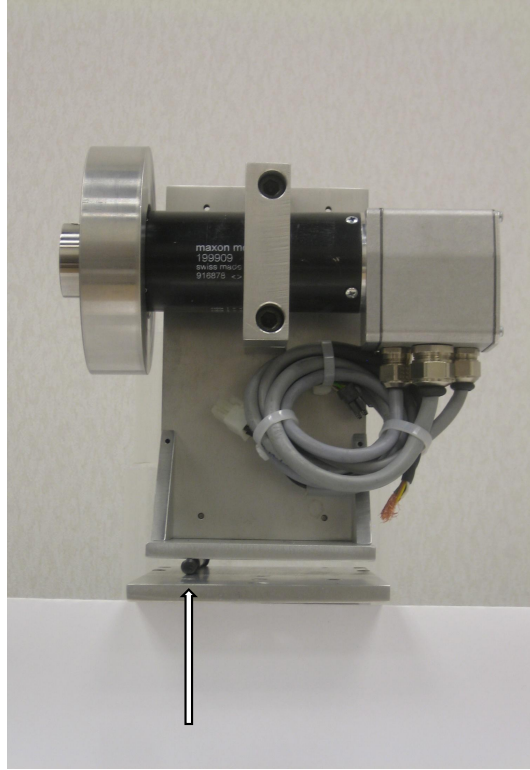


Figure 3.27: Horizontal COM Location of Reaction Wheel Assembly

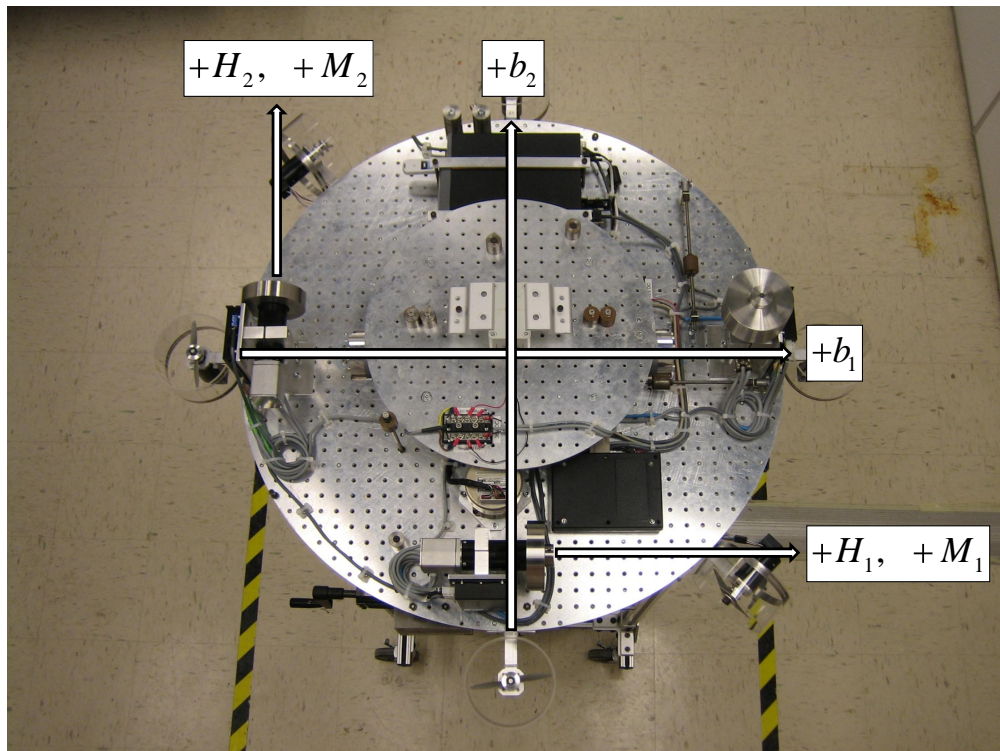


Figure 3.28: Principal Axes of SimSat II

the motor slid back and forth until the equilibrium point matched the axis of rotation pencil marking on the bracket base plate. Figure 3.27 shows the experimental horizontal location of the reaction wheel assembly COM. Figure 3.28 illustrates the location of SimSat II's principal axes of rotation and the final configuration of the reaction wheel assemblies atop SimSat II's tabletop deck.

3.4.6 Mass Moment of Inertia . A body's mass moment of inertia is a measurement of its resistance to rotation. Figure 2.7 shows that a body's resistance to rotation is a result of the body's mass distribution. To measure MOI and POI, a spacecraft is attached to a spin table as seen in Figure 3.29.



Figure 3.29: Measuring MOI of Spacecraft [4]

A known, constant torque is then applied to the platform. The known torque divided by the time rate of change of the spacecraft's angular velocity determines the MOI of the spacecraft about that particular axis of rotation. If one takes the spin table and equips it underneath with a vertically mounted shaft with bearings, then the spacecraft's POI can be measured. As the spacecraft rotates, centrifugal forces act

through the mass distributed far from the axis of rotation causing a sinusoidal force to be exerted against the bearings of the vertically mounted shaft [5].

A spin table was not used to measure the MOI of SimSat II. Rather, a known torque was applied to SimSat II using a hanging mass m while the spacecraft sat atop the tri-axial air-bearing pedestal. The governing equations needed to determine the MOI of SimSat II include

$$\vec{M} = \vec{F} \times \vec{l} \quad (3.22)$$

where \vec{l} is the distance vector from the COR to the applied force \vec{F} ,

$$\vec{F} = \vec{T} - \text{tension in string} . \quad (3.23)$$

The tension in the string however, is negligible therefore, \vec{F} can be written as

$$\vec{F} = \vec{T} = m\vec{g} . \quad (3.24)$$

Also needed among the governing equations is

$$\vec{M} = \mathbf{I}\vec{\alpha} . \quad (3.25)$$

Equating Equations (3.22) and (3.25) one finds that an entry to the MOI matrix \mathbf{I} can be expressed as

$$I_{ii} = \frac{mgl}{\alpha} . \quad (3.26)$$

The MOI about a principal axis of SimSat II is calculated using Equation (3.26). Figure 3.30 illustrates the test set-up.

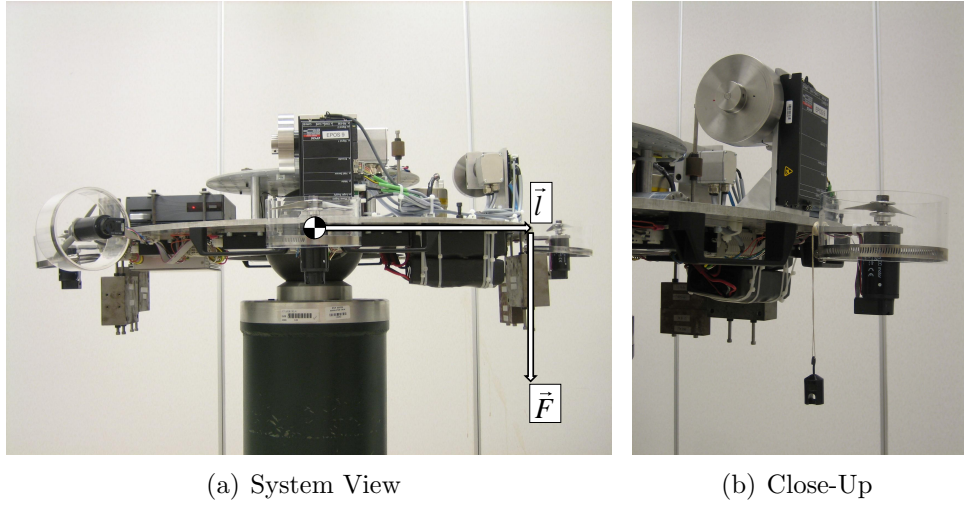
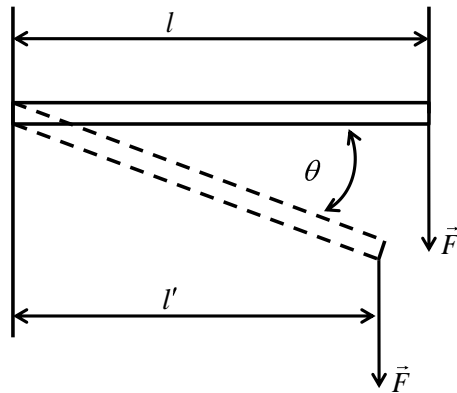


Figure 3.30: Hanging Mass MOI Measurement for Spacecraft Body

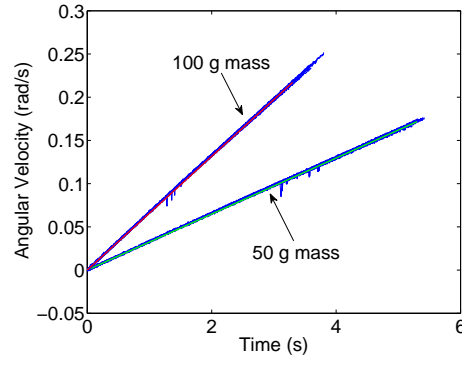
SimSat II's roll and pitch rotation must be kept within $\pm 15^\circ$ of the inertial axes. Imposing this limitation assures SimSat II receives at least 95% of the known torque due to cosine corrections. The cosine correction can clearly be seen in Figure 3.31 as the difference between l and l' .

The hanging mass test was performed approximately 10 times for each of SimSat II's principal axes. A second mass was then used to demonstrate repeatability of the experiment. Angular velocity measurements were collected and a least squares fit line

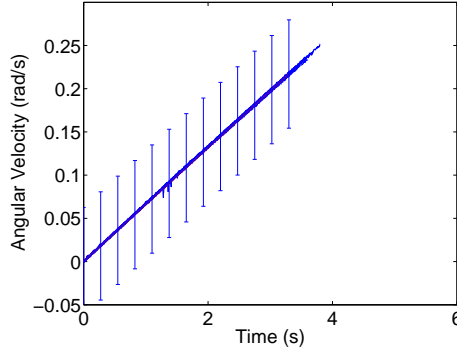


$$l' = l \cos \theta$$

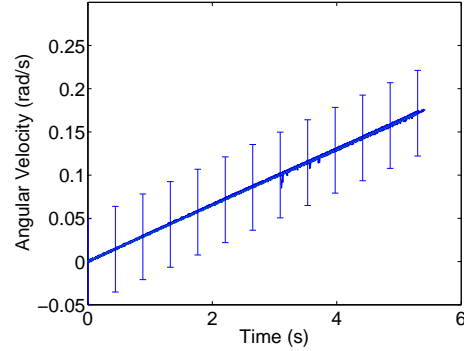
Figure 3.31: Error in Disturbance Torque Due to Cosine Losses



(a) Hanging Mass Resultant Data



(b) 100 g Mass Data with One σ



(c) 50 g Mass Data with One σ

Figure 3.32: SimSat II MOI Measurement— I_{xx}

was applied to the two sets of collected data (see Figure 3.32). The slope of these lines determines the value for α and by substituting α into Equation (3.26) one is able to solve for the MOI. The measured MOI values for SimSat II are presented in Table 3.4 and are used in all calculations performed in the test and evaluation phases of this research.

AFIT is not equipped with the necessary hardware to measure SimSat II's POI. Although it is assumed that the POI is equal zero, during the evaluation phase of this research SimSat II exhibited behavior that would indicate otherwise. Additional research in how to measure POI of the spacecraft simulator would greatly improve the performance characteristics of SimSat II.

Table 3.4: SimSAT II Measured MOI Values

Axis	Value
1	6.8 $\text{kg} \cdot \text{m}^2$
2	4.5 $\text{kg} \cdot \text{m}^2$
3	10.1 $\text{kg} \cdot \text{m}^2$

The principal MOI values about the reaction wheels' axis of rotation was measured using a much smaller spin table than that depicted in Figure 3.29. The measured principal MOI for SimSat II's reaction wheels are presented in Table 3.5 and are used in all calculations performed in the test and evaluation phases of this research.

Table 3.5: SimSAT II's Reaction Wheel Measured MOI Values

Axis	Value
1	0.002161 $\text{kg} \cdot \text{m}^2$
2	0.002161 $\text{kg} \cdot \text{m}^2$
3	0.004195 $\text{kg} \cdot \text{m}^2$

3.4.7 Inertial Measurement Bias .

The Northrop Grumman LN-200 IMU is used to collect SimSat II's angular acceleration measurements. These measurements are integrated twice; once by the LN-200 interface board to attain angular velocity, and a second time within SimSat II's SIMULINK model to determine the spacecraft's angular position (attitude). During the test phase of this research, it was noticed that the dSPACE ControlDesk layout would display a change in SimSat II's angular position even though the spacecraft sat motionless atop its test stand as seen in Figure 3.34. If the measurements of the LN-200 contained an inherent bias, integrating the re-

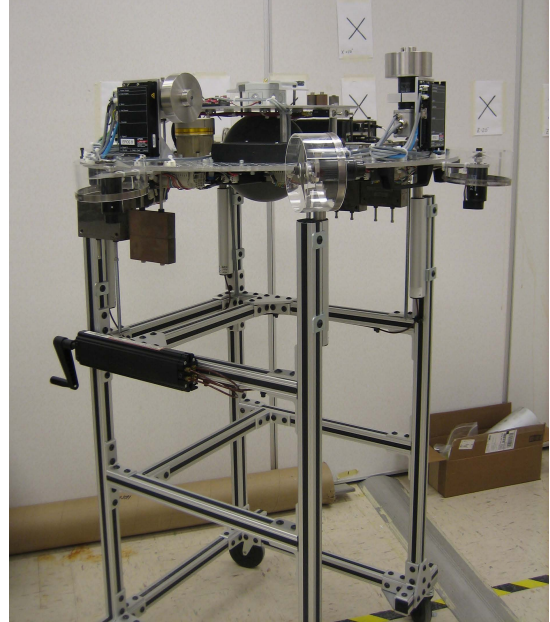


Figure 3.34: SimSat II on Test Stand

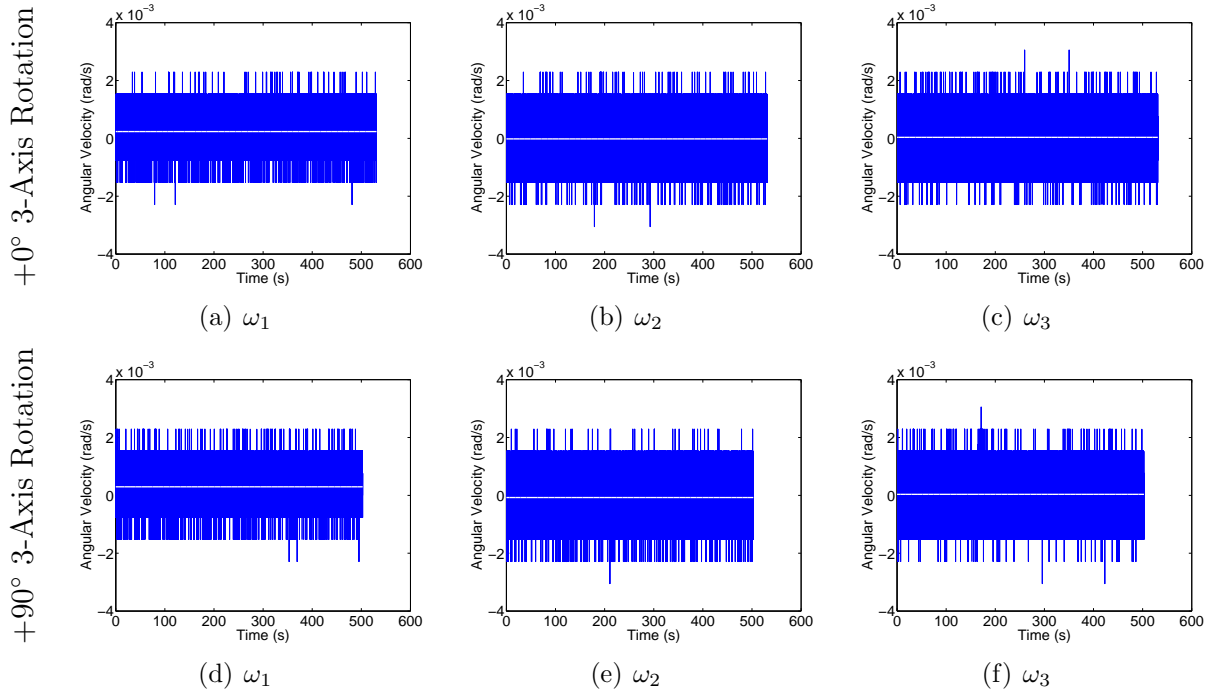


Figure 3.33: LN 200 Bias Measurements

sultant acceleration measurement twice over time would indeed cause a change in the angular position readout. As a test, angular velocity measurements from the LN-200 were recorded for approximately 10 minutes while SimSat II sat motionless. To discount possible non-zero measurements due to Earth's rotation rate, SimSat II was rotated 90° and again 10 minutes of angular velocity measurements were recorded. The comparison results can be seen in Figure 3.33.

The horizontal white lines represent the average values of the collected data. If the errant IMU measurements had been caused by the rotation of the Earth, Figures 3.33(a) and 3.33(e) would have equivalent data; as would Figures 3.33(b) and 3.33(d). This however, is not the case. Thus, it is concluded that a bias is present. The measured LN-200 bias values are presented in Table 3.6.

Table 3.6: LN-200 Bias Measurements

Axis	Value			
1	20.65×10^{-5}	rad/s	11.83×10^{-3}	deg/s
2	-4.75×10^{-5}	rad/s	-2.72×10^{-3}	deg/s
3	3.51×10^{-5}	rad/s	2.01×10^{-3}	deg/s

After the measured acceleration values were integrated a second time within SimSat II's SIMULINK model, it was experimentally determined that the LN-200 bias causes an angular position drift of $1.1^\circ/\text{min}$ about the 1-axis, $0.3^\circ/\text{min}$ about the 2-axis, and $0.2^\circ/\text{min}$ about the 3-axis. Although relatively small when compared to the rest-to-rest maneuvers conducted in this research, as SimSat II attempts to maintain attitude the ever present bias causes the reaction wheels to saturate more quickly. Thus, a bias offset is accounted for in the SimSat II SIMULINK model. The drift rates prior to and after the bias offset are presented in Table 3.7.

Table 3.7: LN-200 Bias Correction

Axis	Before	After
1	$1.1^\circ/\text{min}$	$0.160^\circ/\text{min}$
2	$0.3^\circ/\text{min}$	$0.009^\circ/\text{min}$
3	$0.2^\circ/\text{min}$	$0.002^\circ/\text{min}$

3.4.8 PID Tuning . Proportional K_P , integral K_I , and derivative gains K_D were dynamically tuned using the dSPACE ControlDesk software (see Figure 3.14). The methodology used to tune K_P , K_I , and K_D followed the manual tuning guidance from the EPOS 70/10 *Getting Started* document [28].

An initial value of zero was assigned to K_P , K_I , and K_D . Proportional gain K_P was then increased incrementally. At the same time, K_D was increased incrementally at a value of two times K_P . When an acceptable response was achieved, K_D was increased to diminish overshoot. Lastly, K_I was increased until SimSat II was capable of maintaining attitude control within $\pm 0.1^\circ$. The resultant gain values are presented in Table 3.8. These PID controller settings were used for all experiments conducted in this research.

Table 3.8: SimSat II PID Gain Settings

Axis	K_P	K_I	K_D
1	1.0	0.1	3.0
2	1.0	0.1	3.0
3	0.7	0.1	4.0

3.5 *Summary*

Chapter III presented the methodology used to design, build, and test the reaction wheel ACS. Pertinent hardware and software on-board SimSat II and the interfaces between the two were discussed. Lastly, the efforts that led to characterization subsystems' performance were described.

IV. Results and Analysis

Chapter IV evaluates the performance of the reaction wheel ACS against the following measures:

1. Reaction wheels shall generate sufficient torque to perform the fastest slew maneuvers.
 - (a) Positioning accuracy shall be $\pm 0.01^\circ$.
 - (b) A $\pm 10^\circ$ rest-to-rest maneuver about the 1- and 2-axis shall be demonstrated within 10 seconds.
 - (c) A $\pm 30^\circ$ rest-to-rest maneuver about the 3-axis shall be demonstrated within 10 seconds.
 - (d) SimSat II's angular velocity shall not exceed $180^\circ/\text{s}$.
2. Reaction wheel torque shall equal the worst case anticipated disturbance torque.
3. Reaction wheels must have sufficient momentum storage.

Throughout Chapter IV relevant results with accompanying discussion are presented according to the experiment being performed. In total, three experiments were conducted: positioning accuracy, rest-to-rest maneuvers, and disturbance torques. Each experiment is analyzed with respect to the 1-, 2-, and 3-axis. At the conclusion of each experiment a summary is presented comparing the three axes.

The complete set of experimental results, however, is presented in Appendix B. Each page of Appendix B displays one figure consisting of 12 subfigures arranged in a 4x3 array. Each column displays the experimental results according to an axis of rotation. The 1-axis is represented in the first column and is plotted with the color blue, the 2-axis is represented in the second column and is plotted with the color red, and the 3-axis is represented in the third column and is plotted with the color green. The caption beneath each subfigure indicates the variable being measured, and the figure title located at the bottom of the page indicates the experiment.

The experimental data results in Appendix B were collected using the dSPACE ControlDesk software application. The dSPACE ControlDesk captures data for a time

interval defined by the user. At the conclusion of the time interval the dSPACE ControlDesk writes the captured data to disk and then continues to collect data. While the dSPACE ControlDesk writes the data to disk, no additional data is being collected. Thus, a gap in sampled data occurs.

A data collection interval of 10 s was prescribed for this research. Figure 4.1 shows a sample data set with gaps in data occurring approximately 10 s apart. Also shown in Figure 4.1 is the pause in time between when the operator begins collecting data and when the experiment starts.

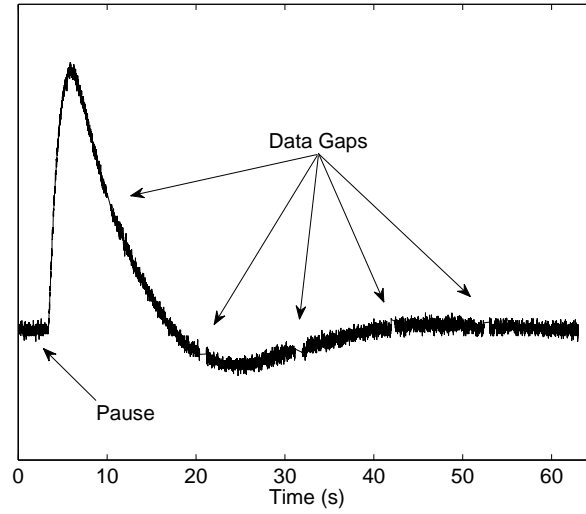
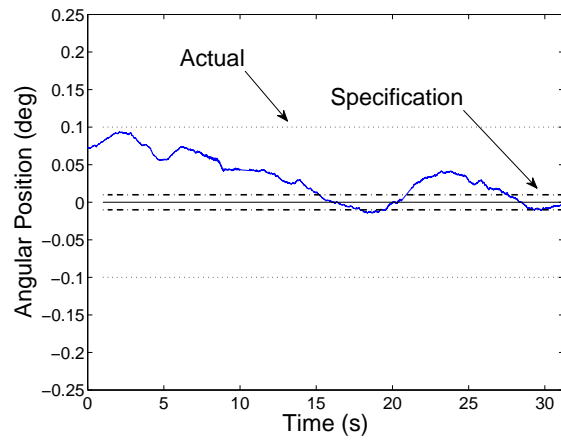


Figure 4.1: Experimental Data Collections

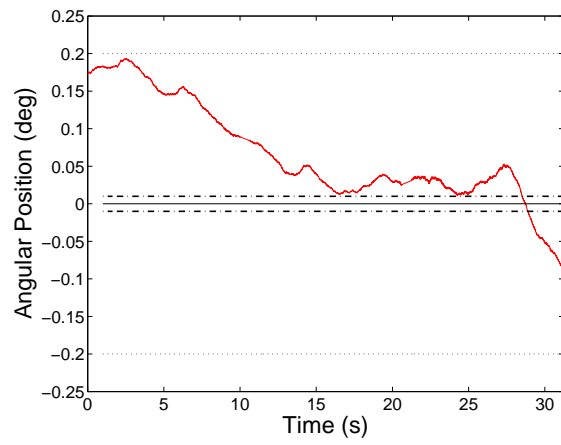
4.1 Positioning Accuracy

To determine the pure positioning accuracy of SimSat II, angular position measurements were collected while SimSat II maintained attitude. During this experiment, SimSat II was not commanded to maneuver nor were any disturbance torques applied. Figure 4.2 presents the findings. All three axes traverse the region of $\pm 0.01^\circ$ but none consistently hold attitude within $\pm 0.01^\circ$. Table 4.1 summarizes the position accuracy results.

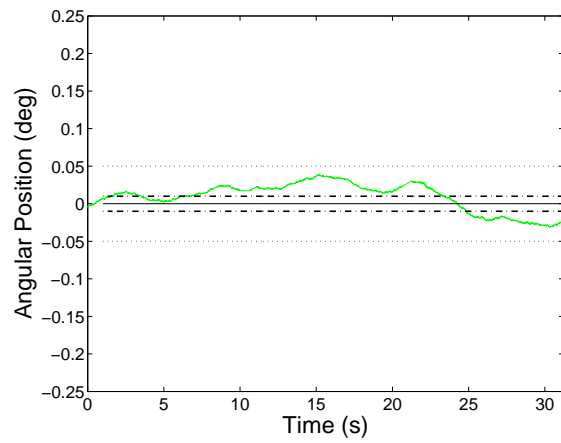
In all cases, the position accuracy specification was not consistently met. The deficiency in position accuracy, however, can readily be mitigated by adjusting the PID gain settings K_P , K_I , and K_D . Although beyond the scope of this research, numerical



(a) 1-Axis



(b) 2-Axis



(c) 3-Axis

Figure 4.2: Attitude Hold

Table 4.1: Positioning Accuracy of the Reaction Wheel ACS

Axis	Positioning Accuracy
1	$\pm 0.10^\circ$
2	$\pm 0.20^\circ$
3	$\pm 0.05^\circ$

methods and experimental techniques can be investigated to optimally tune the PID controller.

Effort can also be extended toward mitigating gravitational torques. Positioning SimSat II's COM, such that it is coincident with the COR, can be improved by investigating alternate counterbalancing methods. Additionally, stiffer materials can be used in counterbalancing. Previously, the assumption was made that SimSat II is a rigid body. The extension rods holding the large masses beneath SimSat II's tabletop deck, however, are noticeably less than rigid.

4.2 *Rest-to-Rest Maneuvers*

It is possible to predict the amount of time required to perform a rest-to-rest maneuver about SimSat II's 1-, 2-, or 3-axis following the same approach as that used in Section 3.4.1 for sizing the reaction wheels. Rearranging Equation (3.3) we are able to calculate the theoretical rest-to-rest maneuver time according to

$$t = \sqrt{\frac{2\beta I_{ii}}{M_{w_{i\max}}}} \quad (4.1)$$

where β is the angular displacement in radians, I_{ii} is the principal MOI, $M_{w_{i\max}}$ is the maximum possible applied torque, and the subscript i corresponds to the axis of rotation.

For this research, settling time for a rest-to-rest maneuver is defined as the time taken for the satellite to start from rest, perform the maneuver, and finish within $\pm 0.01^\circ$ of the desired angular position.

4.2.1 *1-Axis Reorientation* . SimSat II was commanded to perform positive 10° and 20° rest-to-rest maneuvers about the 1-axis. Equation (4.1) predicts that the 10° maneuver should theoretically take 3.74 s, and the 20° maneuver should take 5.29 s; both less than the 10 s threshold for a 10° maneuver.

Figure 4.3 shows that SimSat II exceeds the 10 s threshold for the 10° maneuver. The data set for the 10° maneuver was inconclusive as to how long the settling time would be. The operator stopped the data collection prematurely. At the experiment's conclusion with time equal to 37.601 s, SimSat II's angular position about the 1-axis is 10.0462° .

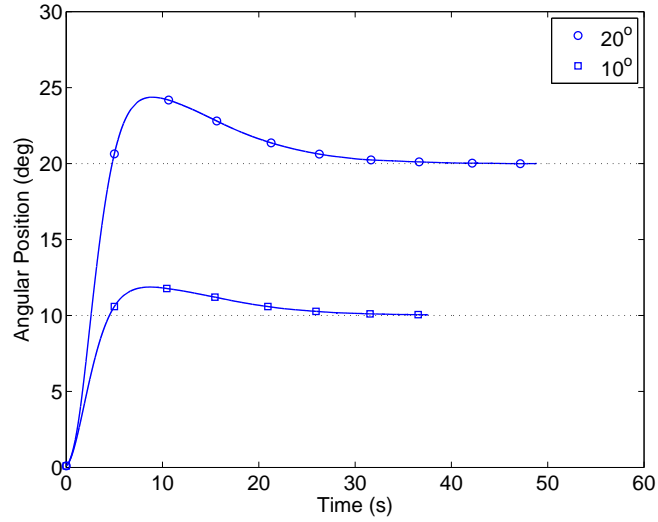


Figure 4.3: Settling Time for Rest-to-Rest Maneuvers about 1-Axis

Equation (4.2) shows how the deviation from the position accuracy specification can be expressed in terms of percent difference. The 10° rotation about the 1-axis exhibits a 0.46% difference from the $\pm 0.01^\circ$ threshold

$$\% \text{ Difference} = \frac{|\text{Actual} - \text{Specification}|}{(\text{Actual} + \text{Specification})/2} \times 100 . \quad (4.2)$$

A phenomenon worth observing during the rest-to-rest maneuver is the principle of conservation of angular momentum. Figure 4.4 illustrates that the angular velocity of the reaction wheel about the 1-axis ψ_{w_1} starts the maneuver spinning at a rate of 128 rpm. The principle of conservation of momentum states that for a rest-to-rest maneuver, the

reaction wheel should begin and end the maneuver rotating at the same angular velocity. The final angular velocity of ψ_{w_1} is 440 rpm; a residual angular velocity of 312 rpm, or better put $0.0706 \text{ kg} \cdot \text{m}^2/\text{s}$ of momentum is present. The cause of the residual angular velocity is air drag.

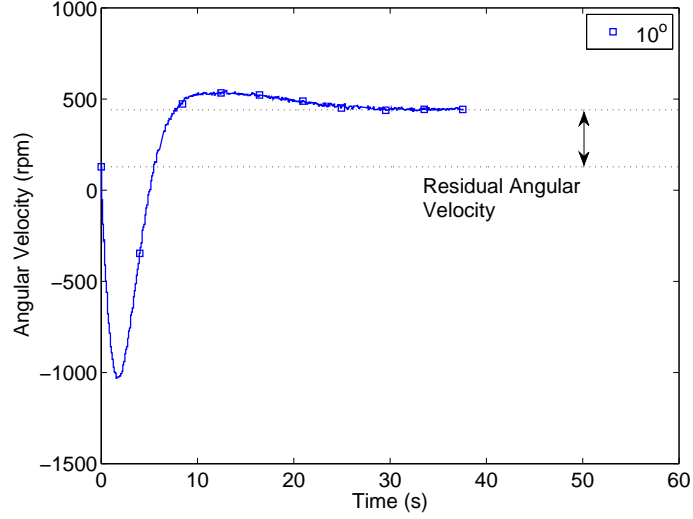


Figure 4.4: Residual Angular Velocity ψ_{w_1} for Rest-to-Rest Maneuver about 1-Axis

McFarland characterized air drag effects when SimSat II was equipped solely with the fan thruster ACS [33]. Strict time constraints imposed upon this research prohibited characterizing the effect air drag has upon SimSat II. It is predicted, however, that the addition of the reaction wheel ACS would cause the effects of air drag to be more prominent. The external torque caused by air drag leads to the residual angular velocity being present.

4.2.2 2-Axis Reorientation . SimSat II was commanded to perform positive 10° and 20° rest-to-rest maneuvers about the 2-axis. Equation (4.1) predicts that the 10° maneuver should theoretically take 3.04 s, and the 20° maneuver should take 4.30 s; both less than the 10 s threshold for a 10° maneuver.

Figure 4.5 shows that SimSat II exceeds the 10 s threshold for a 10° maneuver. At the experiment's conclusion with time equal to 48.216 s, SimSat II's angular position about the 2-axis is 10.0154° ; a 0.15% difference from the $\pm 0.01^\circ$ threshold.

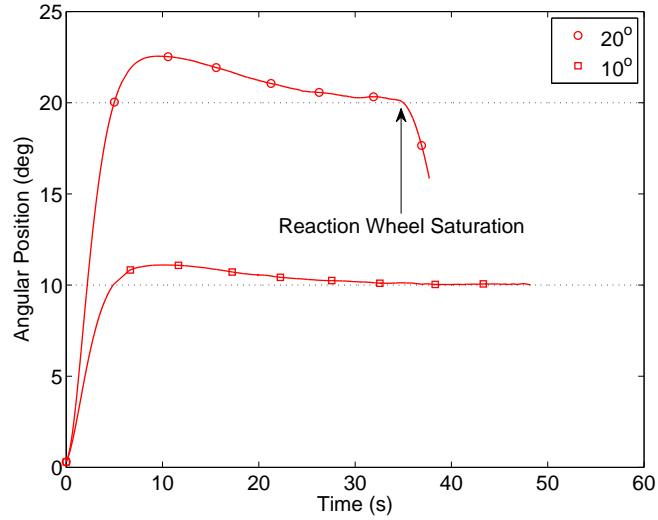


Figure 4.5: Settling Time for Rest-to-Rest Maneuvers about 2-Axis

As SimSat II was decreasing its angular position error in the 20° maneuver, Figure 4.5 indicates that at time equal to 34.397 s the satellite lost attitude control authority over the 2-axis. Constant angular velocity of the reaction wheel beginning at time equal to 34.397 s in Figure 4.6 concludes that attitude control was lost because ψ_{w_2} saturated at -9,000 rpm. Equation (3.18) attests that a change in angular velocity is necessary to counter disturbance torques. Without the ability to change angular velocity (saturation), attitude control is lost.

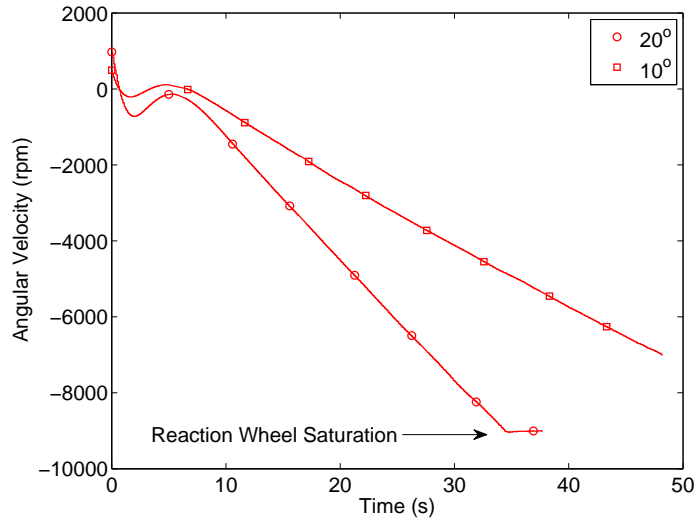


Figure 4.6: Measured Angular Velocity ψ_{w_2} for Rest-to-Rest Maneuver about 2-Axis

The maximum torque that can be applied by the reaction wheel ACS about the 2-axis is calculated in Section 3.4.3.3 to be $0.3395 \text{ N} \cdot \text{m}$. Additionally, a $1 \text{ N} \cdot \text{m}$ torque constraint was imposed upon all three axes in Section 3.4.3.3. Figure 4.7(a) demonstrates that during the 20° rest-to-rest maneuver, the theoretical maximum torque about the 2-axis $M_{w_{2max}}$ was exceeded, and the $1 \text{ N} \cdot \text{m}$ constraint prevented any additional torque from being commanded.

Equation (3.18) states that torque M_w is directly affected by the time step Δt in which it is applied. In Section 3.4.4.4, Δt was fixed at 100 ms. Figure 4.7(b) shows torque changing at intervals other than the predefined time step of 100 ms; therefore, M_w is capable of exceeding its theoretical limit and attaining the $1 \text{ N} \cdot \text{m}$ constraint. Additional analysis on the unpredictability of Δt is presented in Section 4.3.

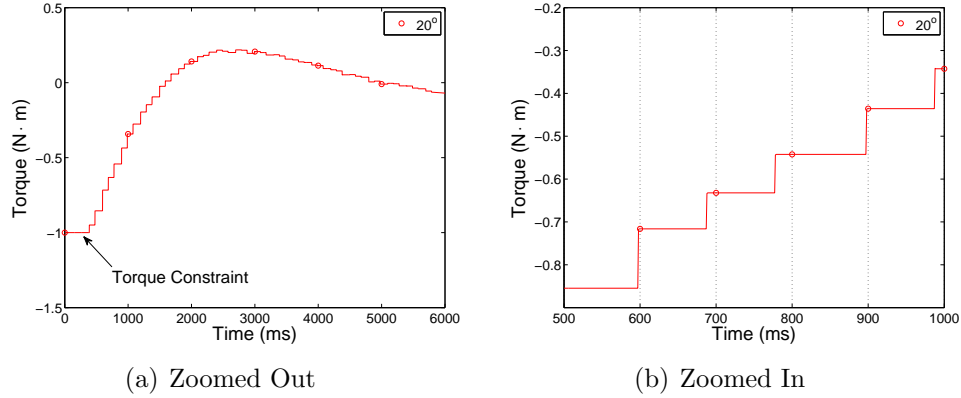


Figure 4.7: Commanded Torque M_{w_2} for Rest-to-Rest Maneuver about 2-Axis

4.2.3 3-Axis Reorientation . SimSat II was commanded to perform positive 10° , 20° and 30° rest-to-rest maneuvers about the 3-axis. Equation (4.1) predicts that the the 30° maneuver should take 5.67 s, the 20° maneuver should take 4.67 s, and the 10° maneuver should theoretically take 3.27 s all less than the 10 s threshold for a 30° maneuver.

Figure 4.8 shows that SimSat II exceeds the 10 s threshold for a 30° maneuver. At the experiment's conclusion with time equal to 69.2650 s, SimSat II's angular position about the 3-axis is 30.0780° ; a 0.26% difference from the $\pm 0.01^\circ$ threshold.

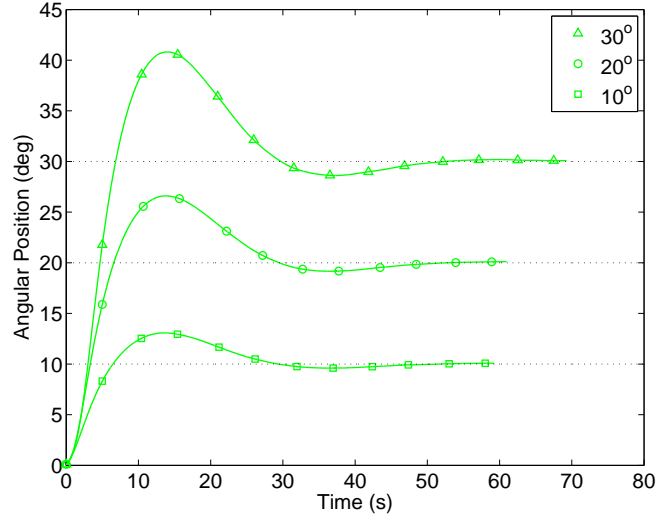


Figure 4.8: Settling Time for Rest-to-Rest Maneuvers about 3-Axis

During the 30° rest-to-rest maneuver Figures 4.9(a) and 4.9(b) exhibit anomalous perturbations throughout the reorientation maneuver. As SimSat II rotates about the 3-axis, ψ_{w_1} and ψ_{w_2} should accelerate at constant rates as they counteract gravitational torques due to SimSat II's COM not being coincident with its COR. The deviations in the slope of ψ_{w_1} and ψ_{w_2} affirm that SimSat II's POI cannot be assumed to equal zero. The presence of POI causes centrifugal force to exert a disturbance torque upon the satellite. The anomalous bumps in the curves of Figure 4.9 are the reaction wheels counteracting the centrifugal disturbance torques as the satellite performs its reorientation maneuver.

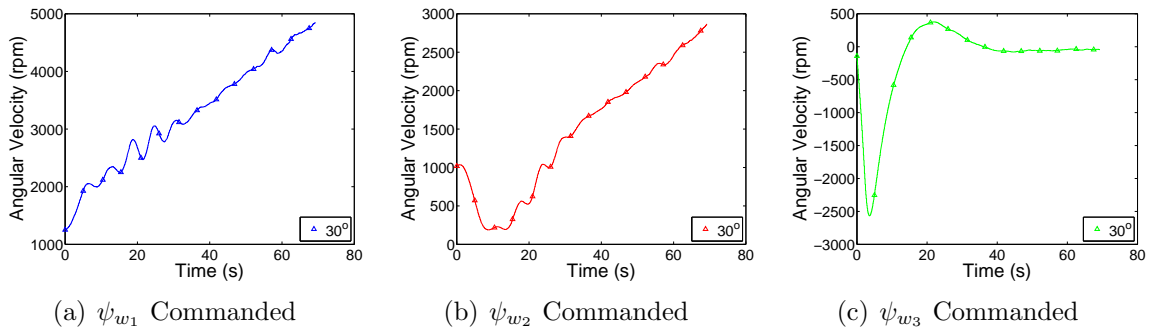


Figure 4.9: Positive 30° Rest-to-Rest Maneuver about 3-Axis

4.2.4 *Rest-to-Rest Summary* . In summary, Sections 4.2.1–4.2.3 conclude that SimSat II exceeds the 10 s threshold for the 10° and 30° maneuvers. Additionally, SimSat II maintained $\pm 0.01^\circ$ pointing accuracy in only one of the seven reorientation maneuvers presented—positive 20° about the 2-Axis. In all cases, the settling time and position accuracy can readily be mitigated by adjusting the PID gain settings K_P , K_I , and K_D . Although beyond the scope of this research, numerical methods and experimental techniques can be investigated to optimally tune the PID controller.

Figure 4.10 summarizes that SimSat II is consistently capable of performing a rest-to-rest maneuver. Table 4.2 compares the angular position of SimSat II at the conclusion of each rest-to-rest maneuver to the specification. Proof of concept has thus been evaluated and confirmed positive.

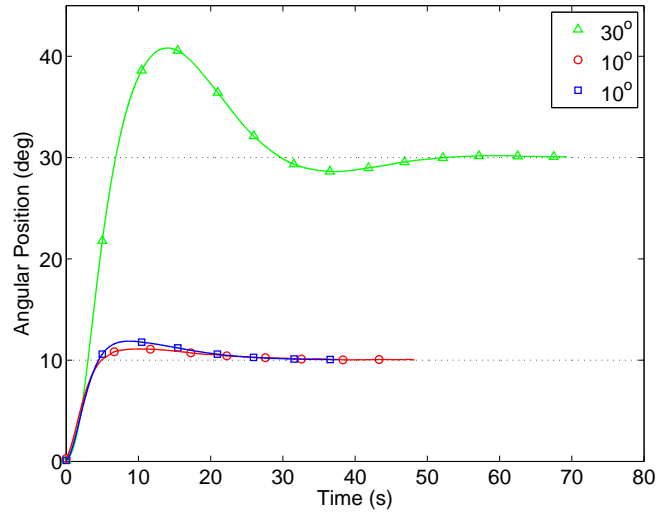


Figure 4.10: Rest-to-Rest Maneuvers Performance Summary

Table 4.2: Rest-to-Rest Maneuvers Performance Summary

Axis	Positioning Accuracy	% Difference
1	10.0462°	0.46%
2	10.0154°	0.15%
3	30.0780°	0.26%

Per the performance specifications sought after by the AFIT faculty, Figure 4.11 demonstrates that SimSat II's angular velocity does not exceed the $180^\circ/\text{s}$ threshold while performing a rest-to-rest maneuver.

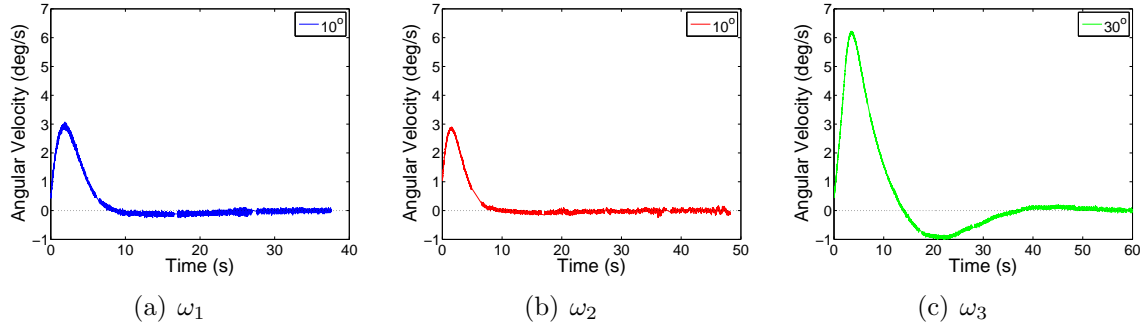


Figure 4.11: Angular Velocity of SimSat II for Rest-to-Rest Maneuvers

4.3 The Inconsistency of Δt

The ability to apply a known torque is predicated on being able to fix one's time step Δt as shown in Equation (4.3)

$$M_w = D_w \dot{\psi}_w \quad (4.3a)$$

$$= D_w \frac{\Delta \psi_w}{\Delta t} . \quad (4.3b)$$

The evaluation of the reaction wheel ACS to apply a known torque concludes that measured torque never equals the predicted torque value. Great care was taken to fix Δt and to assure that commands were impulsively submitted to the EPOS controllers in Section 3.4.4.4. Upon further investigation, it can be seen in Figure 4.12 that although Δt has seemingly been fixed at a value 100 ms, experimental data indicates that the time between impulse commands varies. Future analysis must be conducted toward understanding the timing precision of the SimSat II SIMULINK model, the dSPACE MicroAutoBox, and the behavior of CAN communications protocol or else full command authority of the reaction wheel ACS will never be realized.

Although never capable of fulfilling its potential torque output, Section 4.4 presents that SimSat II does demonstrate the ability to command lesser torques.

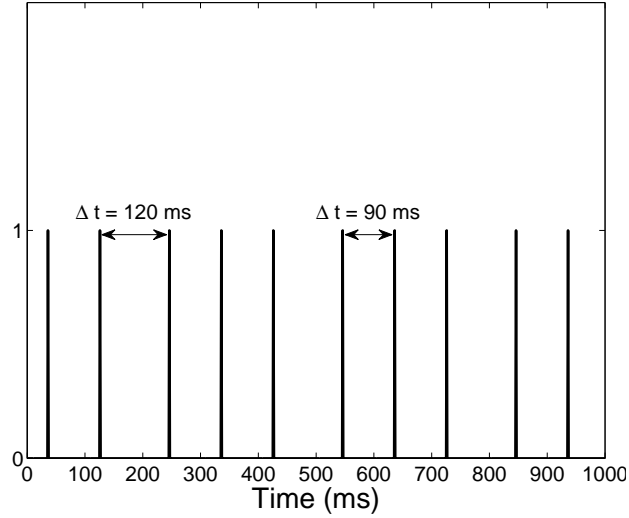


Figure 4.12: EPOS 70/10 Command Intervals

4.4 Disturbance Torques

The maximum torque M_w that can be applied by the reaction wheel ACS about the 1-, 2-, and 3-axis was calculated in Section 3.4.3.3 to be $0.3395 \text{ N} \cdot \text{m}$, $0.3395 \text{ N} \cdot \text{m}$, and $0.6590 \text{ N} \cdot \text{m}$, respectively. The predicted maximum torque capability of SimSat II's reaction wheel ACS can be evaluated by rearranging Equation (3.22). For a known length l , a maximum applied mass m_{max} can be calculated. The resultant expression is Equation (4.4)

$$m_{max} = \frac{M_{w_i}}{gl} \quad (4.4)$$

where M_{w_i} is the applied torque, g is the acceleration due to gravity, l is the radius of SimSat II's tabletop deck, and the subscript i denotes the axis of rotation.

To evaluate whether the torque generated by the reaction wheel ACS equals the worst case anticipated disturbance torque, the test set-up is depicted in Figure 4.13. The disturbance torque caused by the applied mass is described by Equation (3.22) and is illustrated in Figure 4.13(a). Figure 4.13(b) shows the applied mass hanging from a string at a distance l from SimSat II's COR.

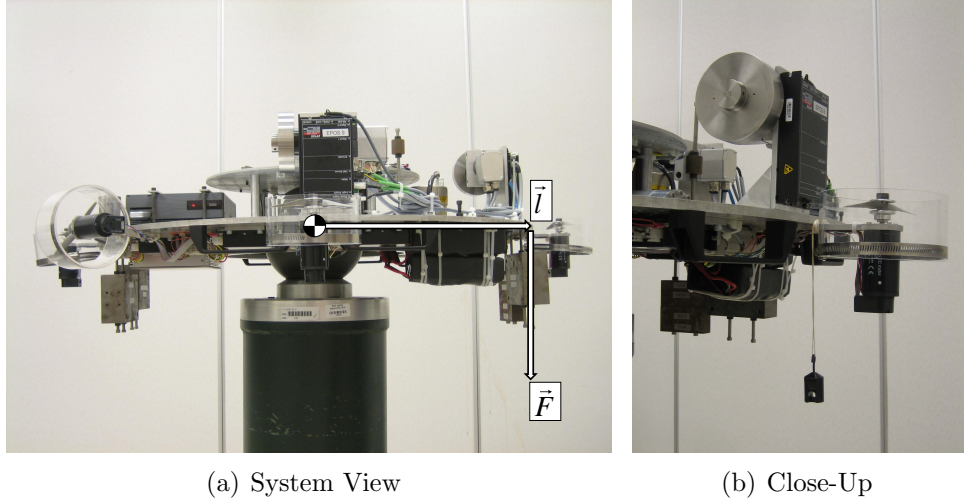


Figure 4.13: Disturbance Torque Evaluation

Likewise, a predetermined amount of mass m can be selected to apply a disturbance torque onto SimSat II. One could then determine the duration of time for which the reaction wheel ACS can theoretically equal the disturbance torque before saturation occurs. By equating Equations (3.18) and (3.22), the duration of time can be expressed as

$$time = \frac{D_i \Delta\psi}{mgl} \quad (4.5)$$

where D_i is the principal MOI of the reaction wheel about its axis of rotation, and $\Delta\psi$ is the reaction wheel's change in angular velocity from time equal to zero until saturation occurs. The reaction wheel ACS is assumed to start at rest; therefore, $\Delta\psi$ is equal to the rpm constraint of $\pm 9,000$ rpm as defined in Section 3.4.3.1. With an angular rate limit of $\pm 9,000$ rpm, according to Equation (2.41), the total momentum the reaction wheel ACS can store is $8.03 \text{ kg} \cdot \text{m}^2/\text{s}$ provided all three reaction wheels saturate simultaneously.

4.4.1 1-Axis Disturbance Torque . To impart a disturbance torque about the 1-axis, a mass was hung from the perimeter of SimSat II's tabletop deck as shown in Figure 4.13. The maximum applied torque M_w about the 1-axis that can be applied by the reaction wheel ACS is $0.3395 \text{ N} \cdot \text{m}$. The radius of SimSat II's tabletop deck l is 45.72 cm . Using Equation (4.4), the reaction wheel ACS can theoretically counteract a

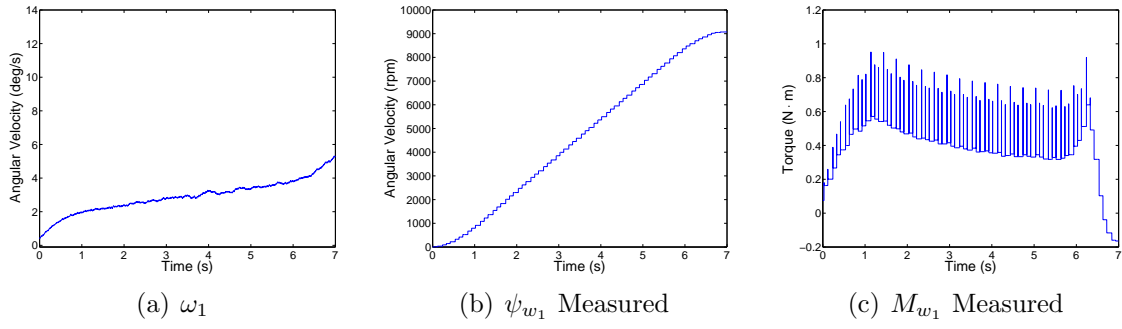


Figure 4.14: Positive Torque about 1-Axis Using 75 g Mass

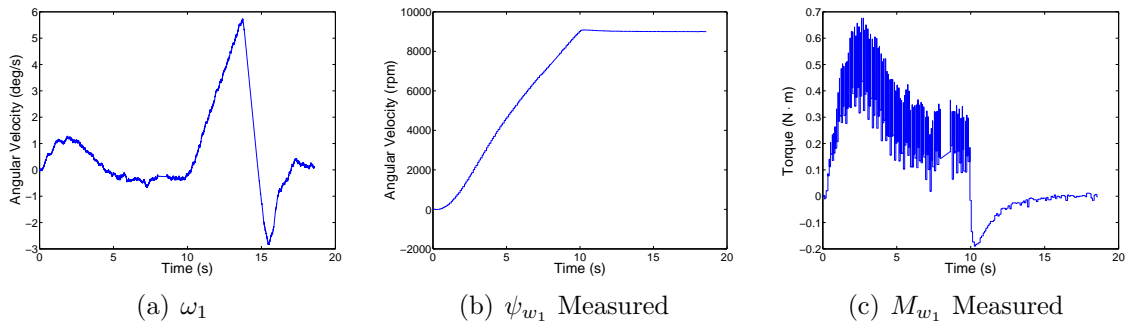


Figure 4.15: Positive Torque about 1-Axis Using 40 g Mass

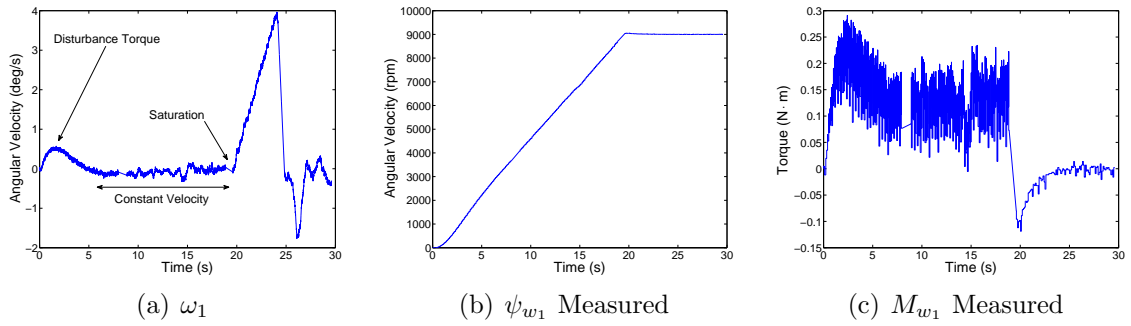


Figure 4.16: Positive Torque about 1-Axis Using 20 g Mass

disturbance torque imparted by a 75.72 g mass. Additionally, Equation (4.5) predicts that a 0.3395 N · m torque imparted by the 75.72 g mass can be withstood by the reaction wheel ACS for a total of 6 s. Similarly, a 75 g mass can be withstood for 6.06 s, a 40 g mass for 11.36 s, and a 20 g mass for 22.72 s.

Figure 4.16(a) is best used to describe what occurs throughout the hanging mass experiment. As the experiment begins, SimSat II rolls about the positive x-axis due to the disturbance torque. After some time the reaction wheel ACS counteracts the disturbance torque. While accelerating at a constant rate, the reaction wheel ACS proceeds to rotate SimSat II back toward its initial state at a constant velocity. Finally, the reaction wheel ACS saturates forcing SimSat II to succumb to the disturbance torque caused by the hanging mass.

Figure 4.14(a) demonstrates that the reaction wheel ACS was not capable of counteracting the 75 g disturbance torque. Conversely, Figure 4.14(b) suggests otherwise since ψ_{w_1} saturated at a time greater than 6.06 s. However, we are reminded by Figure 4.14(c) and the inconsistency of Δt in Section 4.3 that Δt is inconsistent, and, therefore, the commanded torque is not always achieved.

Figures 4.15(a) and 4.16(a) conclude that for the 40 g and 20 g cases, the reaction wheel ACS was able to counter the disturbance torque for approximately 10 s and 20 s, respectively. Figures 4.15(b) and 4.16(b) support this evidence by showing the angular rate of the reaction wheel about the 2-axis ψ_{w_2} achieving a saturation rate of +9,000 rpm at approximately the same times of 10 s and 20 s, respectively.

4.4.2 2-Axis Disturbance Torque . The principal MOI of the reaction wheel that commands torque about the 2-axis is identical to that of the 1-axis. The maximum applied torque M_w about the 2-axis that can be applied by the reaction wheel ACS is therefore, 0.3395 N · m. Equation (4.4) once again predicts the reaction wheel ACS can theoretically counteract a disturbance torque imparted by a 75.72 g mass. Additionally, Equation (4.5) repeatedly predicts that a 0.3395 N · m torque imparted by the 75.72 g mass can be withstood by the reaction wheel ACS for a total of 6 s. Similarly, a 75 g mass can be withstood for 6.06 s, a 40 g mass for 11.36 s, and a 20 g mass for 22.72 s.

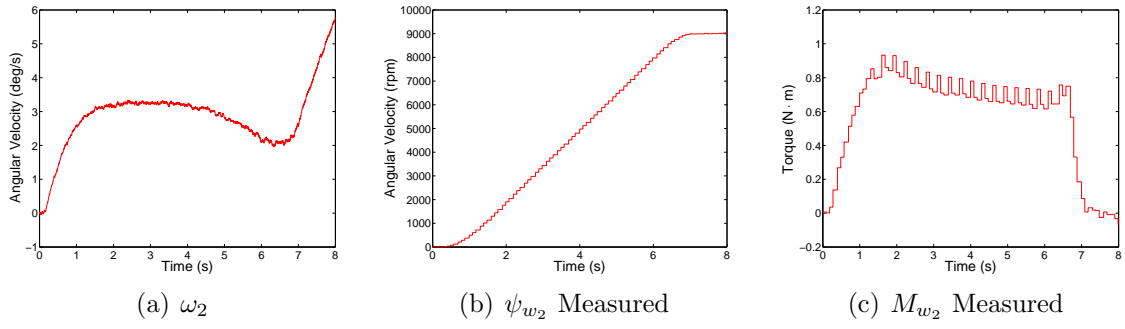


Figure 4.17: Positive Torque about 2-Axis Using 75 g Mass

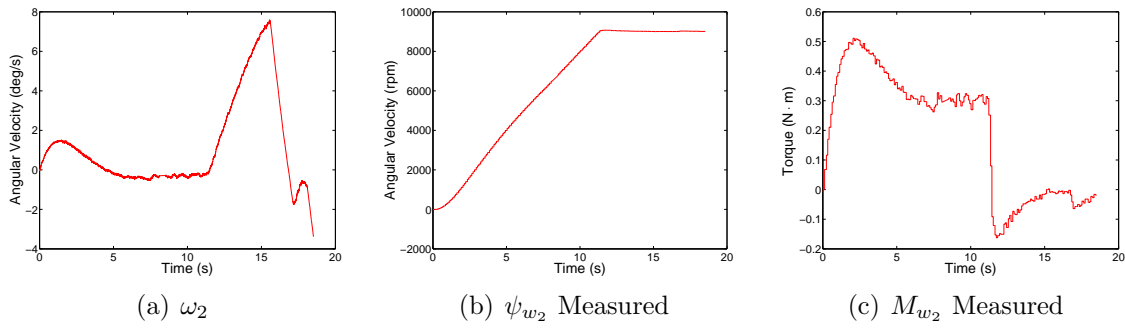


Figure 4.18: Positive Torque about 2-Axis Using 40 g Mass

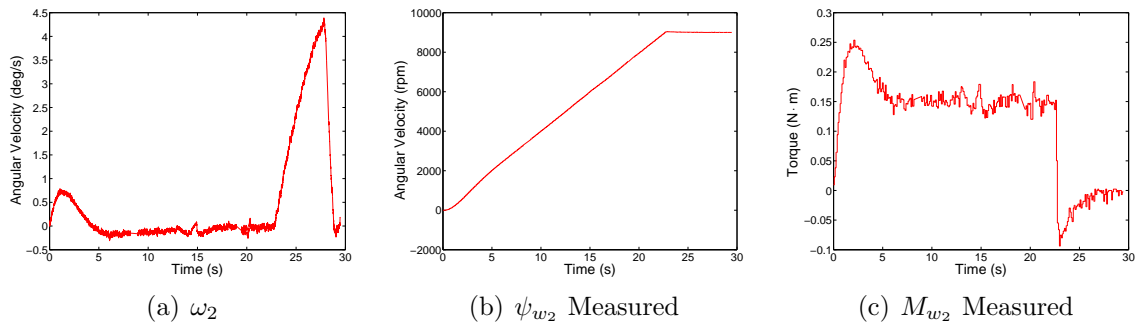


Figure 4.19: Positive Torque about 2-Axis Using 20 g Mass

Figure 4.17(a) demonstrates that the reaction wheel ACS was capable of counteracting the 75 g disturbance torque, if only for a brief amount of time between approximately 4 and 6.5 s. Figure 4.17(b) supports this evidence as ψ_{w_2} saturates at a time of approximately 6.5 s. Unlike the 1-axis, the 2-axis is able to briefly withstand the 75 g disturbance torque. The lesser MOI of the 2-axis ($4.5 \text{ kg} \cdot \text{m}^2$) compared to that of the 1-axis ($6.8 \text{ kg} \cdot \text{m}^2$) contributes to the improved performance of the reaction wheel ACS. Regardless, Figure 4.17(c) serves as a reminder that the unpredictability of Δt causes diminished torque control.

Figures 4.18(a) and 4.19(a) conclude that for the 40 g and 20 g cases, the reaction wheel ACS was able to counter the disturbance torque for approximately 11 s and 22 s, respectively. Figures 4.18(b) and 4.19(b) support this evidence by showing the angular rate of the reaction wheel about the 2-axis ψ_{w_2} achieving a saturation rate of +9,000 rpm at approximately the same times of 11 s and 22 s, respectively.

4.4.3 3-Axis Disturbance Torque . The maximum applied torque M_w about the 3-axis that can be applied by the reaction wheel ACS is $0.6590 \text{ N} \cdot \text{m}$. The radius of SimSat II's tabletop deck l is 45.72 cm. Using Equation (4.4), the reaction wheel ACS can theoretically counteract a disturbance torque imparted by a 146.98 g mass. Additionally, Equation (4.5) predicts that a $0.6590 \text{ N} \cdot \text{m}$ torque imparted by the 146.98 g mass can be withstood by the reaction wheel ACS for a total of 6 s. Similarly, a 145 g mass can be withstood for 6.08 s, a 100 g mass for 8.82 s, and a 50 g mass for 17.64 s.

Figures 4.20(a) and 4.21(a) demonstrate that the reaction wheel ACS was not capable of counteracting the 145 g or 100 g disturbance torques. Conversely, Figures 4.20(b) and 4.21(b) suggests otherwise since ψ_{w_3} saturates at a times greater than 6.08 s and 8.82 s, respectively. However, we are reminded by Figure 4.20(c) and the inconsistency of Δt in Section 4.3 that Δt is inconsistent, and, therefore, the commanded torque is not always achieved.

Figure 4.22(a) concludes that the reaction wheel ACS was capable of counteracting the disturbance torque caused by the 50 g mass for approximately 17 s. Figure 4.22(b) supports this claim by showing the angular rate of the reaction wheel about the 3-axis ψ_{w_3}

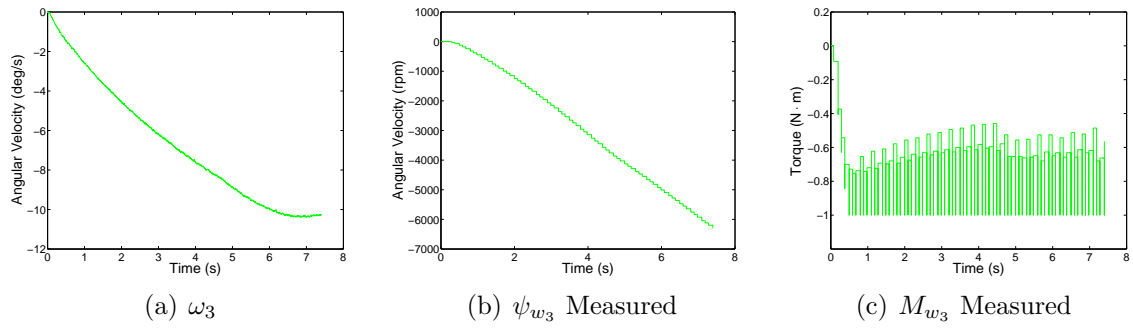


Figure 4.20: Negative Torque about 3-Axis Using 145 g Mass

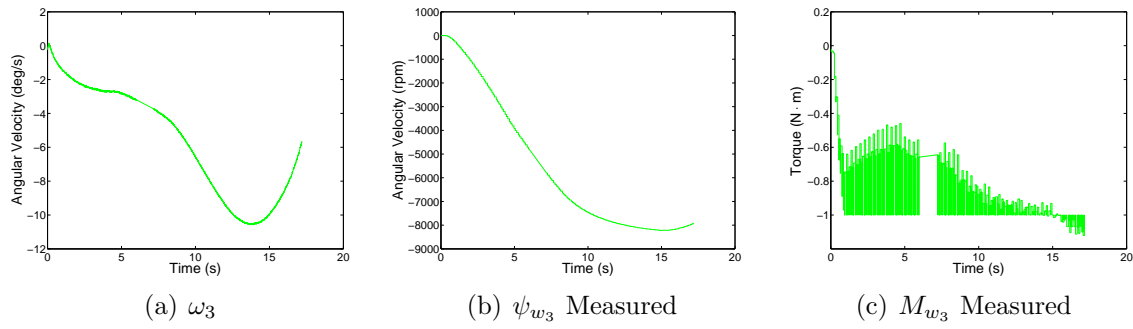


Figure 4.21: Negative Torque about 3-Axis Using 100 g Mass

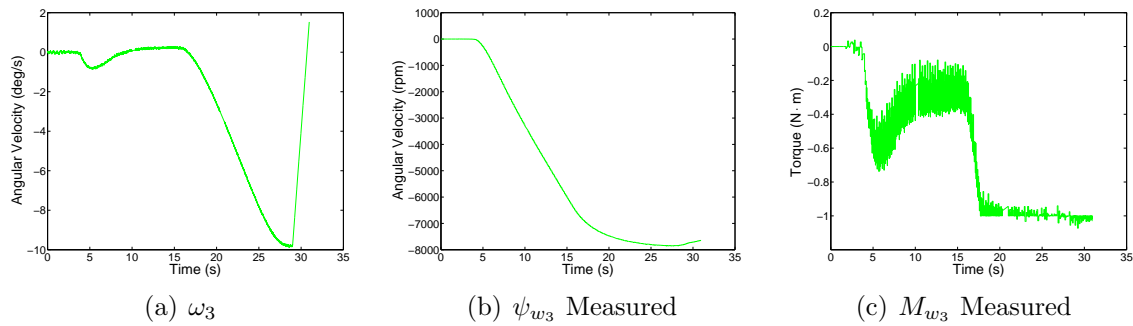


Figure 4.22: Negative Torque about 3-Axis Using 50 g Mass

accelerating at a constant rate until approximately the same times of 17 s. The reaction wheel does not attain the angular velocity saturation limit of -9,000 rpm because the torque saturation limit of 1 N · m is achieved in Figure 4.22(c).

4.4.4 Disturbance Torque Summary . Table 4.3 summarizes the disturbance torque performance of the reaction wheel ACS. The top-half of the table contains the predicted theoretical performance values. The bottom-half of the table contains the measured experimental performance values. Dashed marks (—) indicate that the mass was not used as a disturbance torque for that particular axis of rotation. The ‘X’ marks indicate the reaction wheel ACS was incapable of equaling the applied disturbance torque.

Table 4.3: Disturbance Torques Performance Summary

			20 g	40 g	50 g	75 g	100 g	145 g
Theoretical	3-Axis	M_3 (N · m)	—	—	0.2242	—	0.4484	0.6501
		time (s)	—	—	17.64	—	8.82	6.08
	2-Axis	M_2 (N · m)	0.0897	0.1793	—	0.3363	—	—
		time (s)	22.72	11.36	—	6.06	—	—
	1-Axis	M_1 (N · m)	0.0897	0.1793	—	0.3363	—	—
		time (s)	22.72	11.36	—	6.06	—	—
Actual	3-Axis	M_3 (N · m)	—	—	0.7	—	1.0	1.0
		time (s)	—	—	16	—	X	X
	2-Axis	M_2 (N · m)	0.25	0.5	—	0.9	—	—
		time (s)	22	11	—	6.5	—	—
	1-Axis	M_1 (N · m)	0.3	0.7	—	0.9	—	—
		time (s)	20	10	—	X	—	—

It can be seen that as the applied disturbance torque increases, the reaction wheel ACS has greater difficulty maintaining attitude. Additionally, the reaction wheel ACS has greater difficulty maintaining attitude for the axes with greater MOI values. Table 4.3

correlates that for the MOI relationship of $C > A > B$, the 3-axis C has greater difficulty than the 1-axis A , and the 1-axis has greater difficulty than the 2-axis B as the applied torques increase.

The larger the MOI, the more difficult it is to accelerate about an axis of rotation. Equation (2.20) can be used to calculate the maximum acceleration rate about each of SimSat II's principal axes. Accordingly, the maximum acceleration rates of α_1 , α_2 , and α_3 are 0.0499, 0.0757, and 0.0652 rad/s², respectively.

One might wonder why the reaction wheel ACS was capable of withstanding the 40 g mass about the 1-axis but incapable of withstanding the 100 g mass about the 3-axis seeing that α_3 is greater than α_1 . The 40 g mass disturbance torque about the 1-axis is 52.82% of its maximum 75.72 g value whereas the 100 g mass disturbance torque about the 3-axis is 68.04% of its maximum 146.98 g value. Perhaps the reaction wheel ACS is incapable of counteracting a disturbance torque that is 68.04% of its maximum 75 g total (52 g). Future research can be conducted to determine the upper limit disturbance torque a user can expect to counteract from the SimSat II reaction wheel ACS.

Figure 4.23 demonstrates how Δt varies within a \pm tolerance. The approximate time periods of 5–8 s and 28–31 s show that Δt most likely varies on the minus side of the tolerance. The torque constraints of ± 1 N · m prevent additional insight into whether

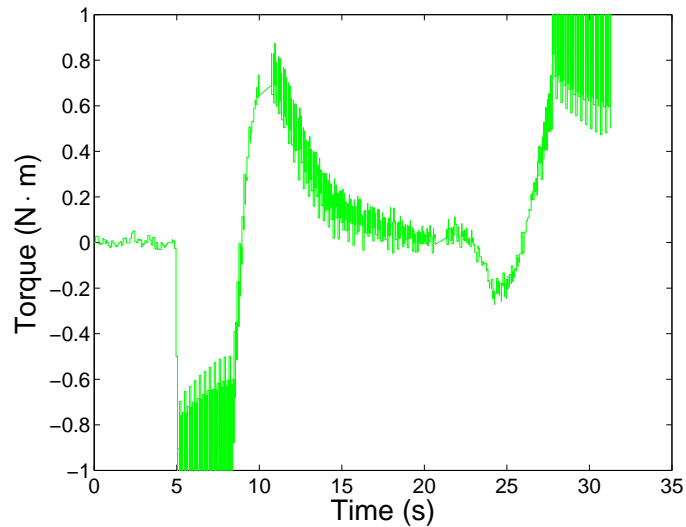


Figure 4.23: Effect of Δt on Measured Torque

Δt varies on both sides of the tolerance interval. The approximate time period of 12–23 s demonstrates that Δt varies on the plus and minus side of the tolerance. Again, proof of concept has been evaluated and confirmed positive; however, future analysis must be conducted toward understanding the timing precision of the SimSat II SIMULINK model, the dSPACE MicroAutoBox, and the behavior of CAN communications protocol or else full command authority of the reaction wheel ACS will never be realized.

V. Conclusions and Recommendations

5.1 Conclusions

The objective of this research was to design, build, test, and evaluate the performance of a reaction wheel ACS on-board AFIT's second-generation satellite simulator, SimSat II. The end result of this research objective was to produce a satellite simulator capable of maintaining position accuracy within $\pm 0.01^\circ$ and performing $\pm 10^\circ$ rest-to-rest maneuvers within 10 s about the 1- and 2-axis and $\pm 30^\circ$ within 10 s about the 3-axis; all while overcoming the worst case anticipated disturbance inputs.

The methodology of this research followed in concordance with the research objective. First, a preliminary design of one reaction wheel assembly was created. Then, improving upon the lessons learned from the preliminary design, an ACS consisting of three reaction wheel assemblies was built along with the necessary SIMULINK control logic. Following the build phase of this research, the software logic underwent extensive testing. Lastly, with SimSat II in its best possible set-up, the reaction wheel ACS was evaluated in a series of experiments.

The reaction wheel ACS and the PID controller exceeded the $\pm 0.01^\circ$ positioning accuracy while holding attitude. All three axes traversed the region of $\pm 0.01^\circ$ but none consistently held attitude within. The 1-axis maintained positioning accuracy within $\pm 0.10^\circ$, the 2-axis maintained positioning accuracy within $\pm 0.20^\circ$, and the 3-axis maintained positioning accuracy within $\pm 0.05^\circ$.

The reaction wheel ACS and the PID controller exceeded the 10 s threshold for the 10° and 30° rest-to-rest maneuvers. Settling time for the rest-to-rest maneuvers was defined as the time taken for the satellite to start from rest, perform the maneuver, and finish within $\pm 0.01^\circ$ of the desired angular position. The 10° maneuvers were performed in approximately 50 s. The positioning accuracy of the 1-axis maneuver resulted in a percent difference of 0.46%. The positioning accuracy of the 2-axis maneuver resulted in a percent difference of 0.15%. The 30° maneuver was performed in approximately 70 s. The positioning accuracy of the 3-axis maneuver resulted in a percent difference of 0.26%. Overall, proof of concept has been evaluated and confirmed positive. Sim-

Sat II consistently executed rest-to-rest maneuvers and demonstrated the maneuvers are comfortably performed within the angular velocity threshold of $180^\circ/\text{s}$.

In the position hold and rest-to-rest maneuver cases, position accuracy and settling time can readily be mitigated by adjusting the PID gain settings K_P , K_I , and K_D . Although beyond the scope of this research, numerical methods and experimental techniques can be investigated to optimally tune the PID controller. The PID gain settings used for this research demonstrated that the duration of time for SimSat II to go from 10% to 90% of its final value (rise time, t_r) in the rest-to-rest maneuvers was within the 10 s threshold.

While overcoming the worst case anticipated disturbance inputs, it can be seen that as the applied disturbance torque increases, the reaction wheel ACS has greater difficulty maintaining attitude. Additionally, the reaction wheel ACS has greater difficulty maintaining attitude for the axes with greater MOI values. For SimSat II's MOI relationship of $C > A > B$, the 3-axis C has greater difficulty than the 1-axis A , and the 1-axis has greater difficulty than the 2-axis B as the applied torques increase.

The ability to apply a known torque is predicated on being able to fix one's time step Δt . The evaluation of the reaction wheel ACS to apply a known torque concluded that measured torque never equaled the predicted torque value. Great care was taken to fix the Δt time step and to assure that commands were impulsively submitted to the EPOS controllers. Further investigation showed that although Δt has seemingly been fixed at a value 100 ms, experimental data indicated that the time between impulse commands varied.

In conclusion, this thesis research advances AFIT's second-generation satellite simulator by documenting how to command angular position inputs to SimSat II using Maxon EPOS 70/10 controllers and the dSPACE inc. RTI CAN block set. Additionally, this document enhances understanding of Maxon and dSPACE literature pertaining to the application of CAN communications and the RTI can block set [27, 13]. Furthermore, this research identifies, partially resolves, and provides recommended follow-on efforts for deconflicting communications traffic on the CAN bus.

5.2 *Recommendations*

The crux in further development of SimSat II rests with fixing the time step Δt in which commands are issued and executed. Multiple options exist for investigating the problem. SIMULINK proficiency is one possibility.

SimSat II's present SIMULINK model issues commands triggered by separate pulse generators for each EPOS 70/10 controller. Consolidating the three pulse generators into one or developing a timing mechanism that triggers off of SIMULINK's master simulation clock are possible alternatives. Coupled to the pulse generators is a TDM timing scheme in which the EPOS 70/10 controllers are issued velocity commands in a serial manner. TDM can be replaced by a Kalman filter to better resolve signal conflicts on the CAN bus.

Developing and testing SimSat II's SIMULINK model in the RTI environment is greatly aided by phoning the dSPACE Help Desk. When speaking with call center technicians, invariably two questions are asked: "Do you have WebEx capability?," and "Do you possess a CANalyzer?" Having neither, it is recommended that AFIT equip SimSat II's ground station PC with internet access and CANalyzer software. WebEx is a CiscoTM systems web conferencing application which requires access to the internet. The SIMULINK model in question can then be shared with the dSPACE Help Desk technician allowing him or her to explore every facet of SimSat II's SIMULINK model. Vector InformatikTM produces a CANalyzer software application that aids in the development of CAN communications architecture. With a CANalyzer, one can know exactly what is being transmitted along the CAN bus.

The last recommended avenue for resolution of Δt is to contact dSPACE directly and inquire about any possible timing limitations of the dSPACE MicroAutoBox. There are several RTI CAN controller settings that issue a warning if changed. A configuration setting of sort could be all that is necessary to resolve the inconsistency of Δt .

Additional research topics include the optimization of SimSat II's PID controller. Numerical methods and experimental techniques can be investigated to adjust the PID gain settings K_P , K_I , and K_D such that pointing accuracy and settling time are achieved.

There is, however, a method to evaluate the performance of the reaction wheel ACS without using the PID controller. Using *current mode* within the EPOS User Interface, one can command torque inputs directly to the EPOS 70/10 controllers. In addition to the EPOS User Interface, an apparatus would need to be constructed to investigate pure spin about either the 1-, 2-, or 3-axis. Experimental disturbance torques could then be applied and compared to the torque commanded via current mode in the EPOS User Interface.

Another recommendation is that SimSat II's mass distribution be addressed. In SimSat II's current state, its POI is not equal to zero. The COM of each component should be located near to the axes of rotation at a height closer to the COR. New reaction wheel assemblies must be designed to lower the height of the reaction wheels' COM. Also, SimSat II's table top deck can be modified to incorporate cutouts where the reaction wheels could recess into the deck such that its axis of rotation is coplanar with the COR.

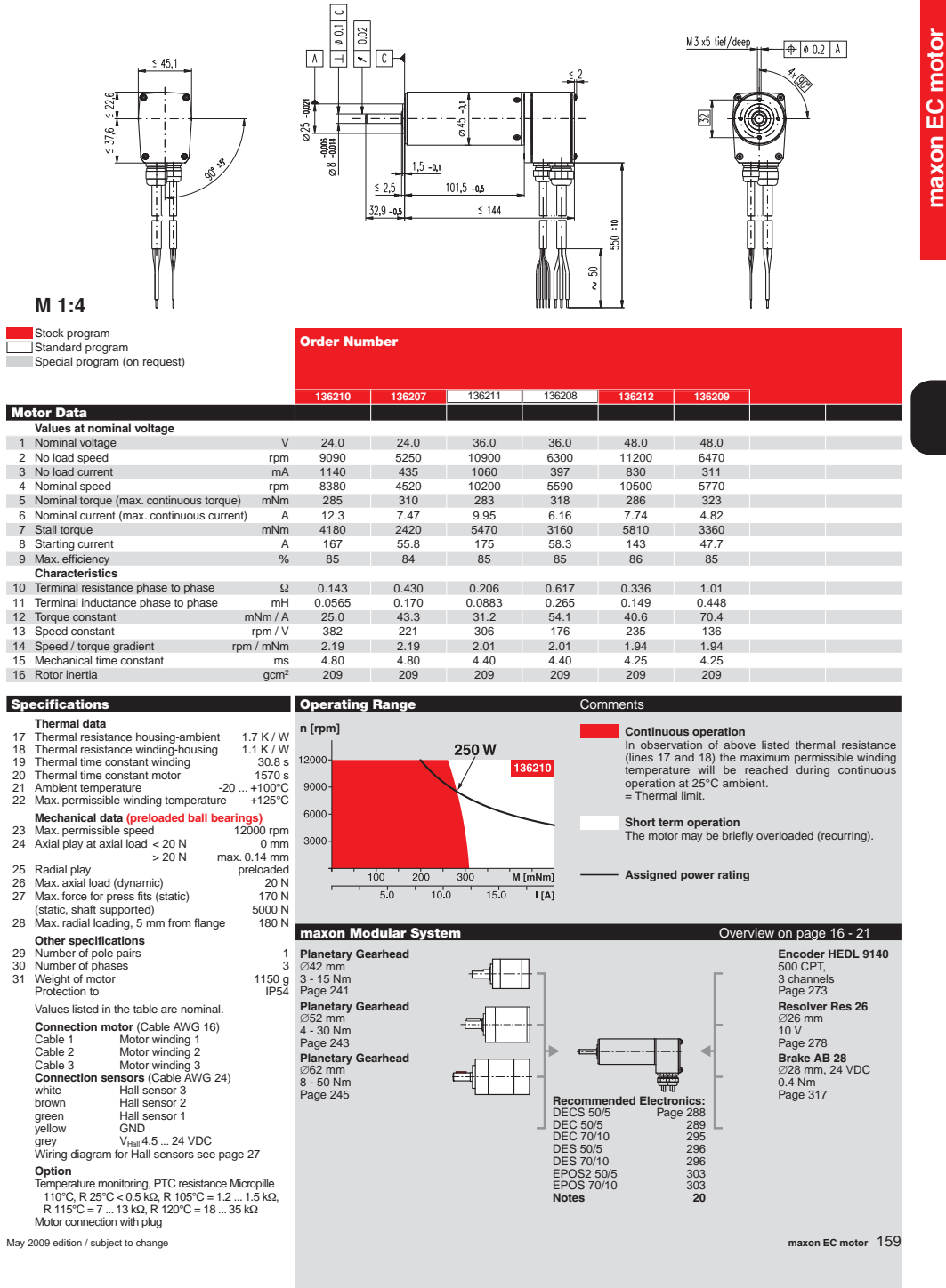
Lastly, future capabilities of SimSat II can be pondered. For example, momentum dumping can be demonstrated by coupling the reaction wheel ACS with the fan thruster ACS implemented by McFarland [33]. A SIMULINK algorithm can be developed to enact the fan thruster ACS when reaction wheel saturation is soon to occur. If SimSat II were equipped with a coupled reaction wheel and fan thruster ACS, the satellite would be capable of maintaining attitude control for longer durations of time and counteracting larger and longer lasting disturbance torques.

Appendices

Appendix A. SimSat II Subsystems

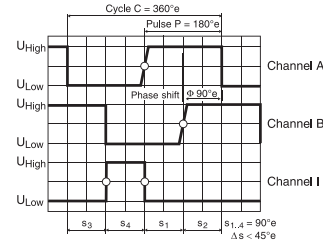
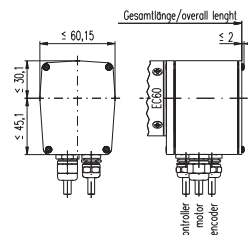
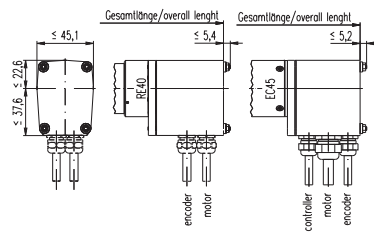
A.1 Reaction Wheel Assembly

EC 45 Ø45 mm, brushless, 250 Watt, CE approved



A.1.1 Maxon EC 45 Brushless Motor .

Encoder HEDL 9140, 500 CPT, 3 Channels, with Line Driver RS 422



maxon sensor

- ☒ Stock program
- ☐ Standard program
- ☐ Special program (on request)

Order Number

137959

Type

Counts per turn	500
Number of channels	3
Max. operating frequency (kHz)	100
Max. speed (rpm)	12000



maxon Modular System

+ Motor	Page	+ Gearhead	Page	+ Brake	Page	Overall length [mm] / • see Gearhead
RE 40, 150 W	82					125.1
RE 40, 150 W	82	GP 42, 3 - 15 Nm	240			•
RE 40, 150 W	82	GP 52, 4 - 30 Nm	243			•
RE 40, 150 W	82			AB 28	317	135.6
RE 40, 150 W	82	GP 42, 3 - 15 Nm	240	AB 28	317	•
RE 40, 150 W	82	GP 52, 4 - 30 Nm	243	AB 28	317	•
EC 45, 150 W	158					126.8
EC 45, 150 W	158	GP 42, 3 - 15 Nm	240			•
EC 45, 150 W	158	GP 52, 4 - 30 Nm	243			•
EC 45, 150 W	158			AB 28	317	135.6
EC 45, 150 W	158	GP 42, 3 - 15 Nm	240	AB 28	317	•
EC 45, 150 W	158	GP 52, 4 - 30 Nm	243	AB 28	317	•
EC 45, 250 W	159					159.6
EC 45, 250 W	159	GP 42, 3 - 15 Nm	241			•
EC 45, 250 W	159	GP 52, 4 - 30 Nm	243			•
EC 45, 250 W	159	GP 62, 8 - 50 Nm	245			•
EC 45, 250 W	159			AB 28	317	168.4
EC 45, 250 W	159	GP 42, 3 - 15 Nm	241	AB 28	317	•
EC 45, 250 W	159	GP 52, 4 - 30 Nm	243	AB 28	317	•
EC 45, 250 W	159	GP 62, 8 - 50 Nm	245	AB 28	317	•
EC 60, 400 W	162					177.3
EC 60, 400 W	162	GP 81, 20 - 120 Nm	246			•
EC 60, 400 W	162			AB 41	318	214.9
EC 60, 400 W	162	GP 81, 20 - 120 Nm	246	AB 41	318	•

Technical Data

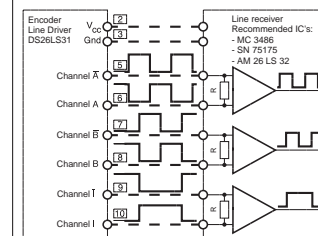
Supply voltage	5 V ± 10 %
Output signal	EIA Standard RS 422
driver used:	DS26LS31
Phase shift Φ	90°e ± 45°e
Signal rise time	180 ns
(typically, at $C_L = 25$ pF, $R_L = 11$ k Ω , 25°C)	
Signal fall time	40 ns
(typically, at $C_L = 25$ pF, $R_L = 11$ k Ω , 25°C)	
Index pulse width	90°e
Operating temperature range	0 ... +70°C
Operating temperature range optional	-40 ... +100°C
Moment of inertia of code wheel	≤ 0.6 gcm ²
Max. angular acceleration	250 000 rad s ⁻²
Output current per channel	min. -20 mA, max. 20 mA

The index signal I is synchronised with channel A or B.

Pin Allocation

Cable white	=	2	V _{CC} 5 VDC
Cable brown	=	3	GND
Cable green	=	5	Channel A
Cable yellow	=	6	Channel A
Cable grey	=	7	Channel B
Cable pink	=	8	Channel B
Cable blue	=	9	Channel I (Index)
Cable red	=	10	Channel I (Index)
Cable size 8 x 0.25 mm ²			

Connection example



Terminal resistance R = typical 100 Ω

maxon sensor 273

A.1.2 Maxon HEDL 9140 Encoder .

DIGITAL

CANopen

RS232

GUI

NEW



USB

EPOS2 24/5

Matched with DC brush motors with encoder or brushless EC motors with Hall sensors and encoder, from 5 to 120 watts.



USB

EPOS2 50/5

Matched with DC brush motors with encoder or brushless EC motors with Hall sensors and encoder, from 5 to 250 watts.

**EPOS 70/10**

Matched with DC brush motors with encoder or brushless EC motors with Hall sensors or encoder, from 80 to 700 watts.

maxon motor control

Controller versions		
Slave version	Slave version	Slave version
Electrical Data		
11 - 24 VDC	11 - 50 VDC	11 - 70 VDC
11 - 24 VDC	11 - 50 VDC	11 - 70 VDC
0.9 x V _{CC}	0.9 x V _{CC}	0.9 x V _{CC}
10 A	10 A	25 A
5 A	5 A	10 A
10 kHz	10 kHz	10 kHz
1 kHz	1 kHz	1 kHz
1 kHz	1 kHz	1 kHz
25 000 rpm (sinusoidal); 100 000 rpm (block)	25 000 rpm (sinusoidal); 100 000 rpm (block)	25 000 rpm
15 µH / 5 A	22 µH / 5 A	25 µH / 10 A
H1, H2, H3	H1, H2, H3	H1, H2, H3
A, A\, B, B\, I, I\ (max. 5 MHz)	A, A\, B, B\, I, I\ (max. 5 MHz)	A, A\, B, B\, I, I\ (max. 1 MHz)
6 digital inputs	12 digital inputs	8 digital inputs
2 analogue inputs	2 analogue inputs (differential)	2 analogue inputs
12-bit resolution, 0 ... +5 V	12-bit resolution, ±10 V	10-bit resolution, 0 ... +5 V
configurable with DIP switch 1 ... 7	configurable with DIP switch 1 ... 7	configurable with DIP switch 1 ... 7
4 digital outputs	5 digital outputs; 1 analogue 12-bit 0 ... 10 V	4 digital outputs
+5 VDC, max. 100 mA	+5 VDC, max. 100 mA	+5 VDC, max. 100 mA
+5 VDC, max. 30 mA	+5 VDC, max. 30 mA	+5 VDC, max. 30 mA
V _{CC} , max. 1300 mA	+5 VDC, max. 150 mA	+5 VDC (R _i = 1 kΩ)
RxD; TxD (max. 115 200 bit/s)	RxD; TxD (max. 115 200 bit/s)	RxD; TxD (max. 115 200 bit/s)
high; low (max. 1 Mbit/s)	high; low (max. 1 Mbit/s)	high; low (max. 1 Mbit/s)
Data+; Data- (max. 12 Mbit/s)	Data+; Data- (max. 12 Mbit/s)	
green LED, red LED	green LED, red LED	Bi-colour LED (green/red)
Ambient temperature / Humidity range		
-10 ... +45°C	-10 ... +45°C	-10 ... +45°C
-40 ... +85°C	-40 ... +85°C	-40 ... +85°C
20 ... 80 %	20 ... 80 %	20 ... 80 %
Mechanical data		
Approx. 170 g	Approx. 240 g	Approx. 330 g
105 x 83 x 24 mm	120 x 93.5 x 27 mm	150 x 93 x 27 mm
Flange for M3-screws	Flange for M3-screws	Flange for M3-screws
Order Number		
367676 EPOS2 24/5	347717 EPOS2 50/5	300583 EPOS 70/10

Accessories		
309687 DSR 50/5 Shunt regulator	309687 DSR 50/5 Shunt regulator	235811 DSR 70/30 Shunt regulator
Order accessories separately, see page 308	Order accessories separately, see page 308	Order accessories separately, see page 308

May 2009 edition / subject to change

maxon motor control 303

A.1.3 Maxon EPOS 70/10 Controller .

A.2 Northrop Grumman LN-200 IMU

NORTHROP GRUMMAN

Northrop Grumman is the world's leading producer of inertial navigation systems with more than 45,000 systems in use worldwide

LN-200 Fiber Optic Inertial Measurement Unit



Description

The LN-200 Inertial Measurement Unit (IMU) has been in high rate production since 1994. It is the latest in applied technology, utilizing state-of-art inertial fiber optic gyros and micro-machined accelerometers.

The LN-200 IMU is produced in a fully complemented and highly robotic production facility.

Applications

The LN-200 IMU has a wide variety of applications. Customers have purchased these products for space stabilization, missile guidance, Radar/EO/FLIR stabilization, motion compensation, UUV/UAV guidance and control, camera/mapping, and as IMUs for higher order integrated systems.

The LN-200 is a versatile inertial unit that is suitable for a wide variety of applications:

- Space Stabilization
- Camera/Mapping

- AHRS
- Motion Compensation
- EO/FLIR Stabilization
- Navigation
- Flight Controls
- ACMI/TSPI*

Advantages

The LN-200 is hermetically sealed and contains no moving parts or gaseous cavities, ensuring long, reliable shelf and usage life.

Northrop Grumman is the world's leading producer of inertial navigation systems with more than 45,000 systems in use worldwide.

Functionality

The LN-200, having been applied to a wide variety of applications, is available in a number of functional and data rate configurations.

* Air Combat Maneuvering Instrumentation/
Time, Space, Position Instrumentation

LN-200

Fiber Optic Inertial Measurement Unit



LN-200 Features

- 3 solid-state fiber optic gyros
- 3 solid-state silicon accelerometers
- Miniature package <35 cu in. (88.9 cu cm)
- Lightweight package <2 lb (907.2g)

Heritage

LN-200 is on the following platforms:

- Clementine
- Satellites
- AGM-142
- Air Combat Maneuvering Instrumentation Pods
- BQM-74E
- GMLRS ATD
- LANTIRN
- Predator
- Global Hawk
- MK-48
- AMRAAM
- Stingray
- CH-46
- MB-339
- Radar – MoComp
- RAH-66

LN-200 Core IMU

Physical Characteristics

Weight	<1.65 lb (750g)
Size	3.5 D x 3.35 H in. (plus connector) (8.89 D x 8.51 H cm)
Power	12W steady-state (nominal)
Cooling	Conduction to mounting plate

Performance—Accelerometer

Bias Repeatability	300 µg to 3.0 milli-g, 1σ
Scale Factor Accuracy	300 to 5,000 ppm, 1σ

Performance—Gyro

Bias Repeatability	1°/hr to 10°/hr, 1σ
Scale Factor Accuracy	100 to 500 ppm, 1σ
Random Walk	0.07 to 0.15°/sq rt hr Power Spectral Density (PSD) level

Operating Range

Angular Rate	Up to ±11,459°/sec
Angular Acceleration	±100,000°/sec/sec
Acceleration	>70g
Angular Attitude	Unlimited

MTBF

>20,000 hr	
------------	--

Input/Output

RS-485 serial data bus (SDLC)	
----------------------------------	--

Environmental

Temperature	-54°C to +71°C continuous operation
Vibration	15g rms, 20-20,000 Hz @ PSD NTE 0.114g ² /Hz in any bandwidth
Shock	90g, 6 msec terminal sawtooth

For more information, please contact:

Northrop Grumman Corporation
Navigation Systems
21240 Burbank Boulevard
Woodland Hills, CA 91367 USA
Phone: 1-866-NGNAVSY (646-2879)
www.nsd.es.northropgrumman.com

22939/02-06/2000/Crawford

Appendix B. Experimental Data

B.1 Positioning Accuracy

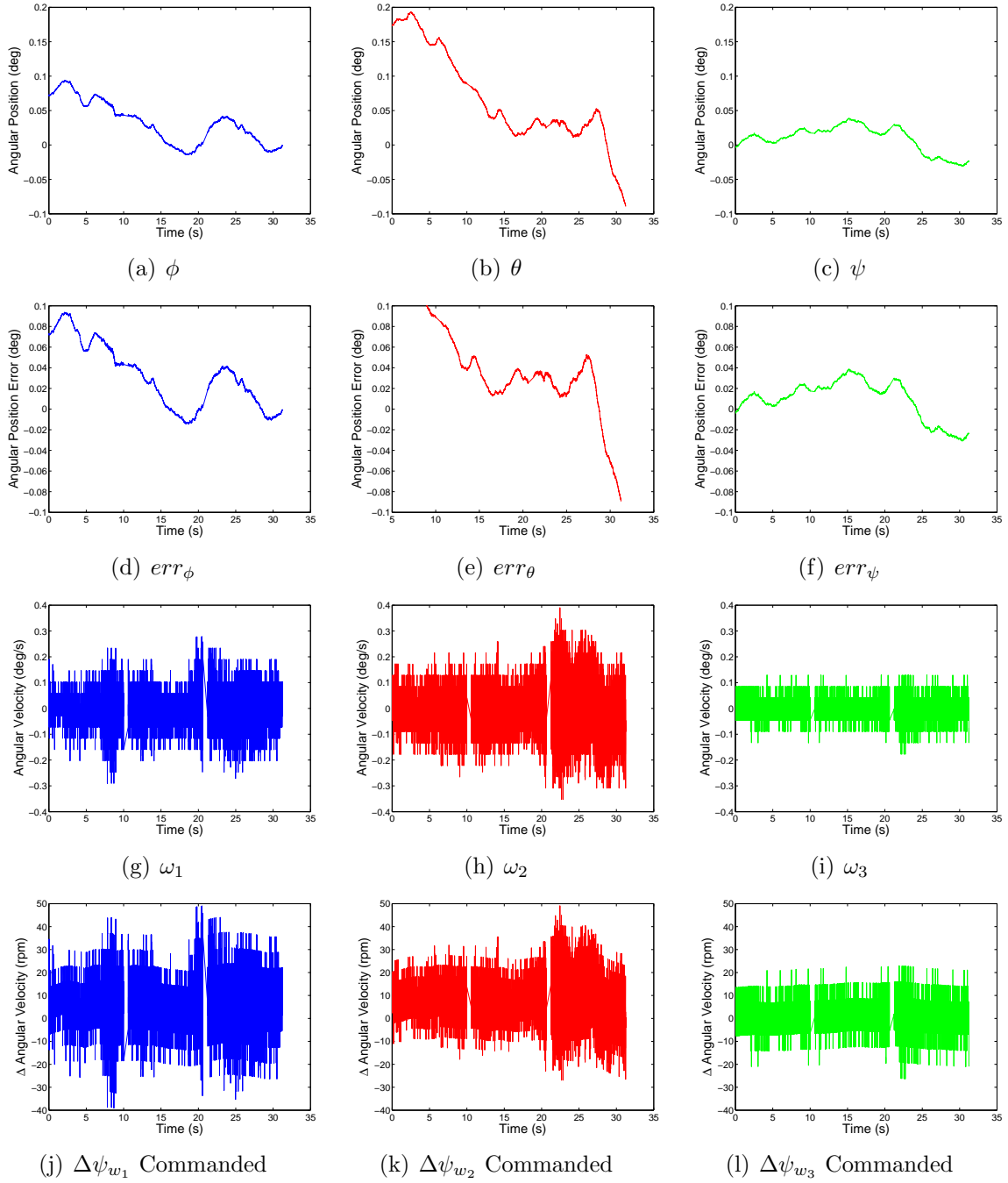


Figure B.1: Attitude Hold (1 of 2)

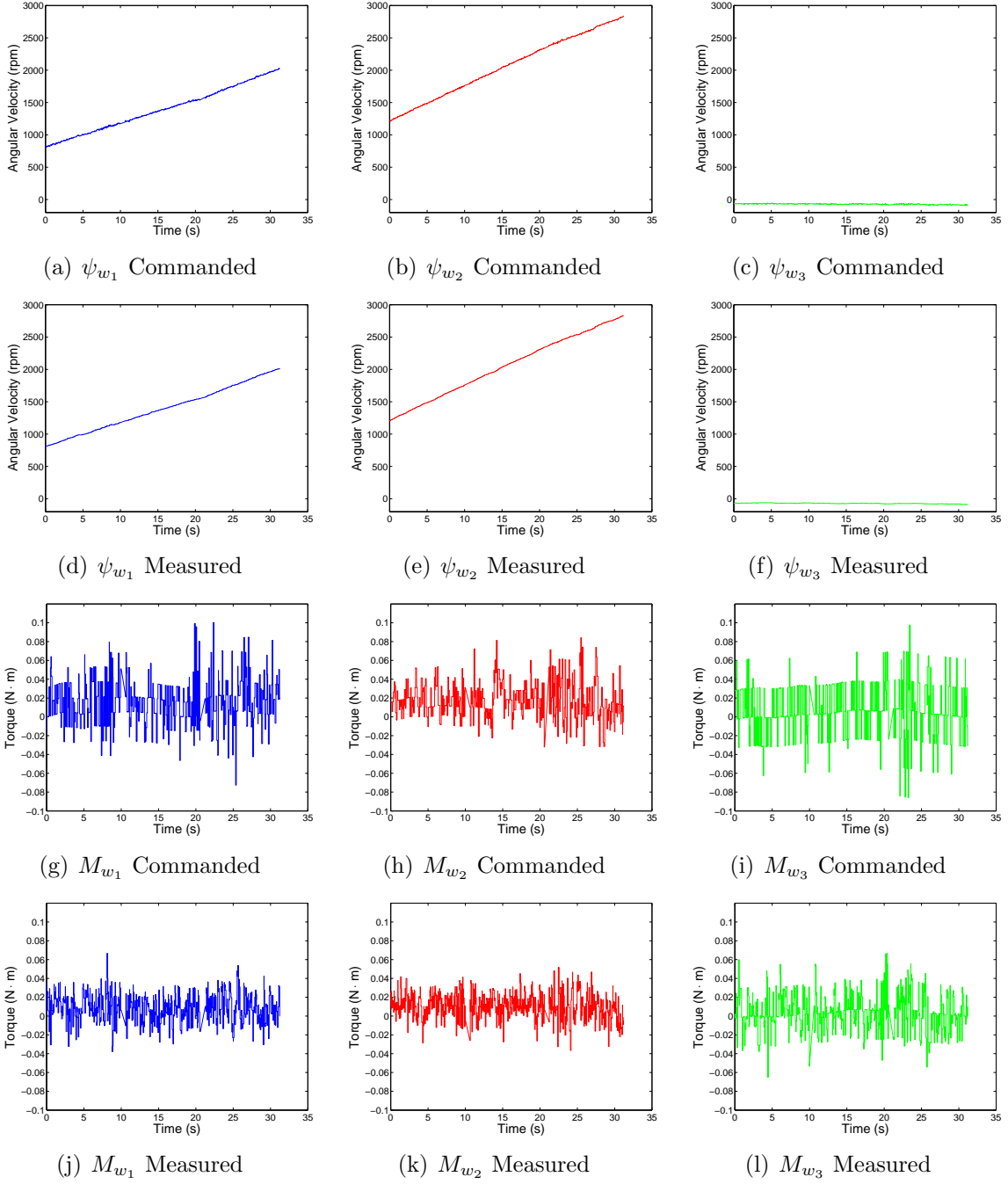


Figure B.2: Attitude Hold (2 of 2)

B.2 Rest-to-Rest Maneuvers

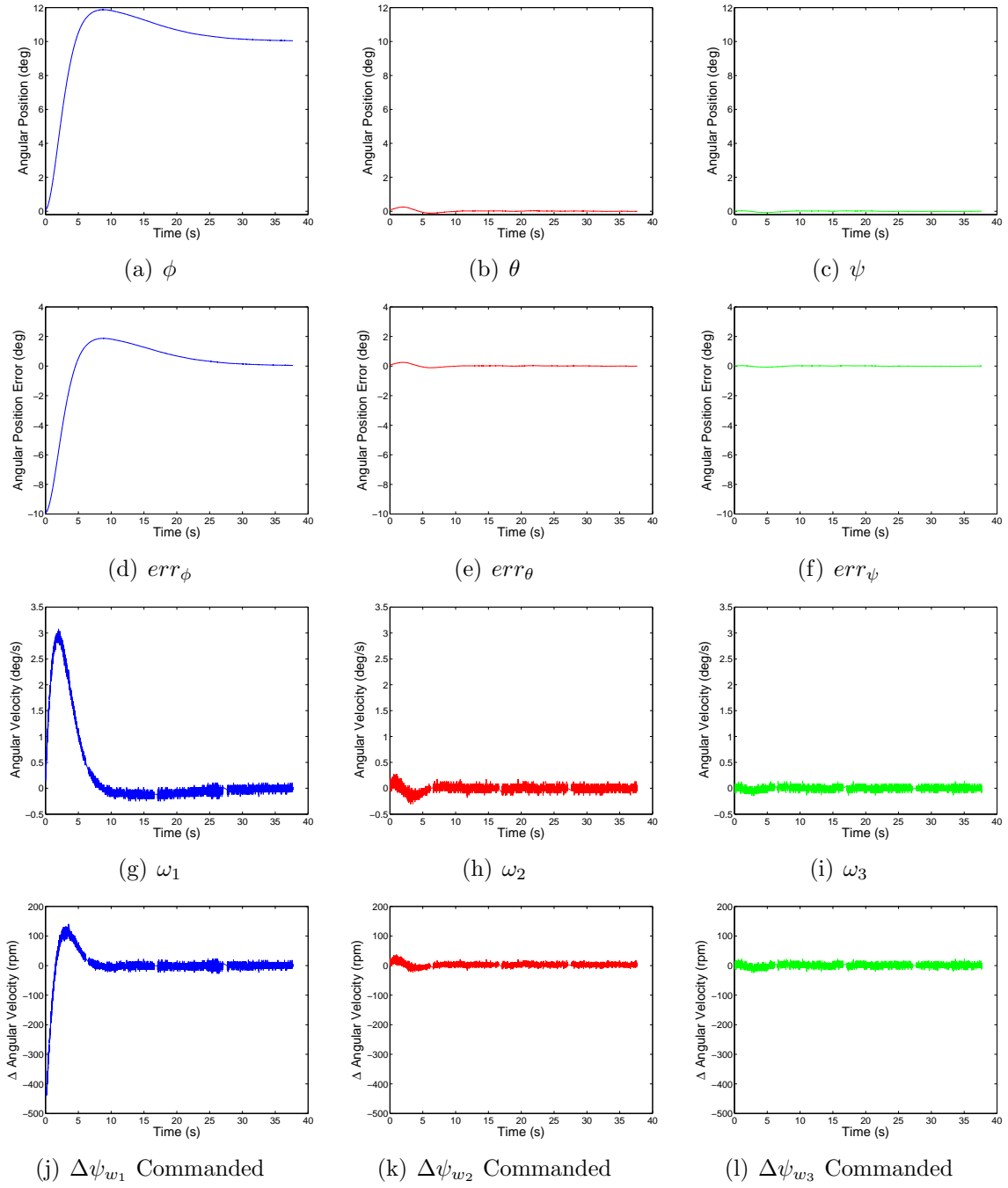


Figure B.3: Positive 10° Rest-to-Rest Maneuver about 1-Axis (1 of 2)

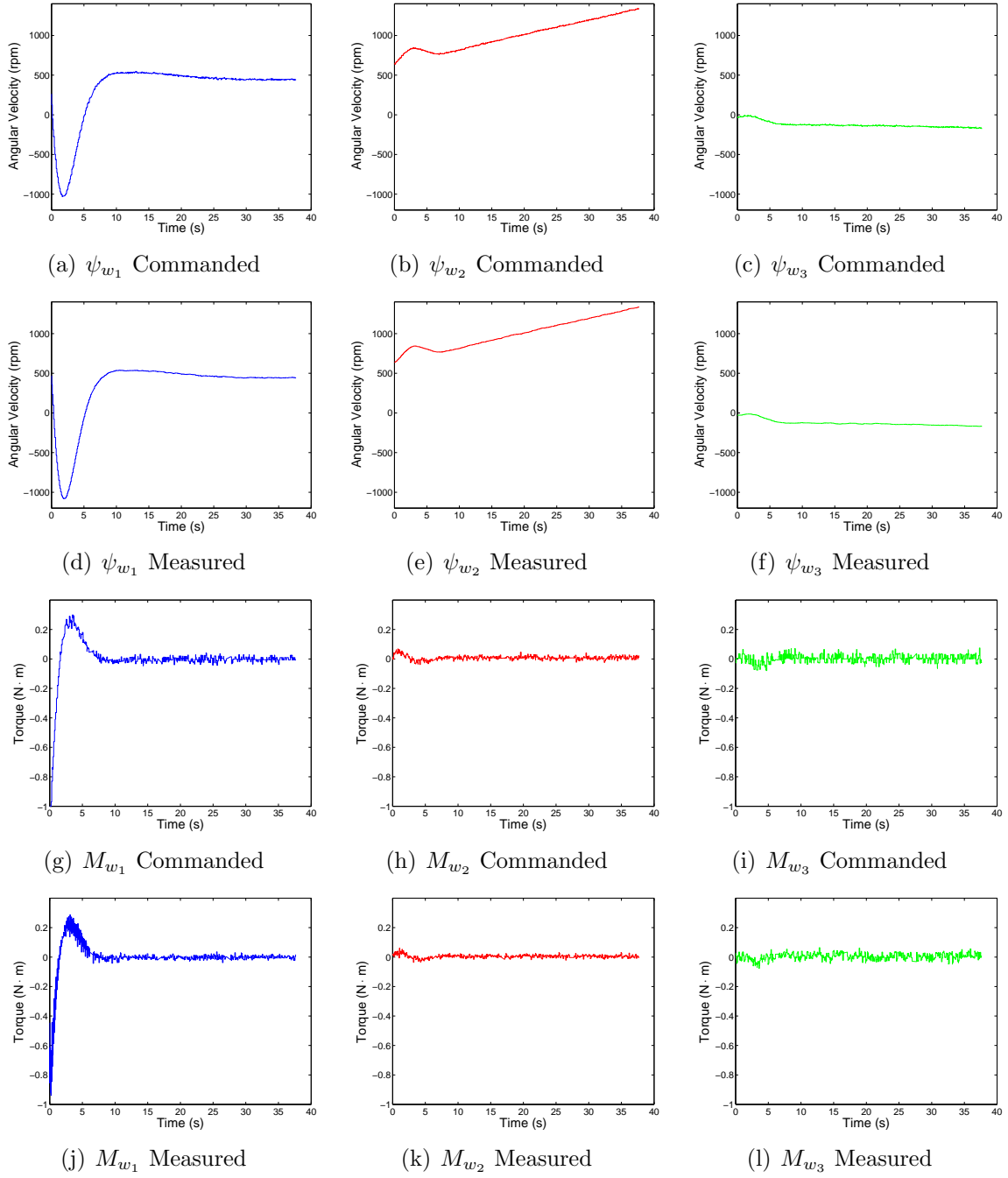


Figure B.4: Positive 10° Rest-to-Rest Maneuver about 1-Axis (2 of 2)

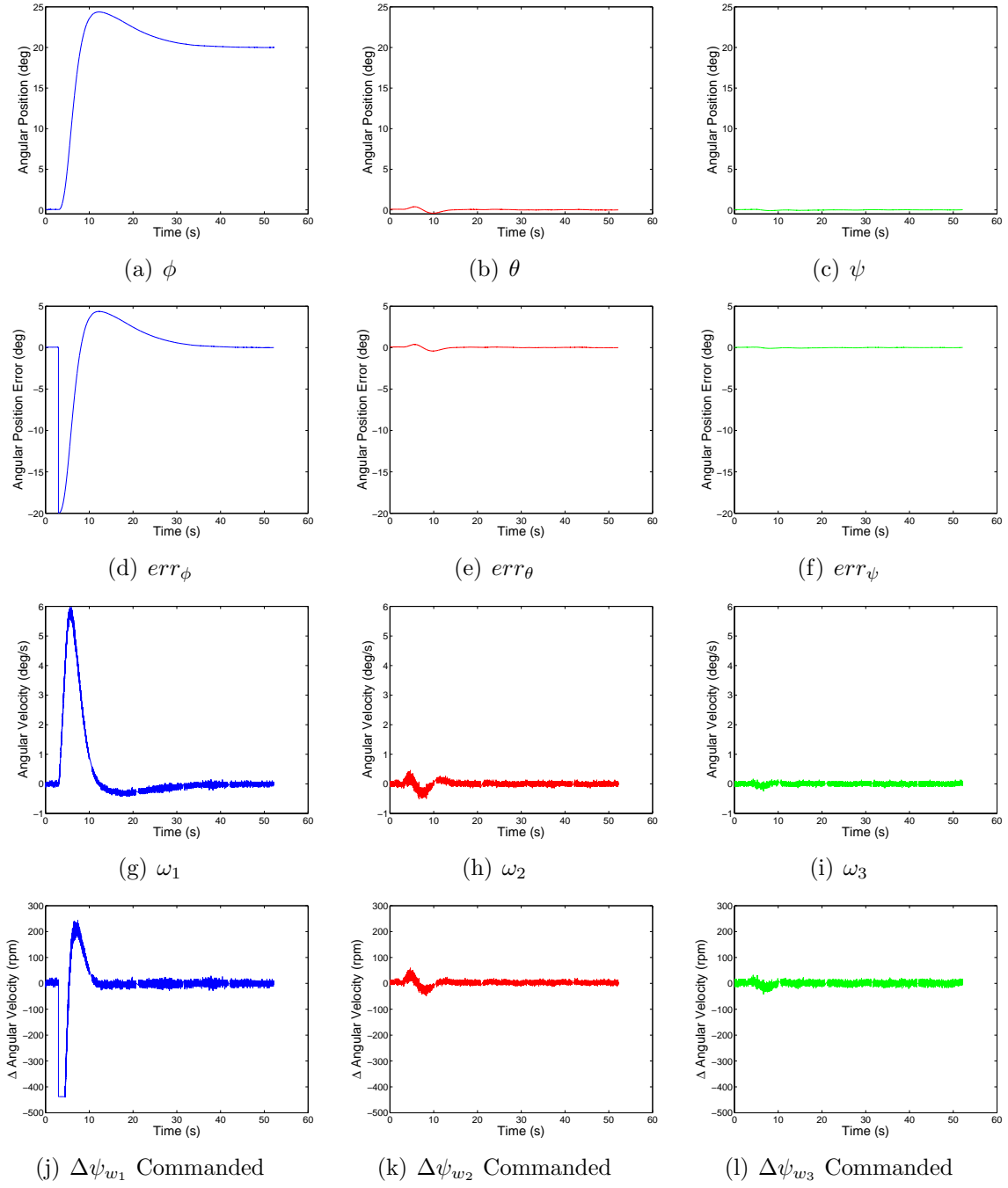


Figure B.5: Positive 20° Rest-to-Rest Maneuver about 1-Axis (1 of 2)

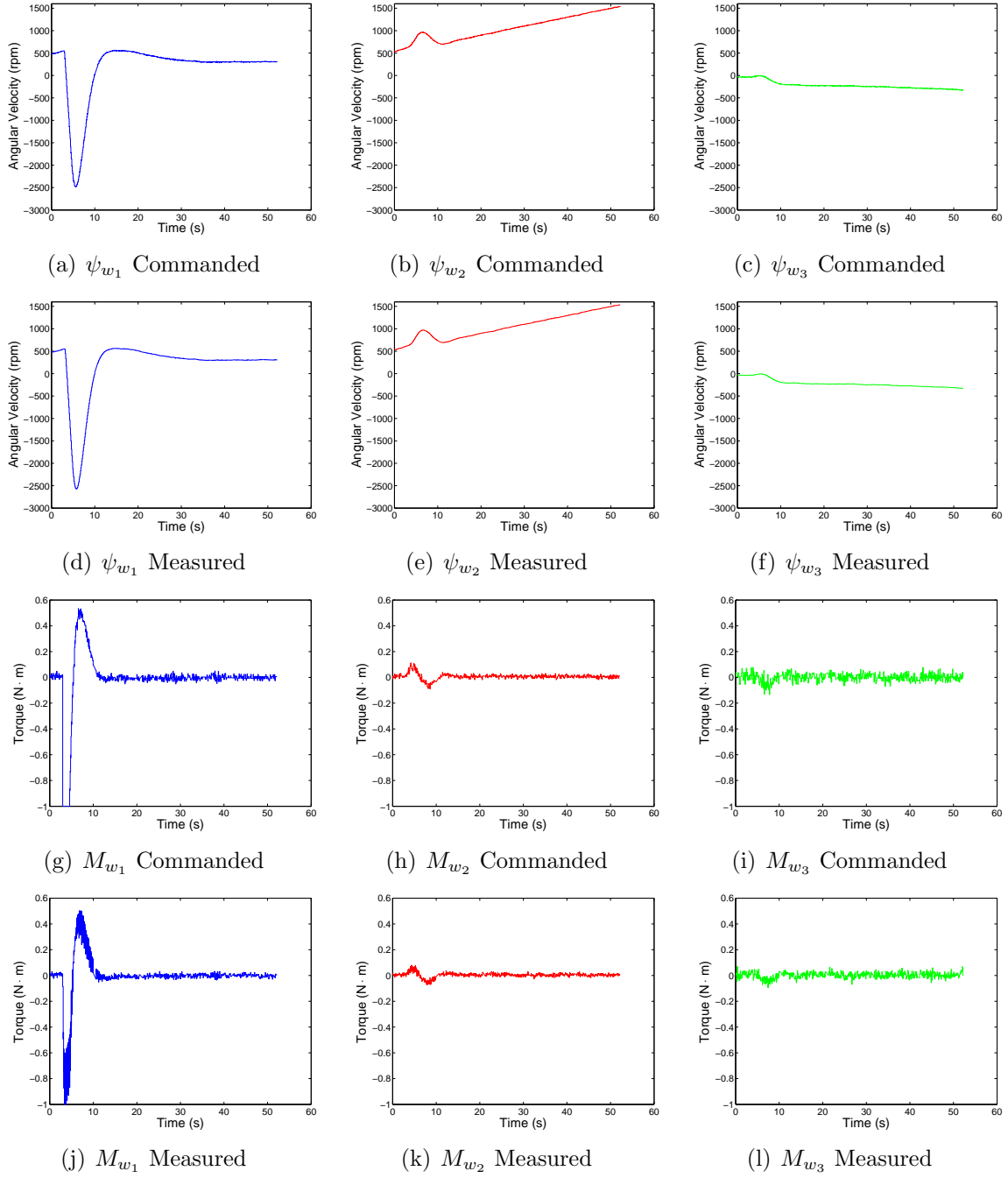


Figure B.6: Positive 20° Rest-to-Rest Maneuver about 1-Axis (2 of 2)

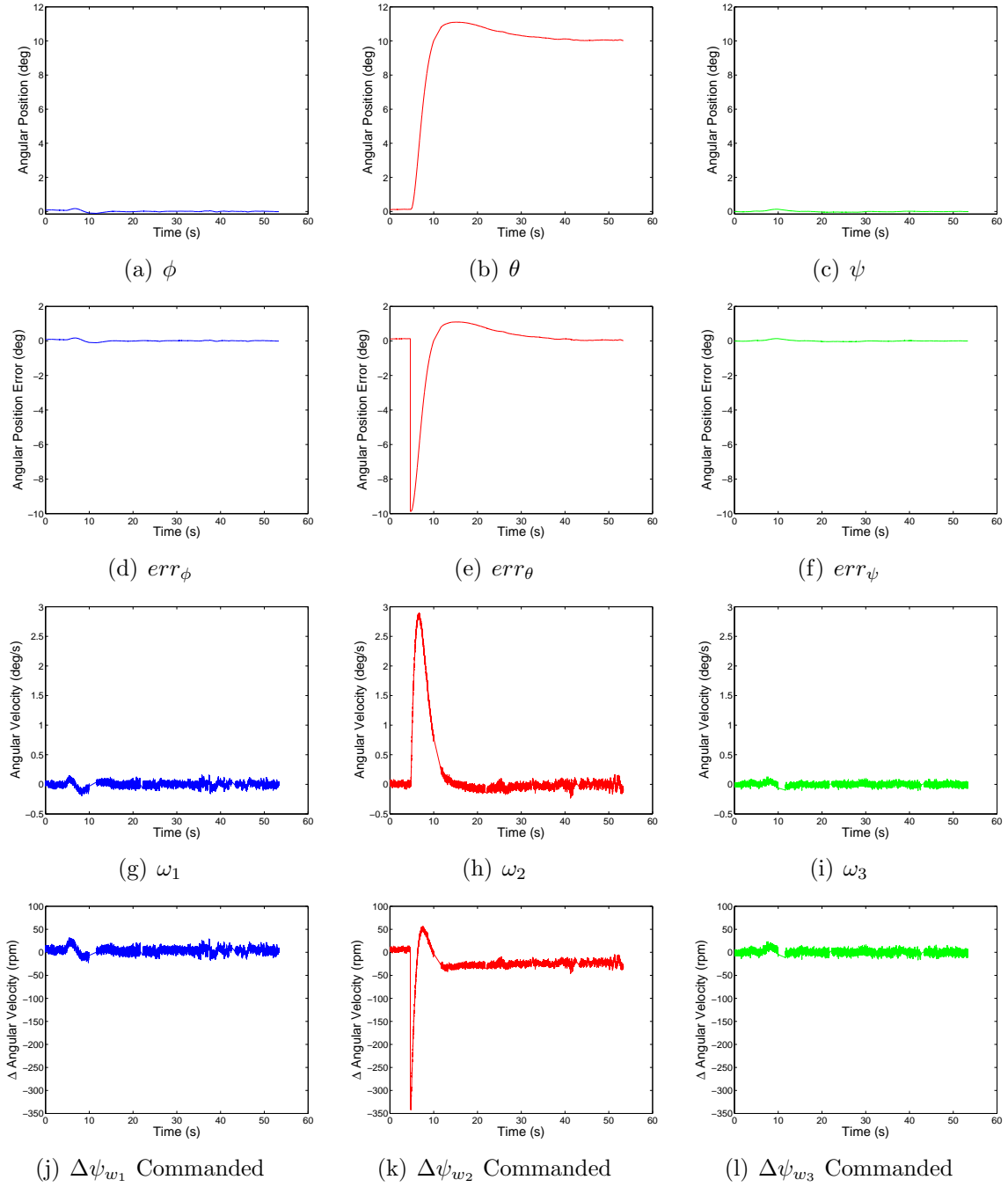


Figure B.7: Positive 10° Rest-to-Rest Maneuver about 2-Axis (1 of 2)

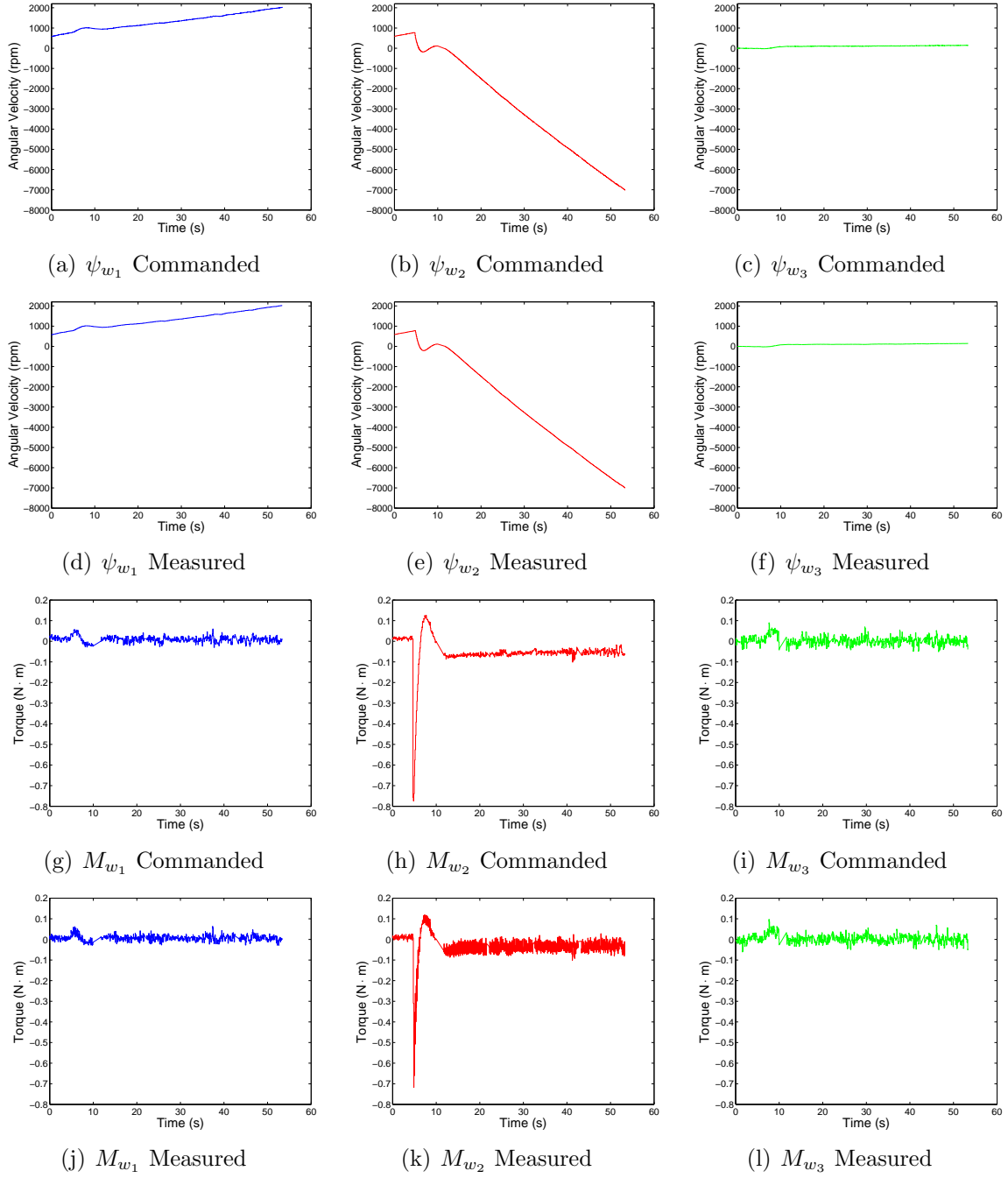


Figure B.8: Positive 10° Rest-to-Rest Maneuver about 2-Axis (2 of 2)

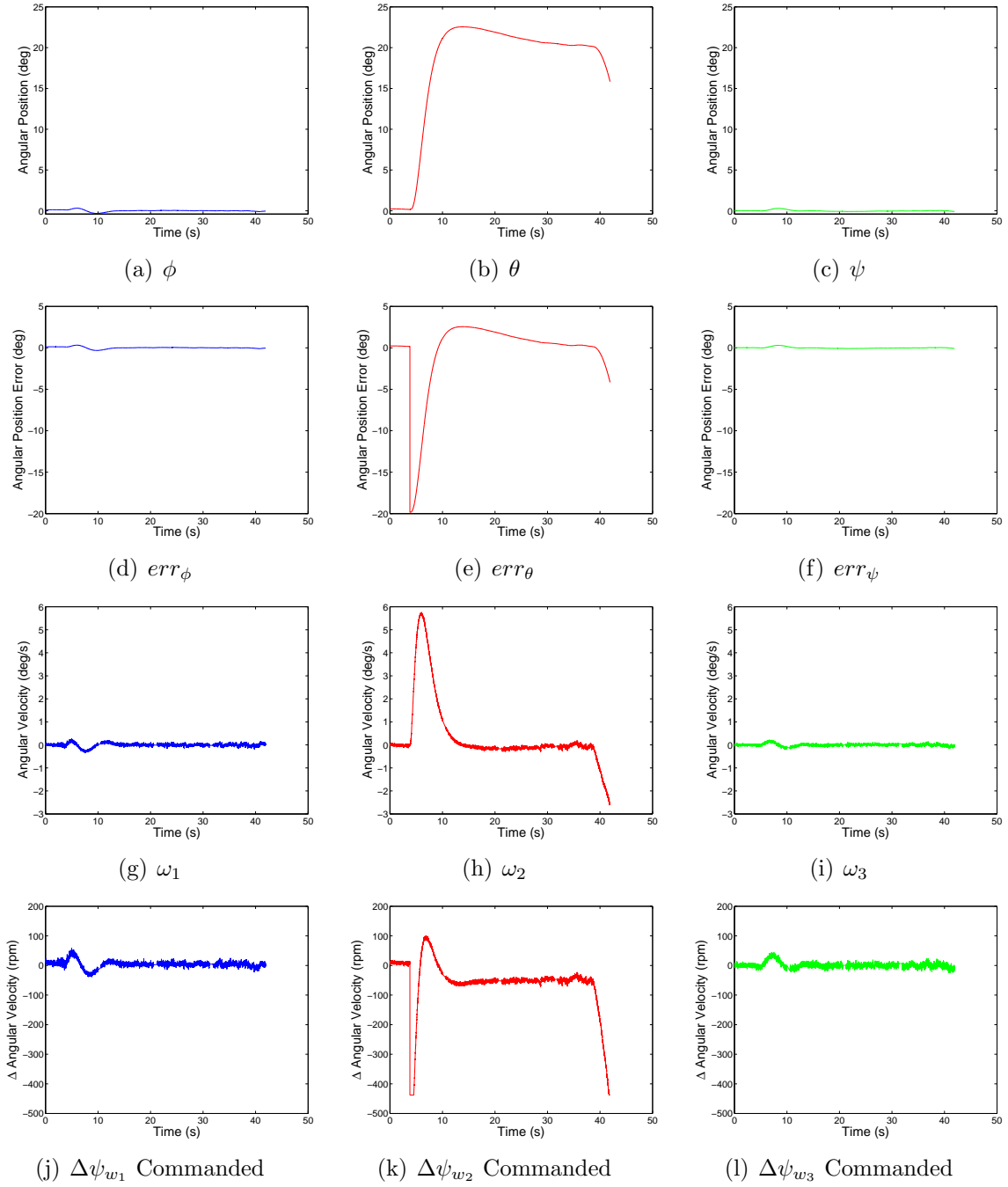


Figure B.9: Positive 20° Rest-to-Rest Maneuver about 2-Axis (1 of 2)

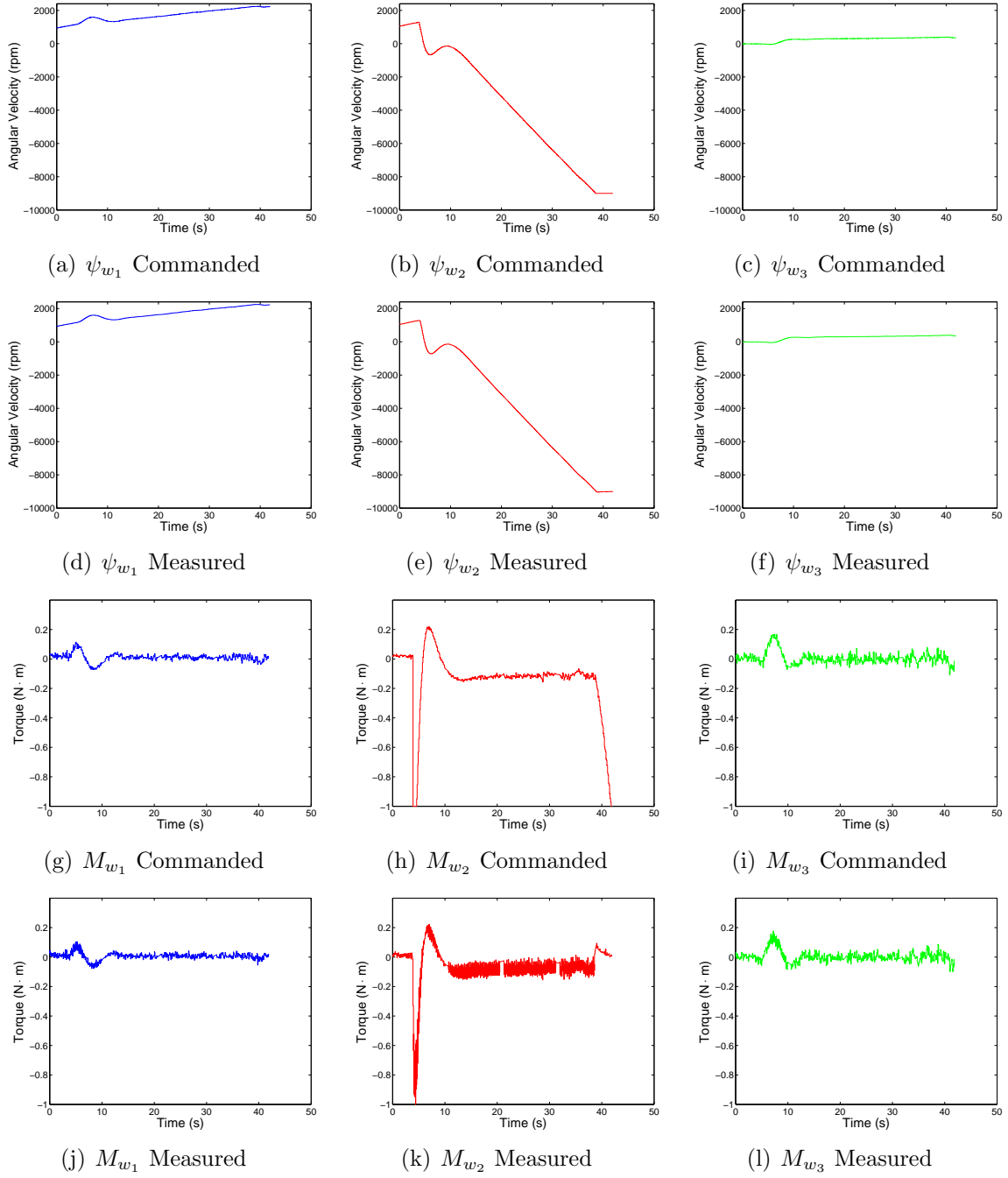


Figure B.10: Positive 20° Rest-to-Rest Maneuver about 2-Axis (2 of 2)

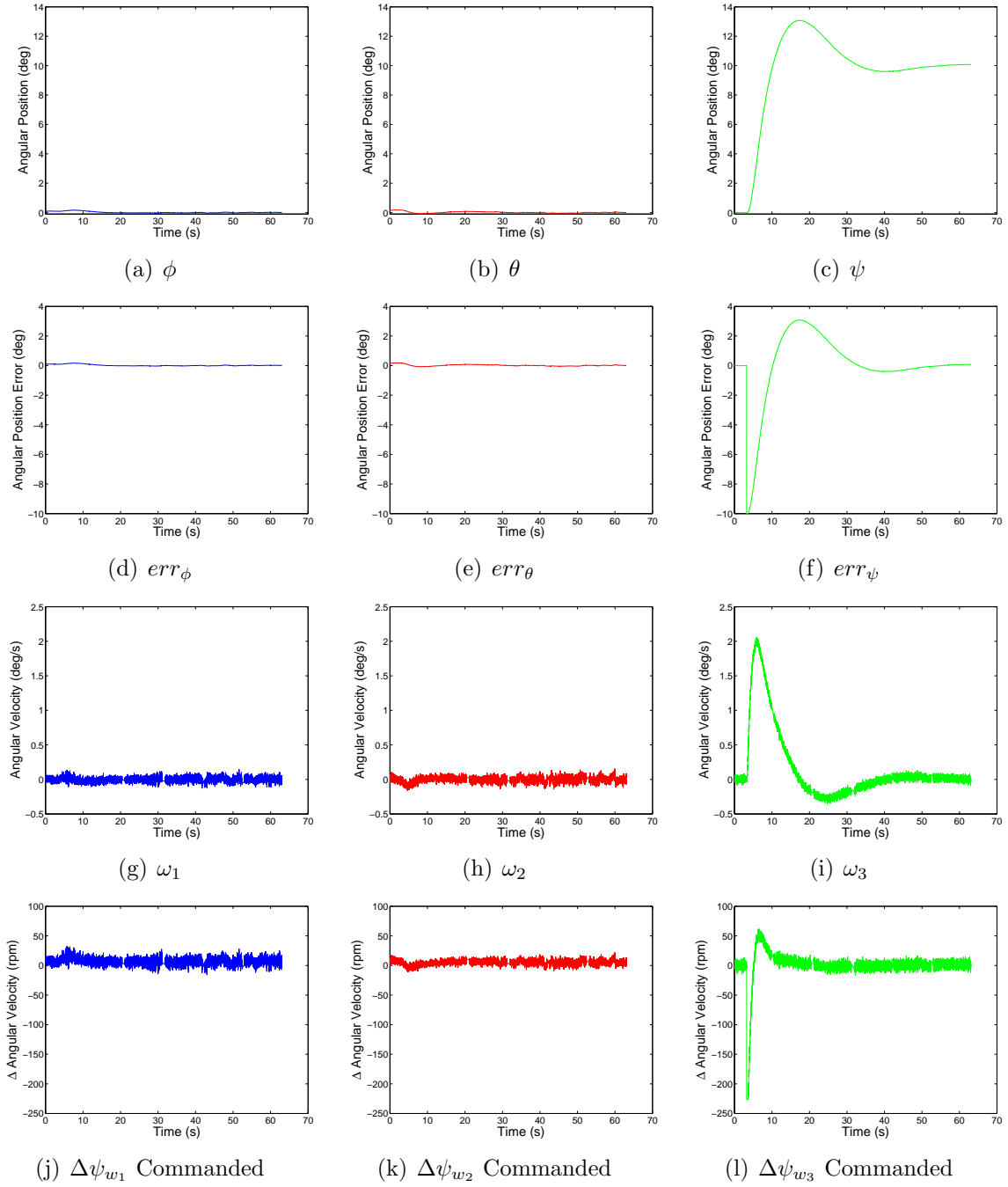


Figure B.11: Positive 10° Rest-to-Rest Maneuver about 3-Axis (1 of 2)

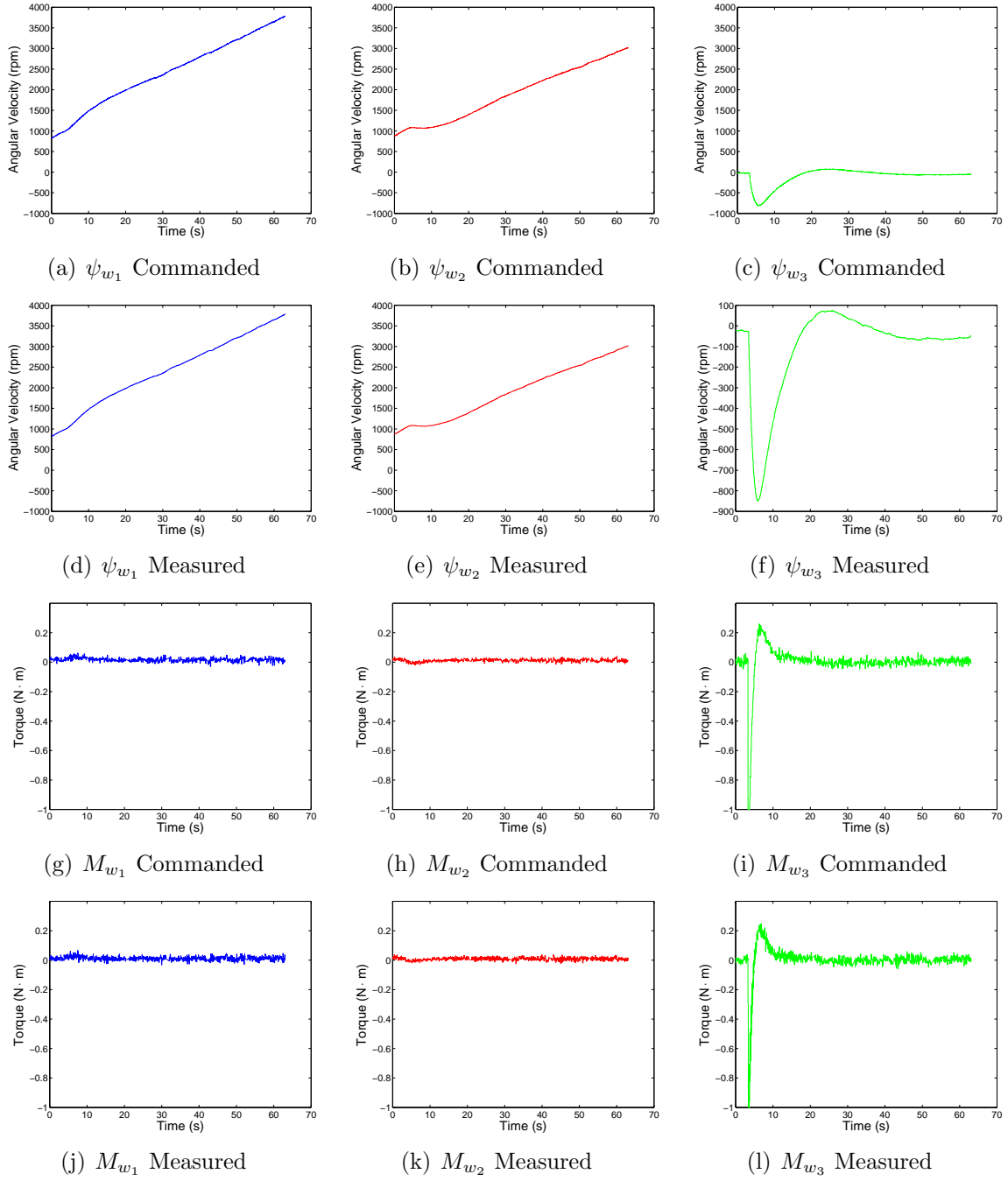


Figure B.12: Positive 10° Rest-to-Rest Maneuver about 3-Axis (2 of 2)

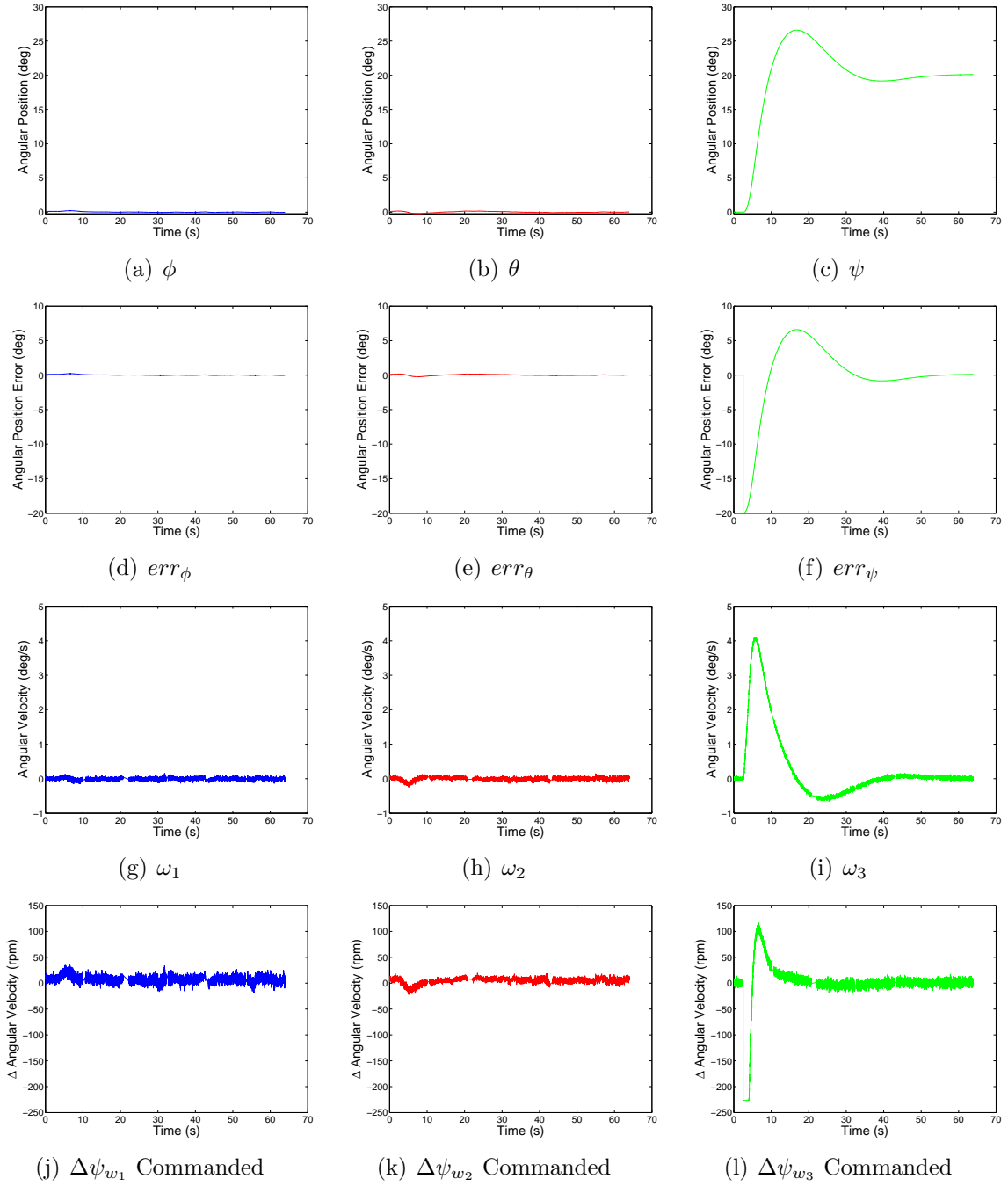


Figure B.13: Positive 20° Rest-to-Rest Maneuver about 3-Axis (1 of 2)

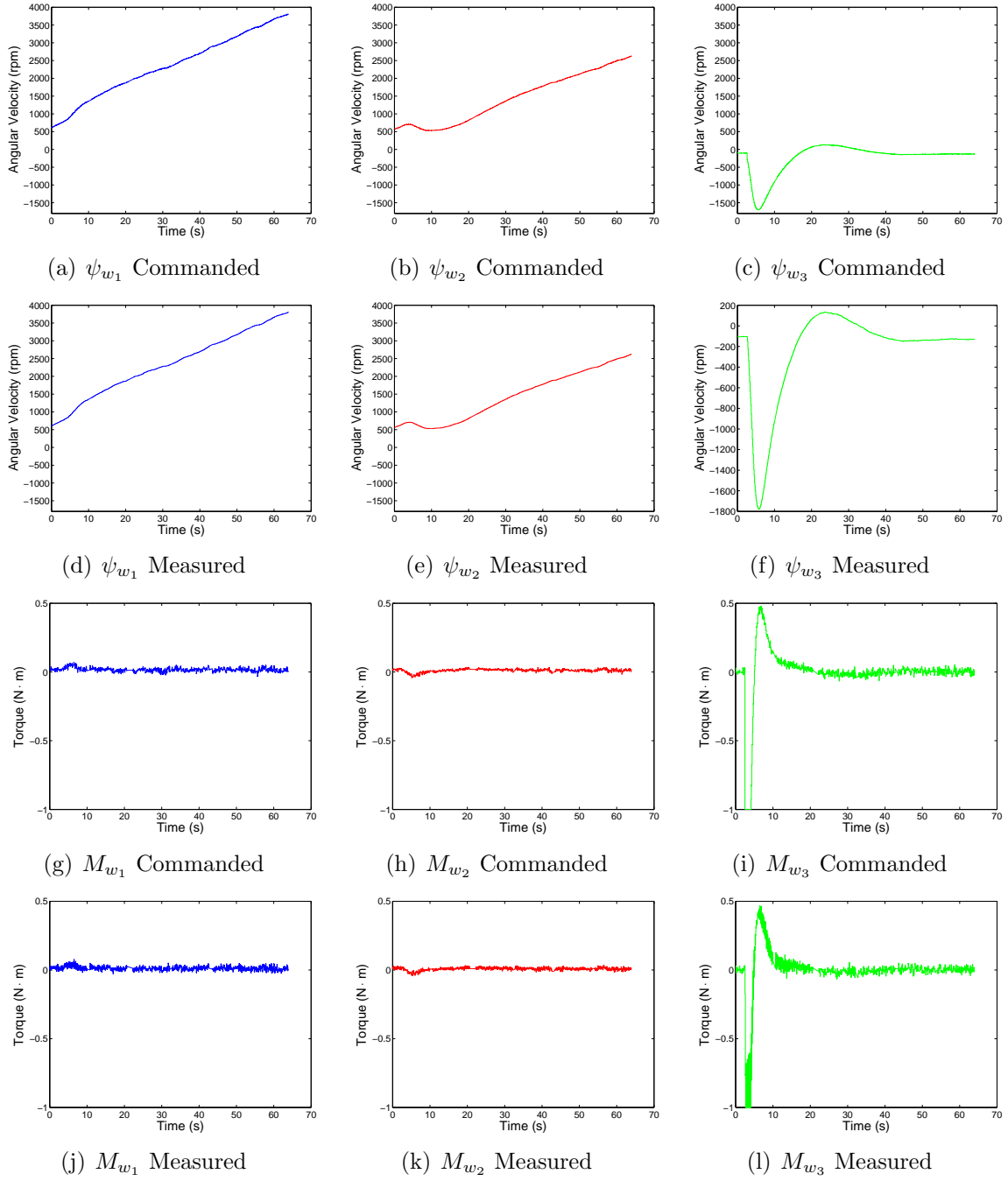


Figure B.14: Positive 20° Rest-to-Rest Maneuver about 3-Axis (2 of 2)

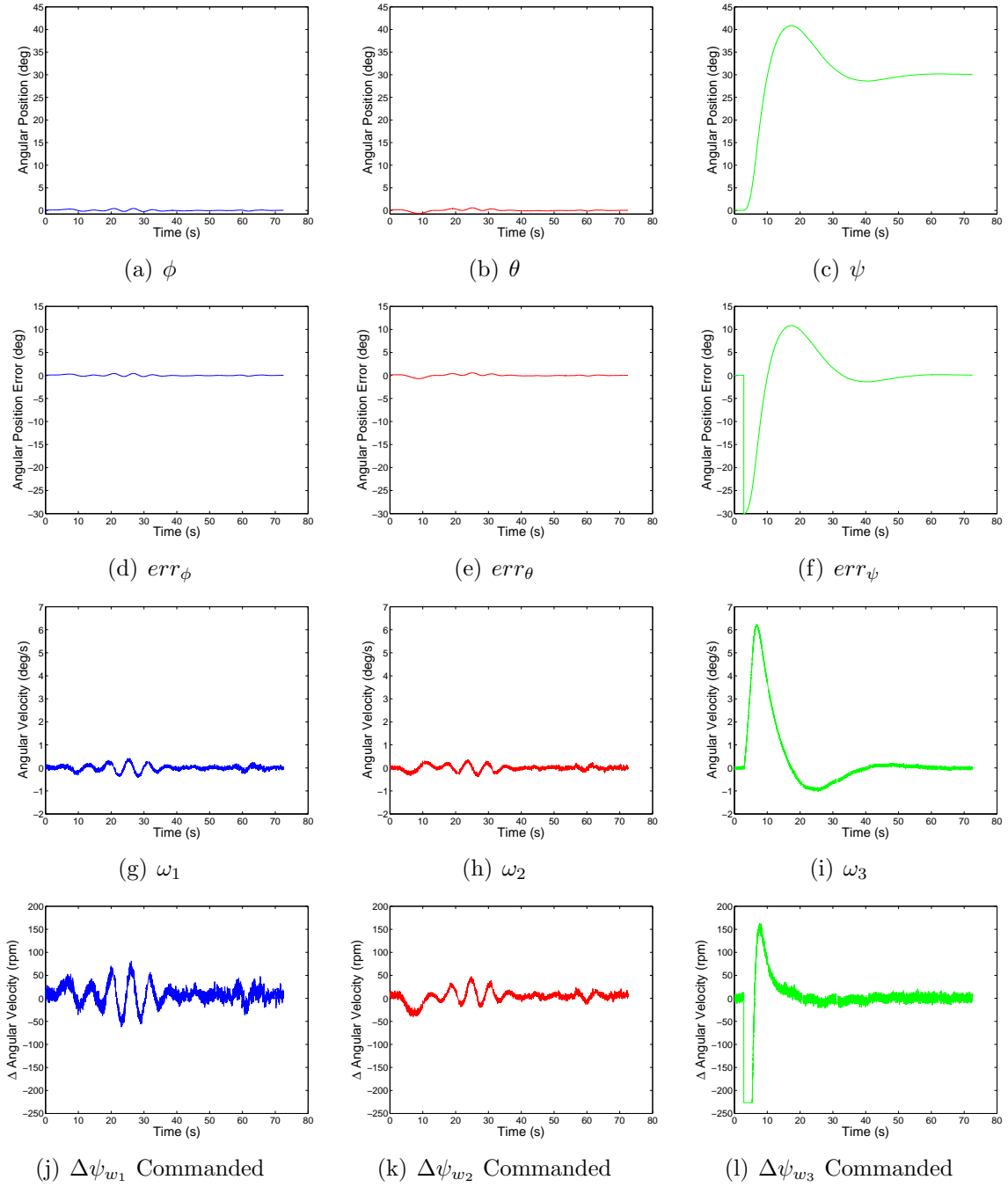


Figure B.15: Positive 30° Rest-to-Rest Maneuver about 3-Axis (1 of 2)

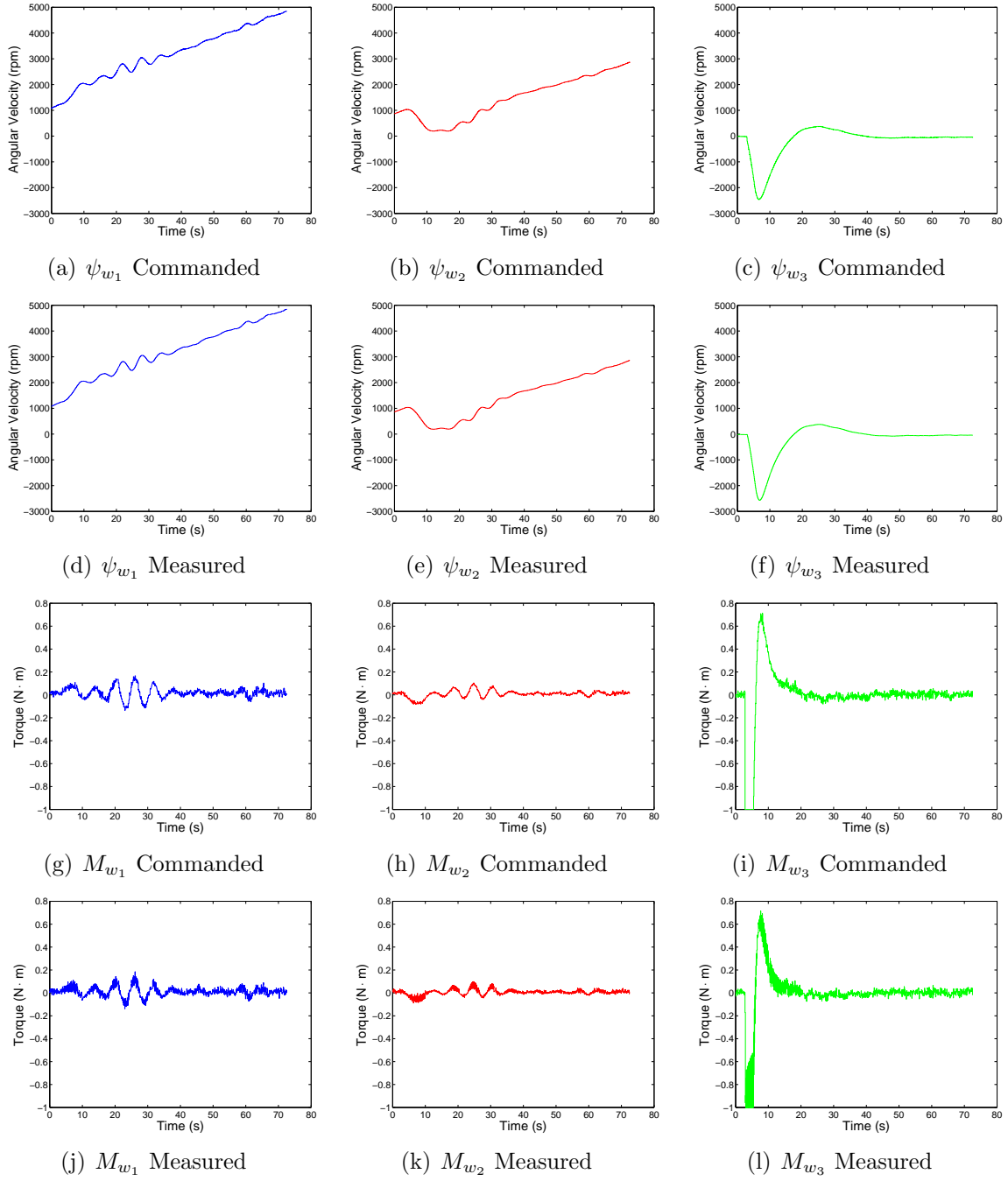


Figure B.16: Positive 30° Rest-to-Rest Maneuver about 3-Axis (2 of 2)

B.3 Disturbance Torques

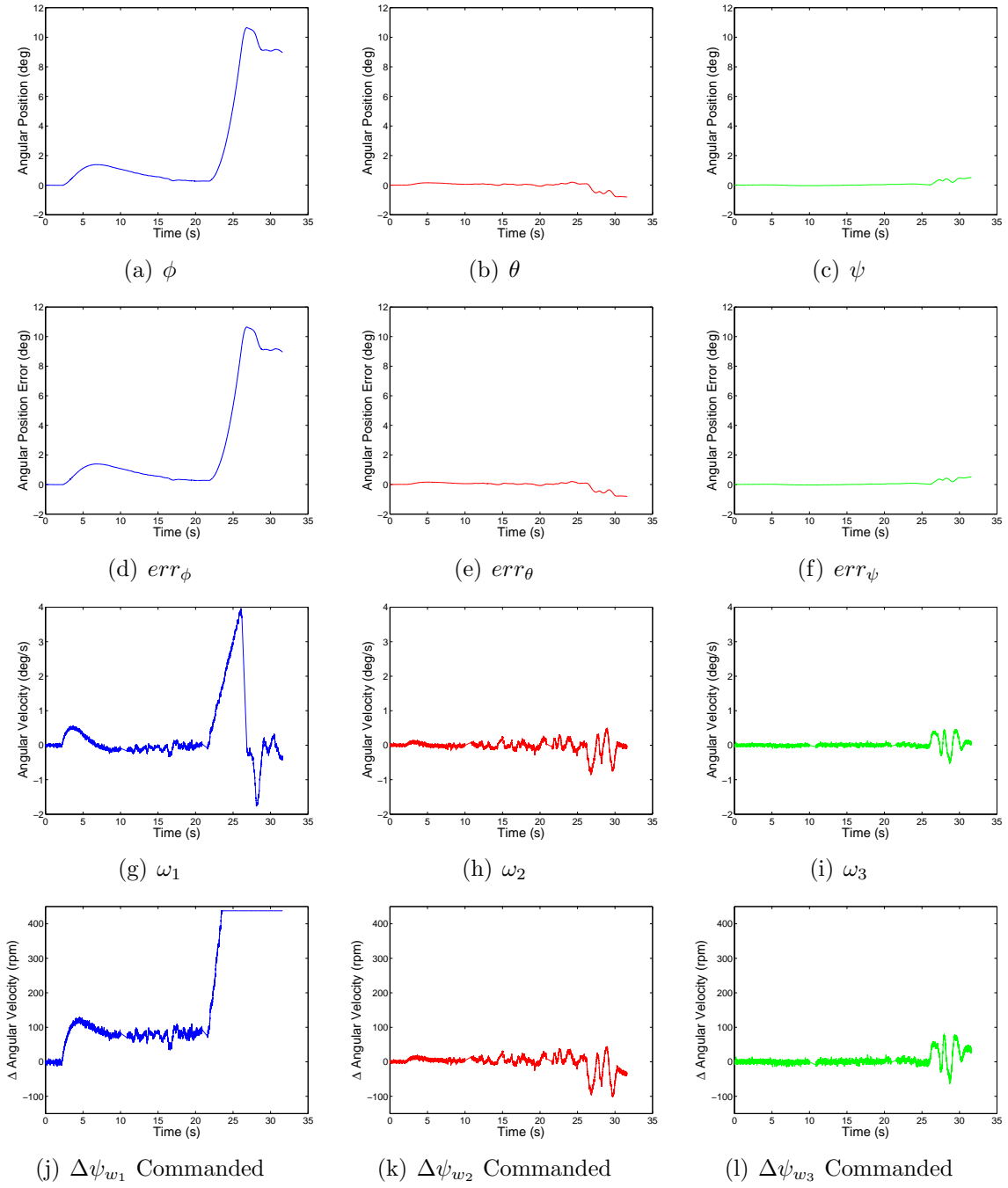


Figure B.17: Positive Torque about 1-Axis Using 20 g Mass (1 of 2)

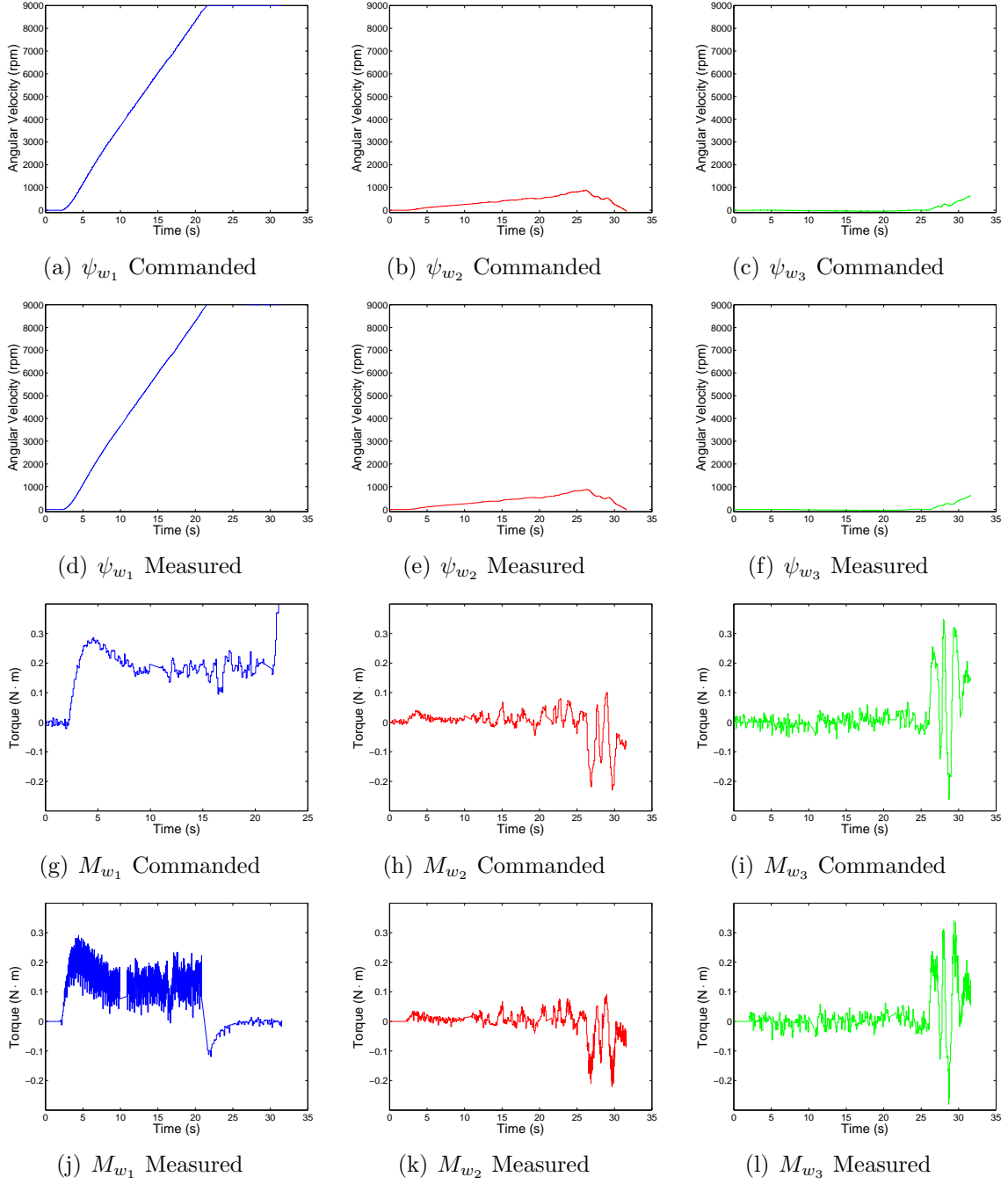


Figure B.18: Positive Torque about 1-Axis Using 20 g Mass (2 of 2)

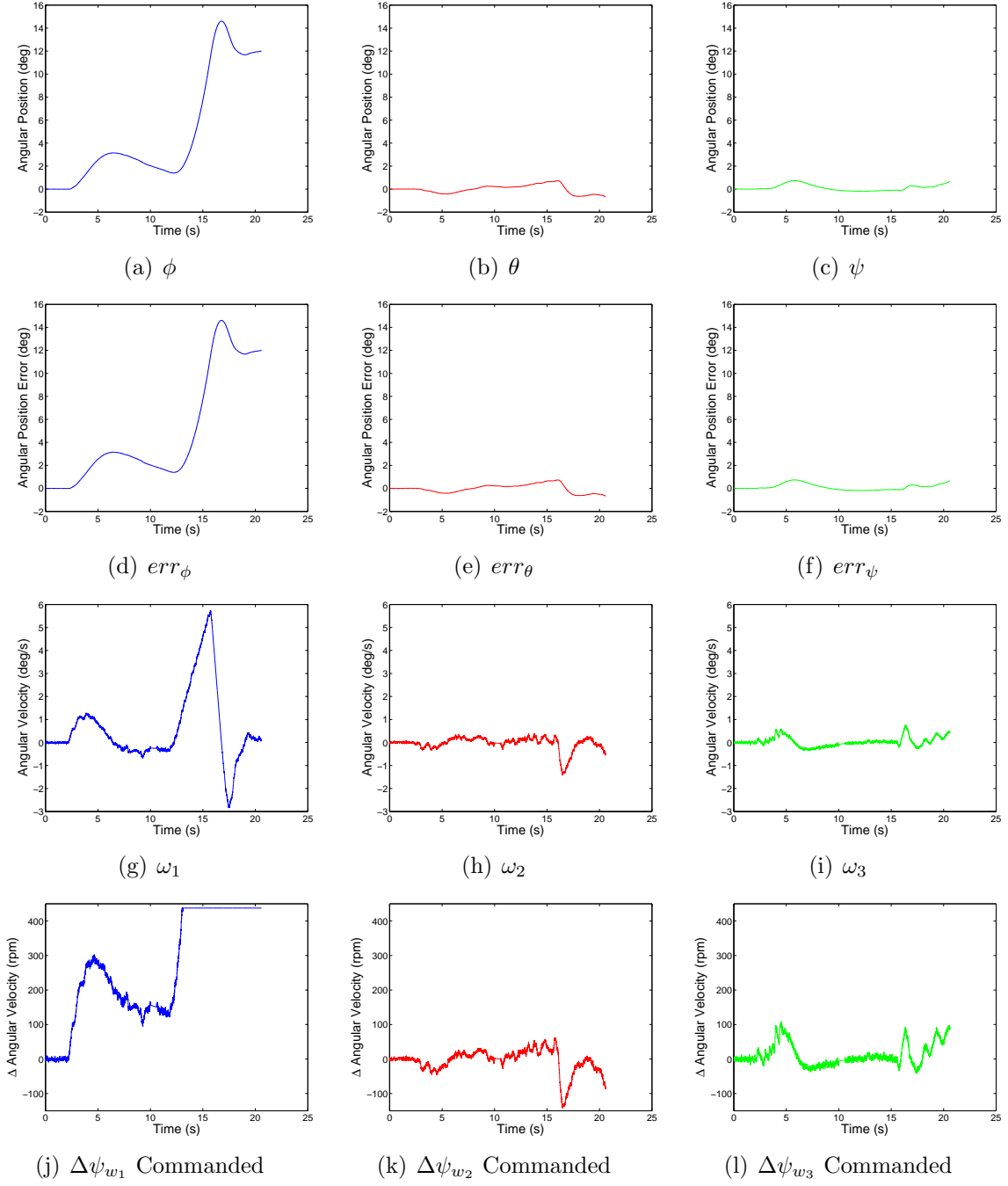


Figure B.19: Positive Torque about 1-Axis Using 40 g Mass (1 of 2)

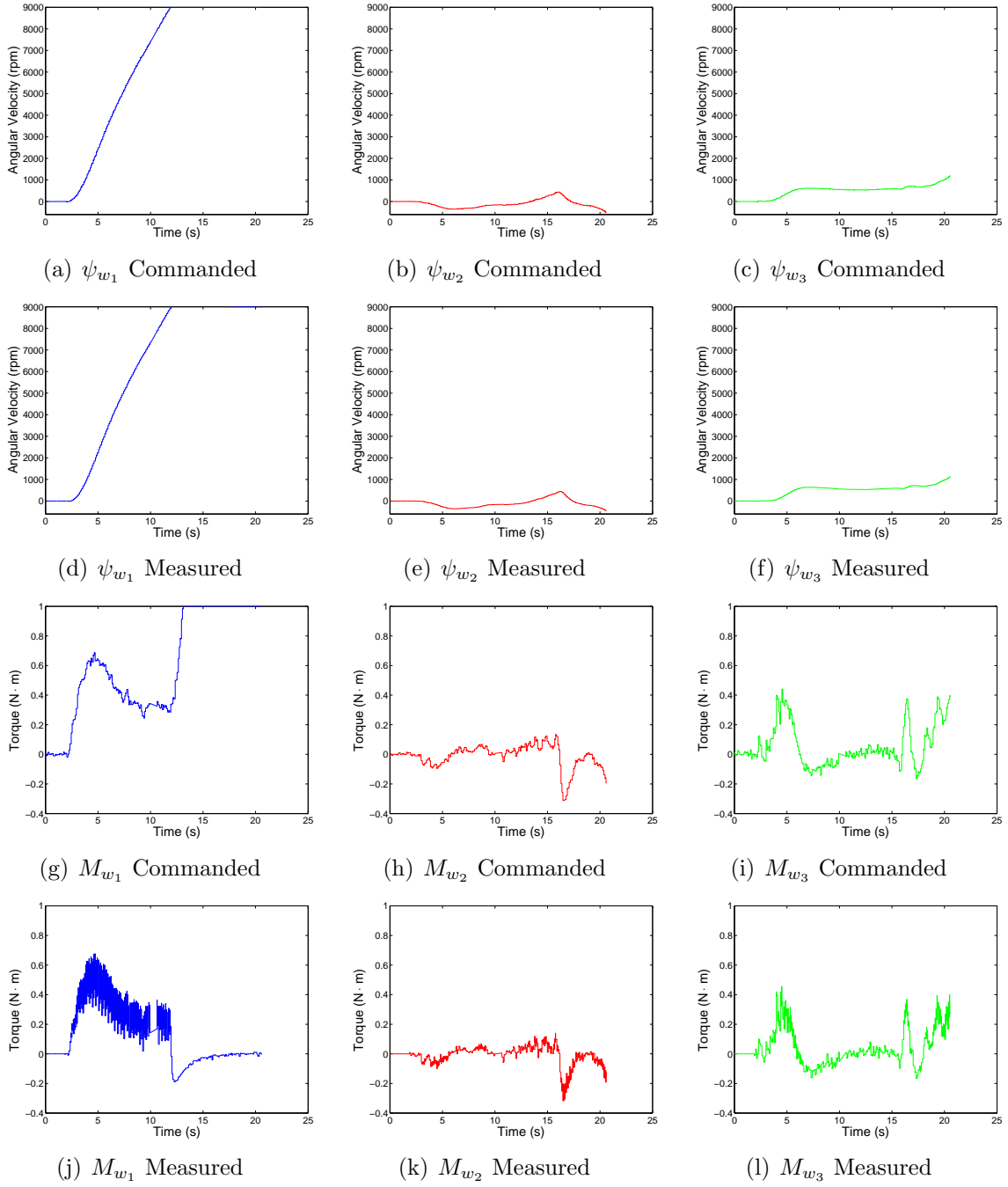


Figure B.20: Positive Torque about 1-Axis Using 40 g Mass (2 of 2)

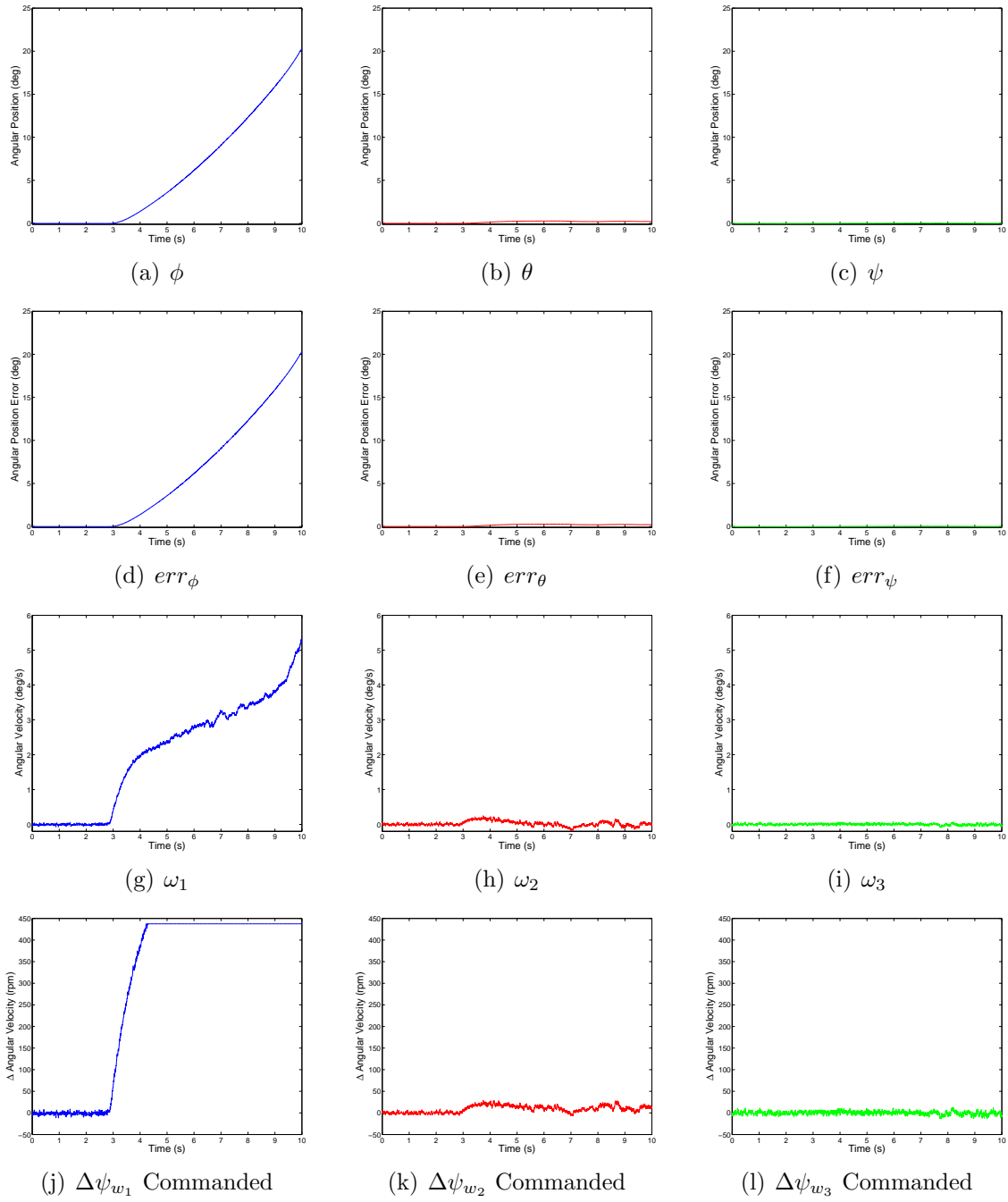
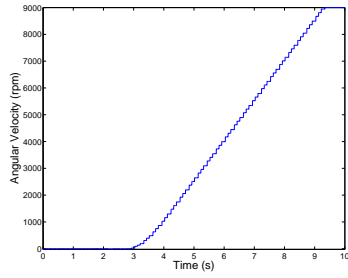
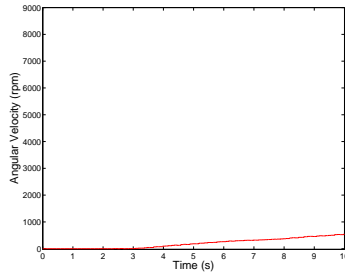


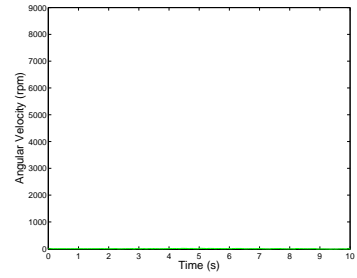
Figure B.21: Positive Torque about 1-Axis Using 75 g Mass (1 of 2)



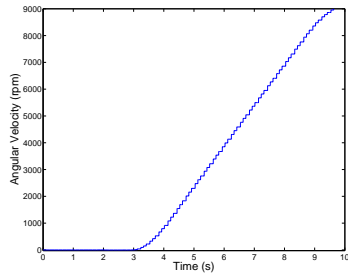
(a) ψ_{w_1} Commanded



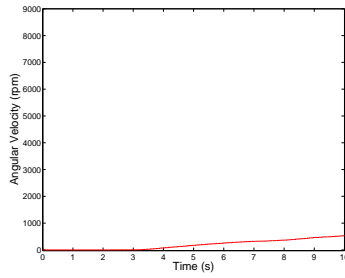
(b) ψ_{w_2} Commanded



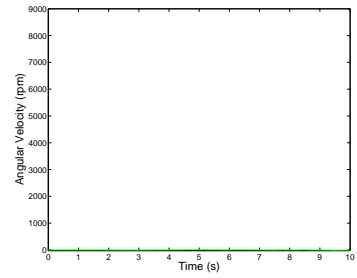
(c) ψ_{w_3} Commanded



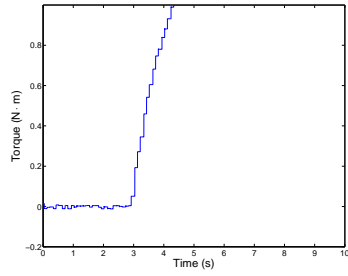
(d) ψ_{w_1} Measured



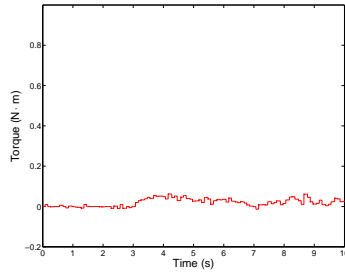
(e) ψ_{w_2} Measured



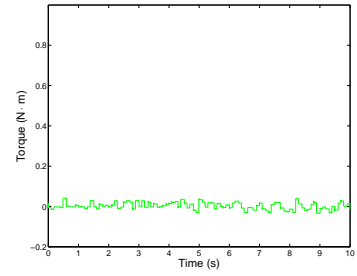
(f) ψ_{w_3} Measured



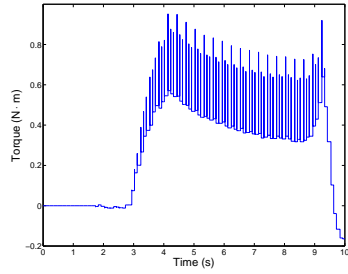
(g) M_{w_1} Commanded



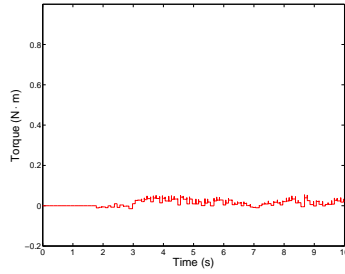
(h) M_{w_2} Commanded



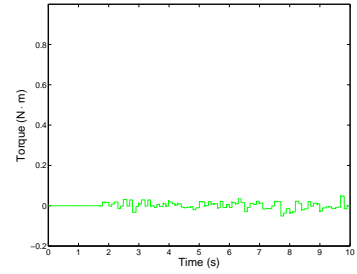
(i) M_{w_3} Commanded



(j) M_{w_1} Measured



(k) M_{w_2} Measured



(l) M_{w_3} Measured

Figure B.22: Positive Torque about 1-Axis Using 75 g Mass (2 of 2)

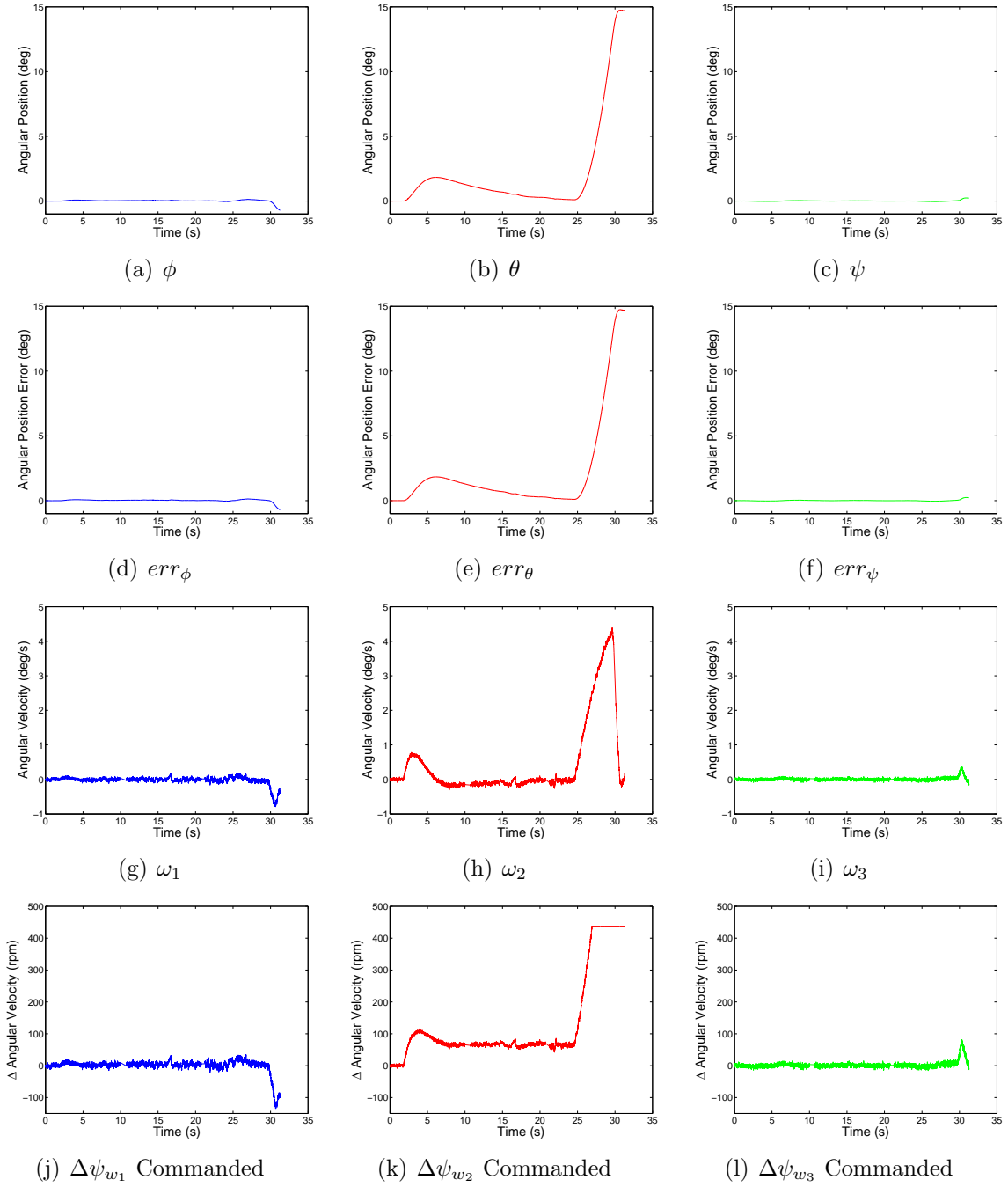


Figure B.23: Positive Torque about 2-Axis Using 20 g Mass (1 of 2)

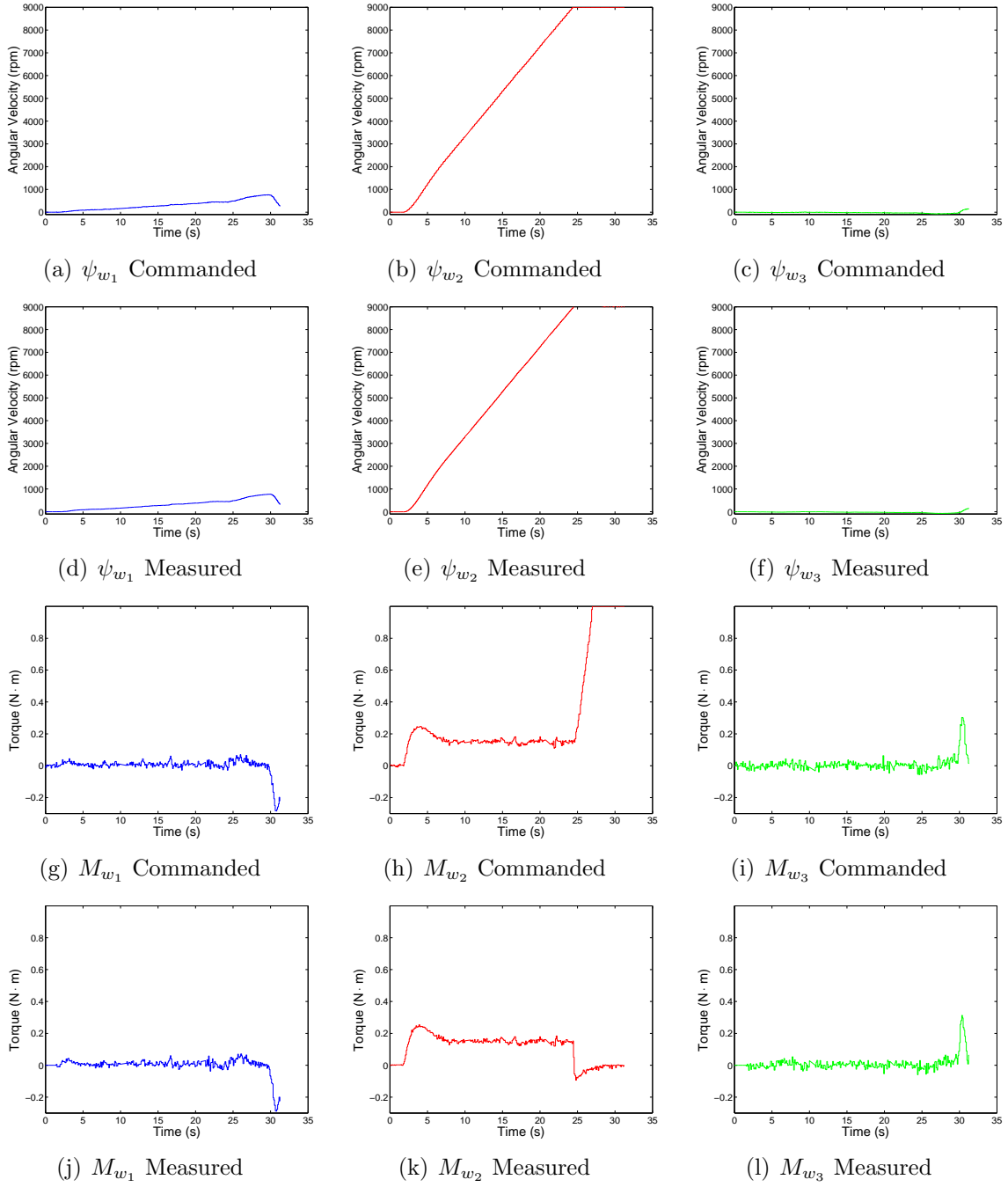


Figure B.24: Positive Torque about 2-Axis Using 20 g Mass (2 of 2)

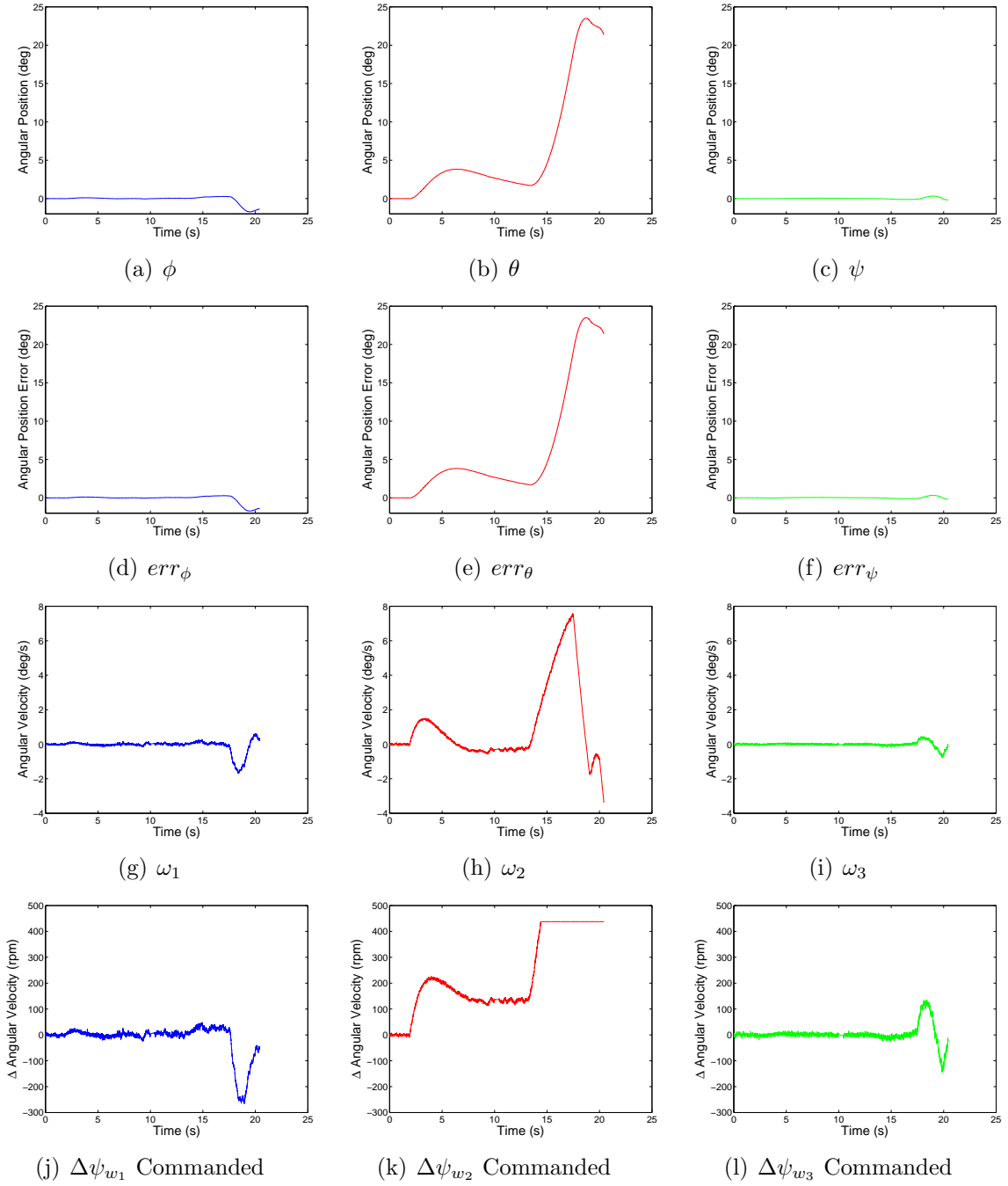


Figure B.25: Positive Torque about 2-Axis Using 40 g Mass (1 of 2)

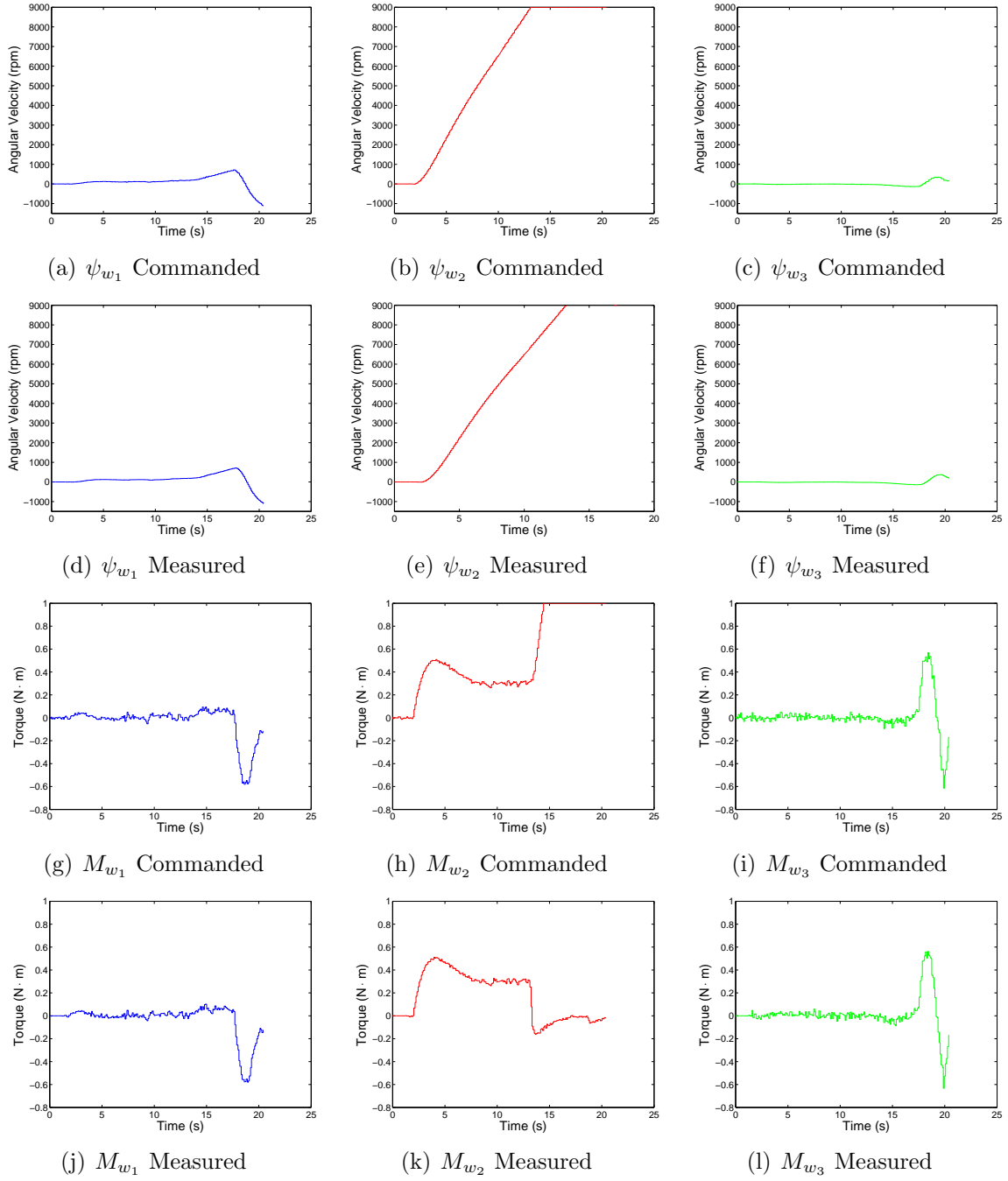


Figure B.26: Positive Torque about 2-Axis Using 40 g Mass (2 of 2)

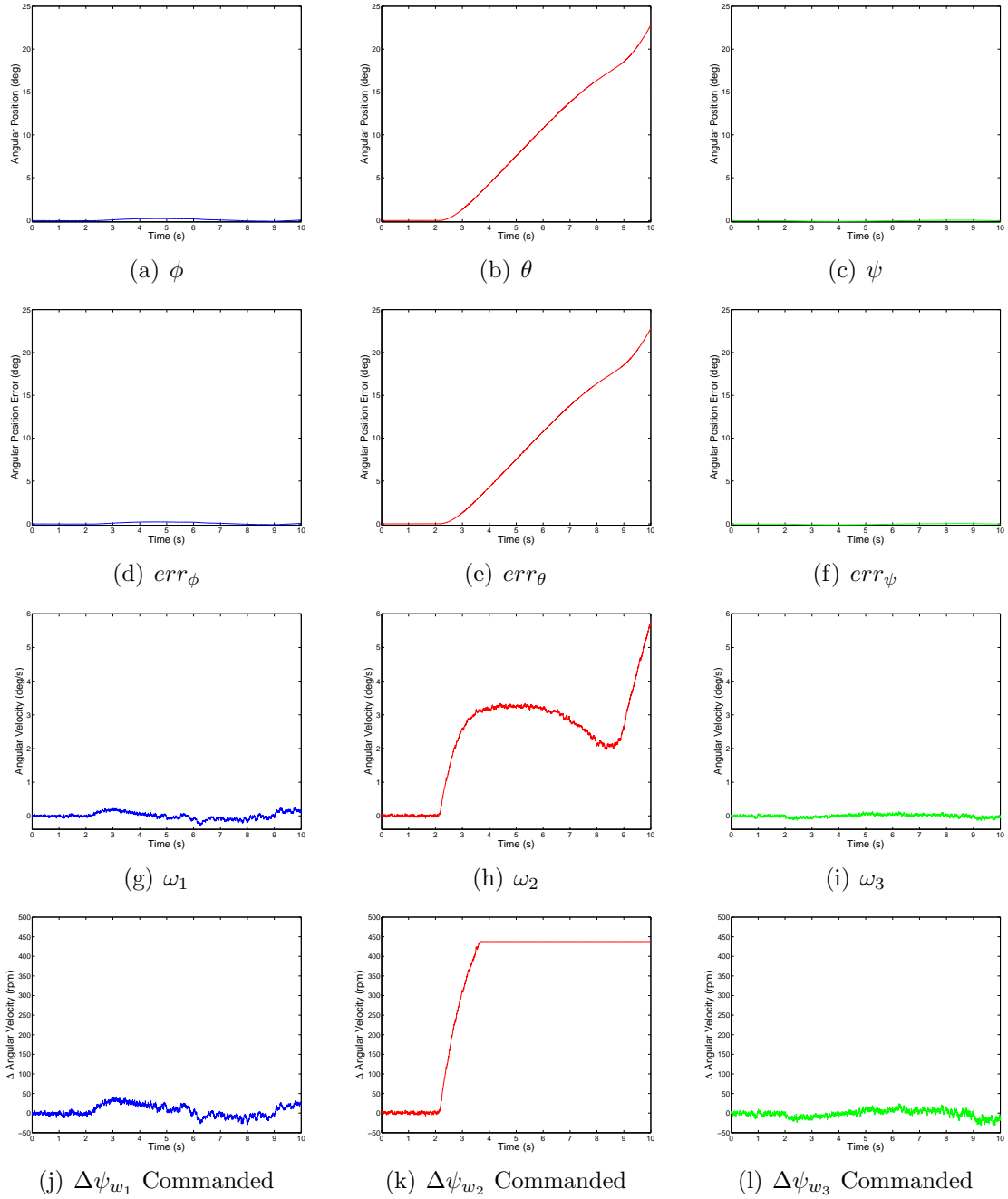


Figure B.27: Positive Torque about 2-Axis Using 75 g Mass (1 of 2)

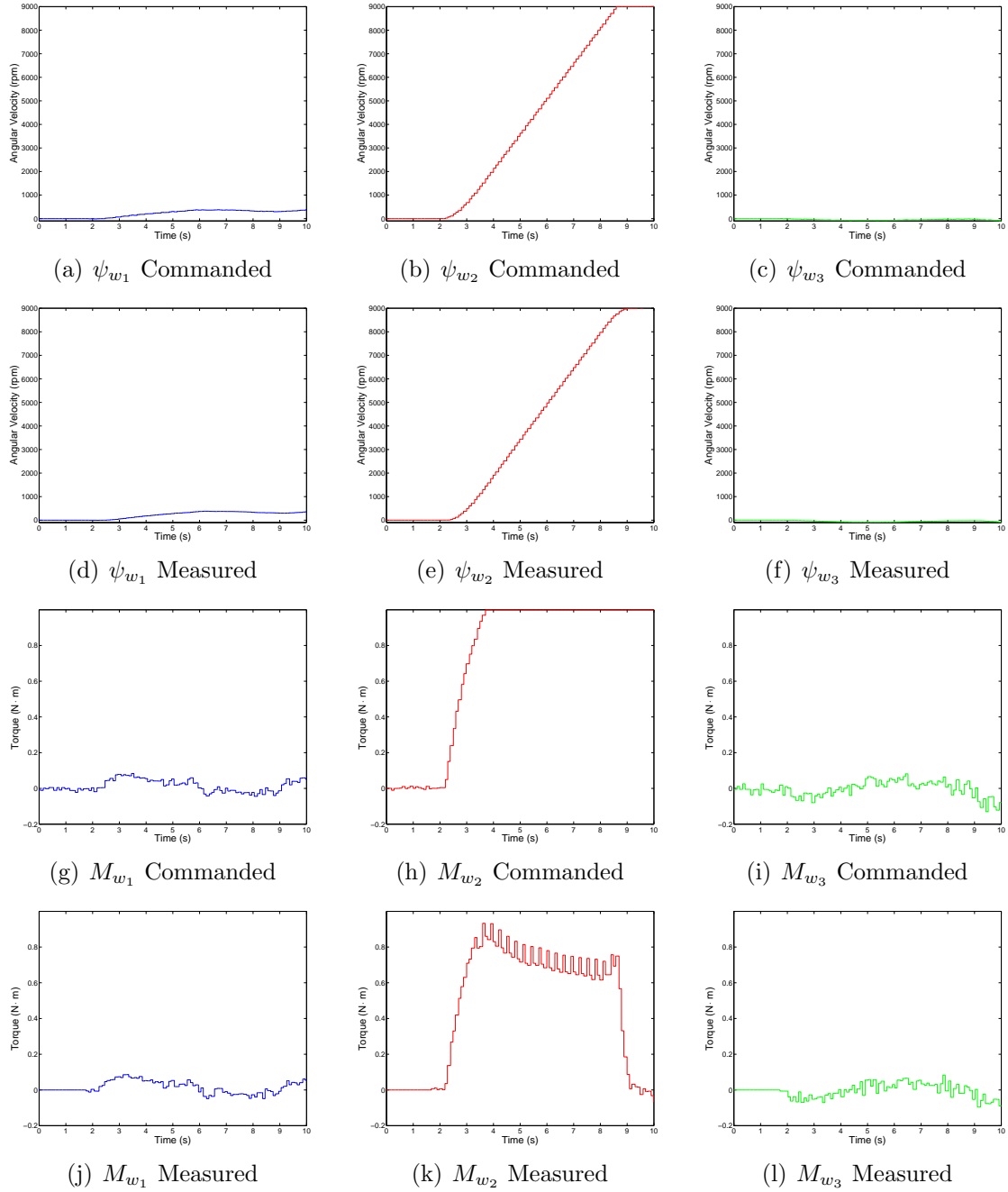


Figure B.28: Positive Torque about 2-Axis Using 75 g Mass (2 of 2)

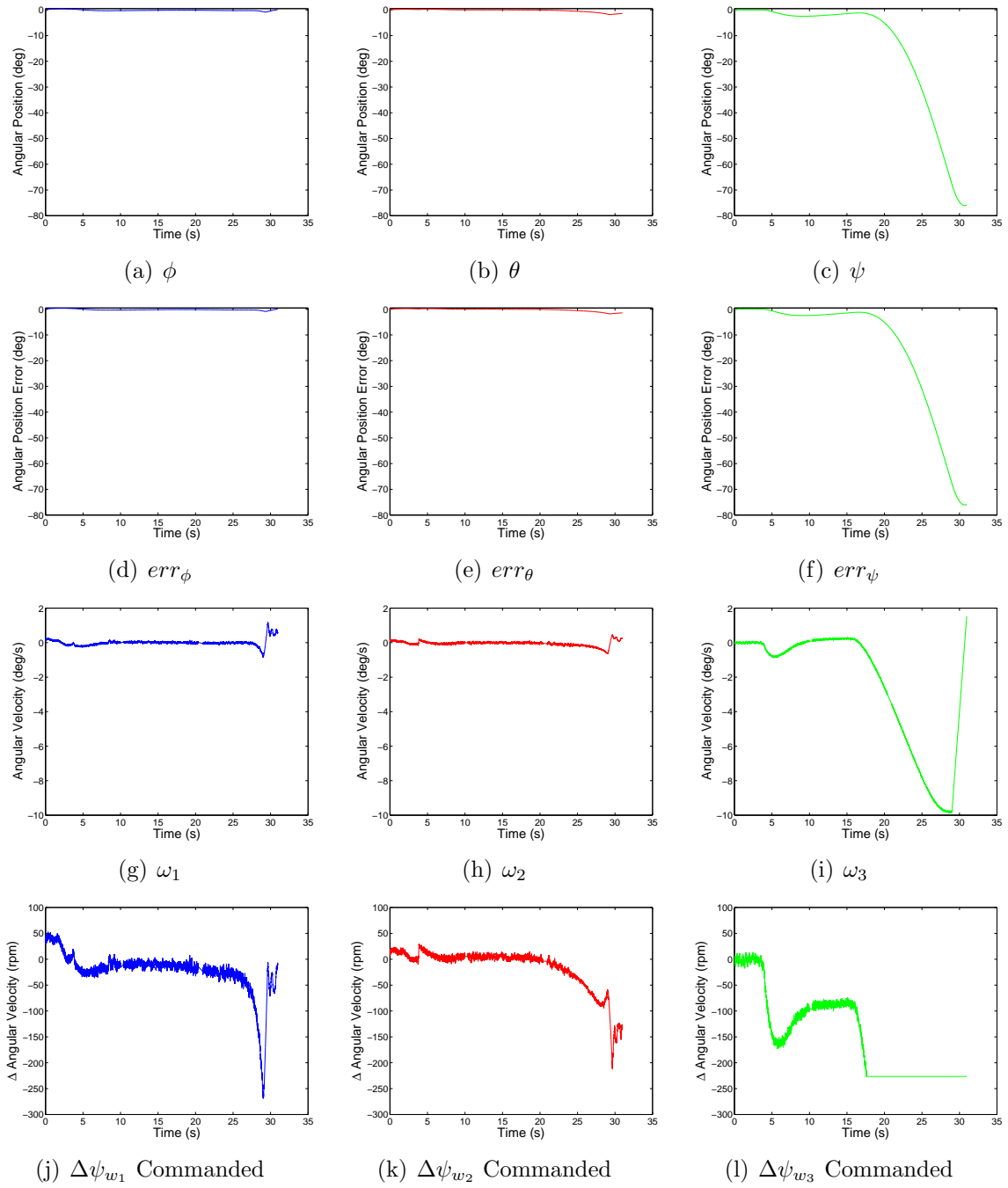


Figure B.29: Negative Torque about 3-Axis Using 50 g Mass (1 of 2)

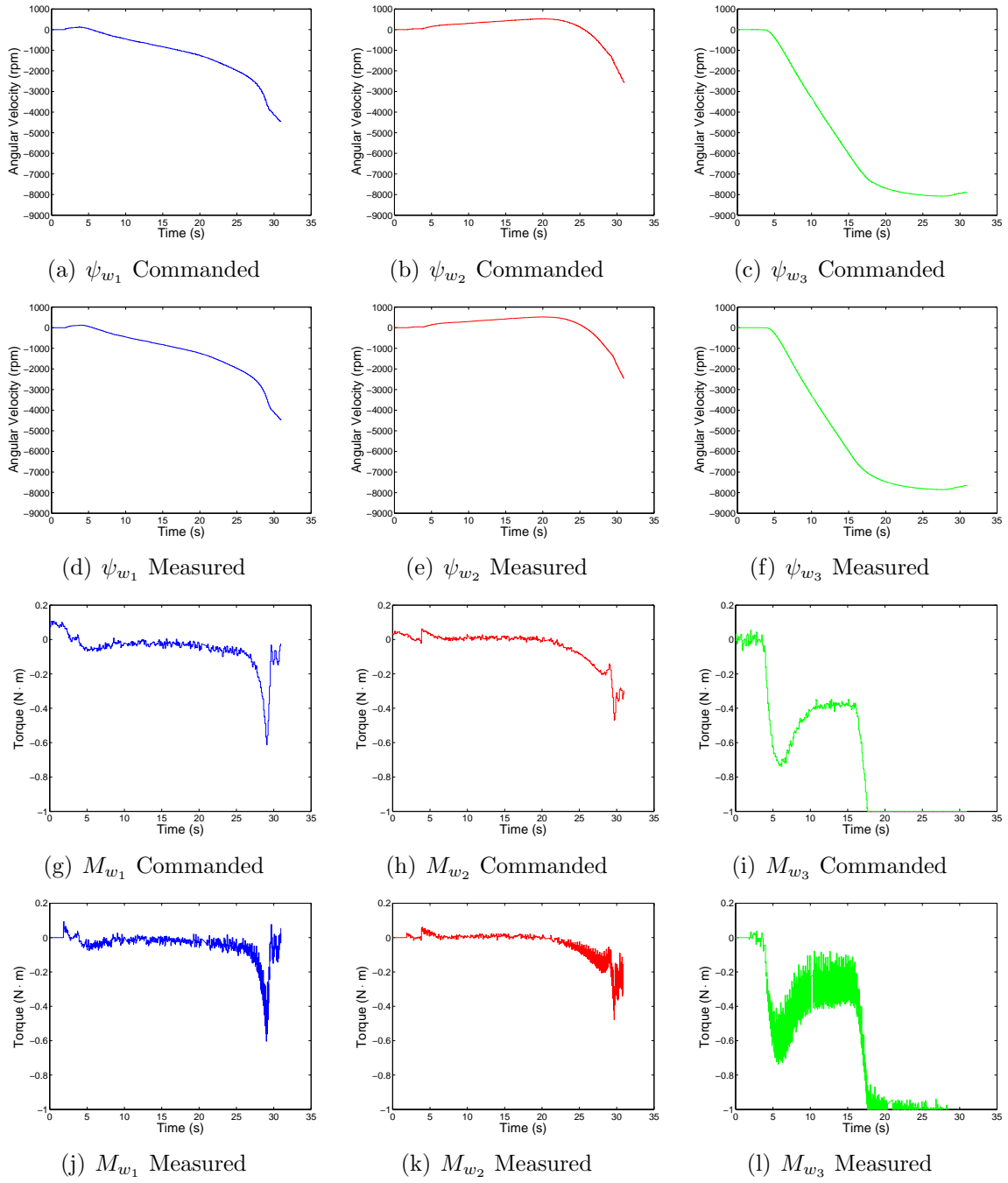


Figure B.30: Negative Torque about 3-Axis Using 50 g Mass (2 of 2)

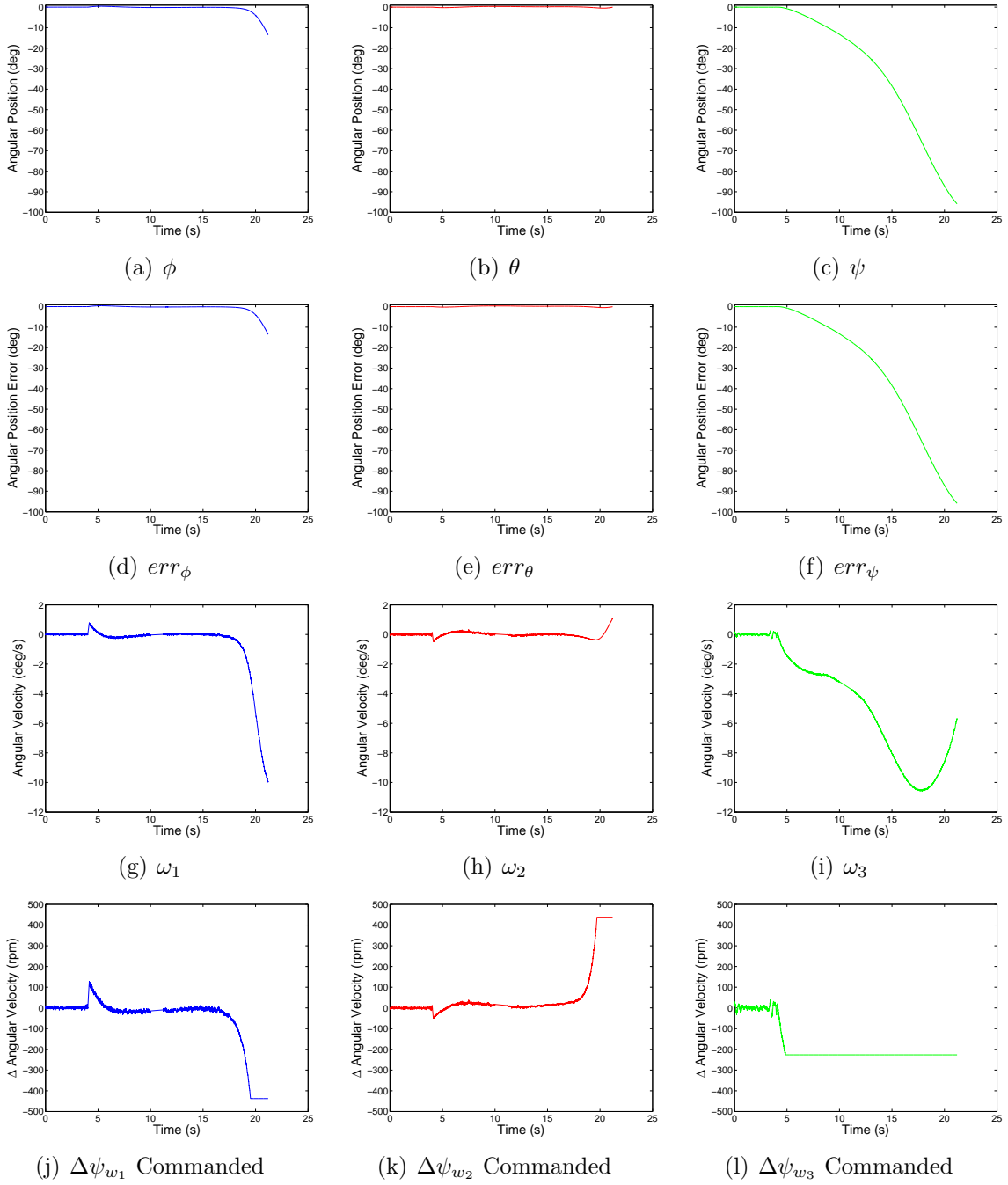


Figure B.31: Negative Torque about 3-Axis Using 100 g Mass (1 of 2)

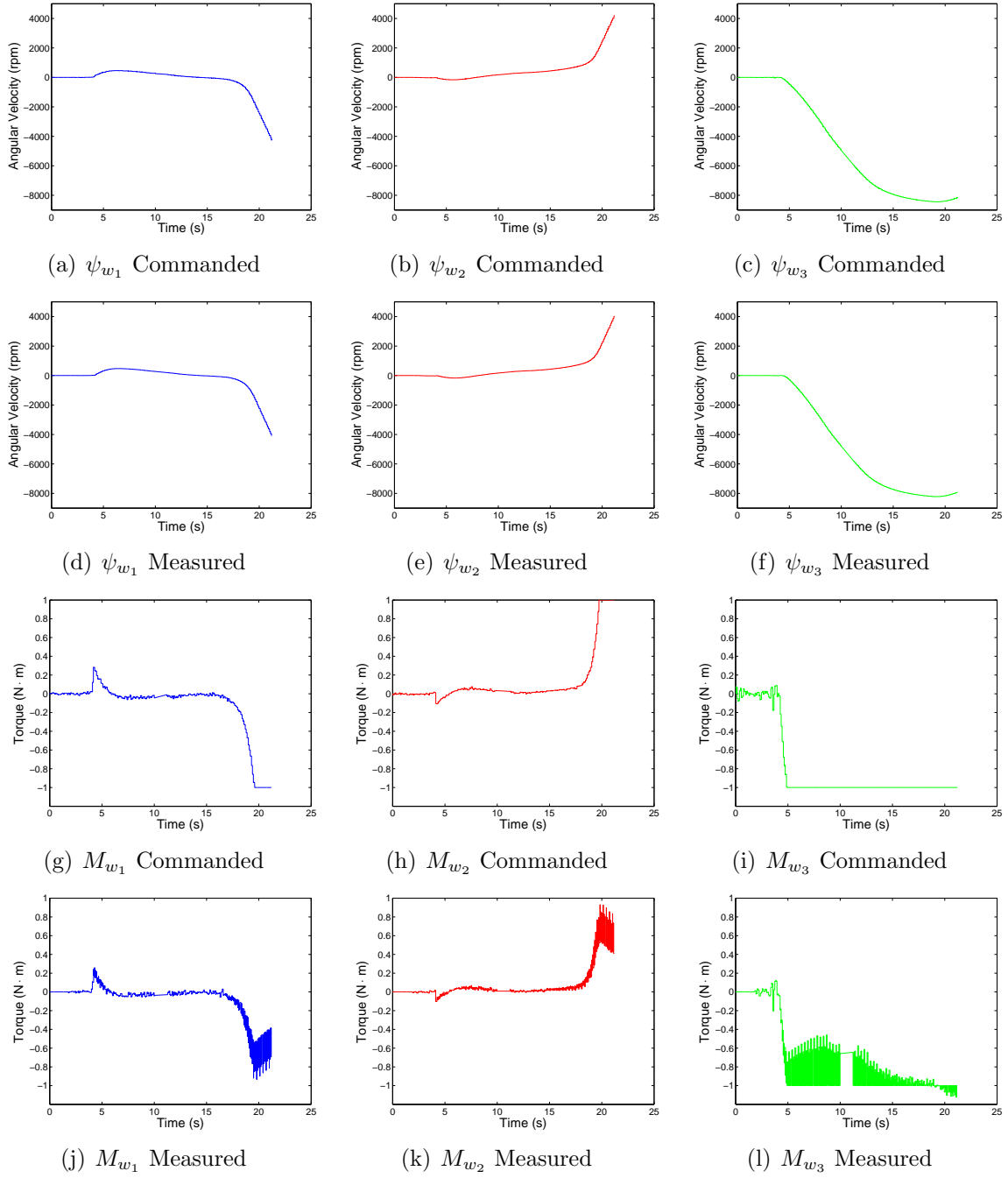


Figure B.32: Negative Torque about 3-Axis Using 100 g Mass (2 of 2)

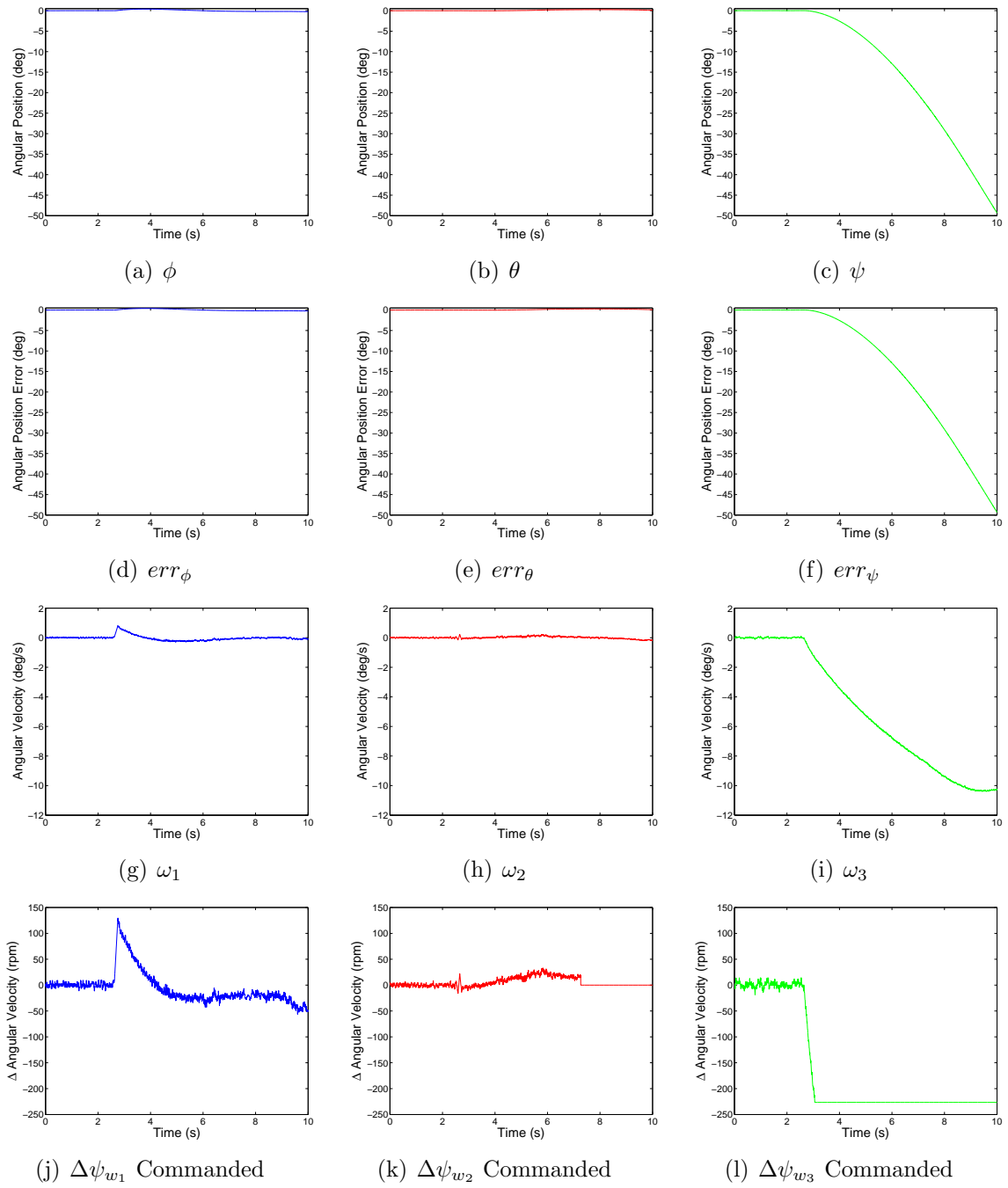


Figure B.33: Negative Torque about 3-Axis Using 145 g Mass (1 of 2)

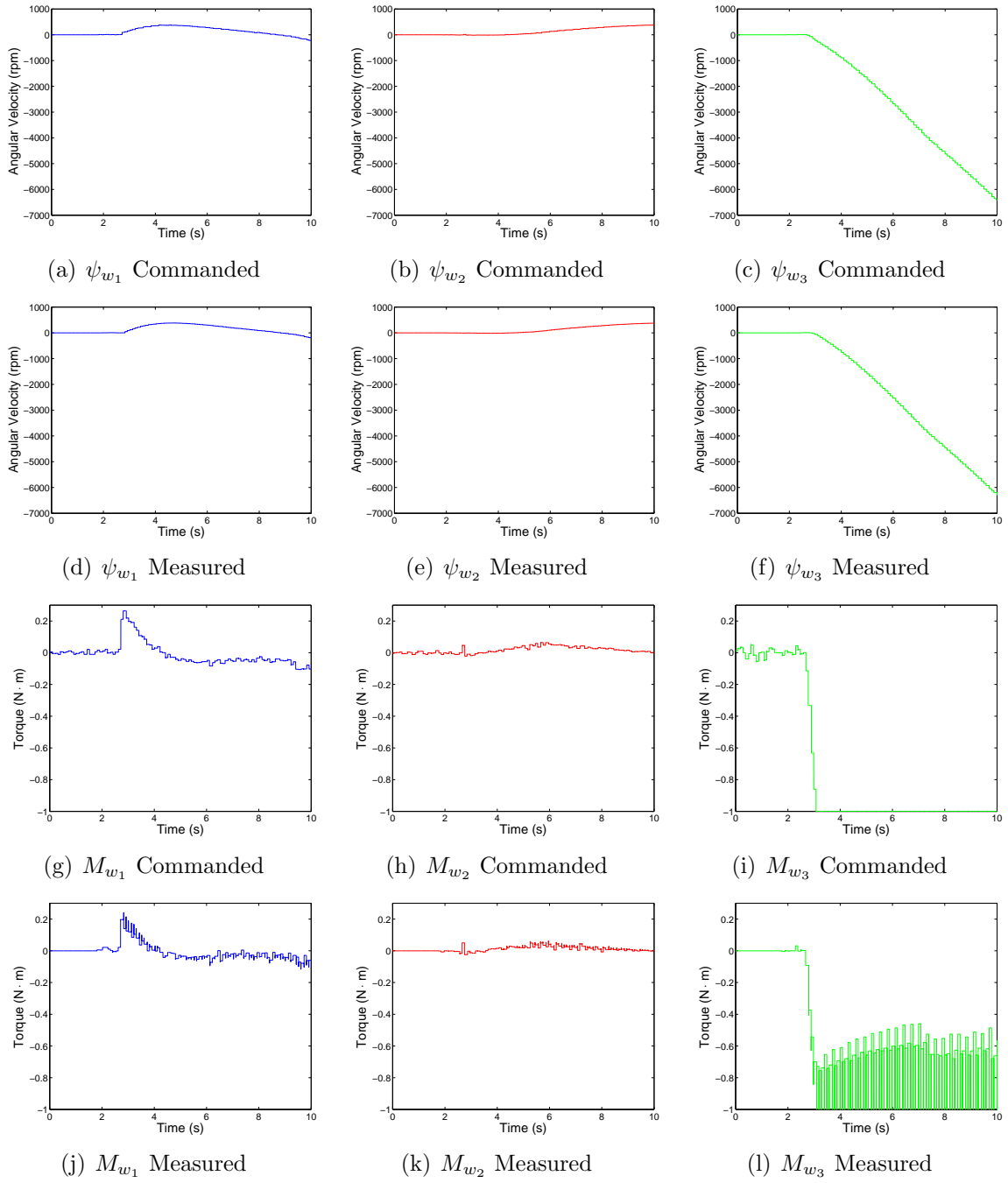


Figure B.34: Negative Torque about 3-Axis Using 145 g Mass (2 of 2)

Bibliography

1. Haim Baruh. *Analytical Dynamics*. McGraw-Hill, Inc., Boston, 1998.
2. Dennis S. Bernstein, N. Harris McClamroch, and Anthony Bloch. “Development of Air Spindle and Triaxial Air Bearing Testbeds for Spacecraft Dynamics and Control Experiments,” *Proceedings of the American Control Conference*. pages 3967–3972. American Automatic Control Council (AACC), June 2001.
3. Richard Boynton. “Using A Spherical Air Bearing to Simulate Weightlessness,” *55th Annual Conference of the Society of Allied Weight Engineers*. SAWE, June 1996.
4. Richard Boynton. “How Mass Properties Affect Spacecraft Attitude Control,” *67th Annual Conference of the Society of Allied Weight Engineers*. In *67th Annual Conference of the Society of Allied Weight Engineers*. SAWE, May 2008.
5. Richard Boynton and Kurt Wiener. “How to Calculate Mass Properties (An Engineer’s Practical Guide)”.
6. Charles D. Brown. *Elements of Spacecraft Design*. AIAA Education Series, Virginia, 2002.
7. Charles M. Close and Dean K. Frederick. *Modeling and Analysis of Dynamic Systems*. John Wiley & Sons, Inc., New York, 2nd edition, 1995.
8. James E. Colebank, Robert D. Jones, George R. Nagy, Randall D. Pollack, and Donald R. Mannebach. *SIMSAT: A Satellite System Simulator and Experimental Test Bed for Air Force Research*. MS thesis, Air Force Institute of Technology (AU), March 1999. ADA361635.
9. Vincent J. Dabrowski. *Experimental Demonstration of an Algorithm to Detect the Presence of a Parasitic Satellite*. MS thesis, Air Force Institute of Technology (AU), March 2003. (ADA413233).
10. Alok Das, Joel L. Berg, Gregory A. Norris, Derek F. Cossey, Tim J. Strange III, and Waid T. Schlaegel. “ASTREX — A Unique Test Bed for CSI Research,” *Proceedings of the 29th Conference on Decision and Control*. IEEE, December 1990.

11. Clarence W. de Silva. *Sensors and Actuators: Control Systems Instrumentation*. CRC Press, Florida, 2007.
12. dSPACE. *ControlDesk "Experiment Guide"*, Release 4.2 — March edition, 2005.
13. dSPACE. *ControlDesk "Instrument Reference"*, Release 4.2 — March edition, 2005.
14. dSPACE. *"RTI Reference" for MicroAutoBox 1401/1501, 1401/1504 and 1401/1505/1506*, Release 4.2 — March edition, 2005.
15. Leonhard Euler. "Du Mouvement de Rotations des Corps Solides Autour d'un Axe Variable". *Mémoires de l'Académie des Sciences de Berlin*, 14:154–193, 1758.
16. Gene F. Franklin, J. David Powell, and Abbas Emami-Naeini. *Feedback Control of Dynamic Systems*. Series in Electrical and Computer Engineering: Control Engineering. Addison Wesley, Massachusetts, 3rd edition, 1994.
17. David B. French. *Hybrid Control Strategies for Rapid, Large Angle Satellite Slew Maneuvers*. MS thesis, Air Force Institute of Technology (AU), March 2003. ADA412869.
18. Joseph M. Fulton. *Attitude Control and Multimedia Representation of Air Force Institute of Technology's (AFIT'S) Simulation Satellite (SIMSAT)*. MS thesis, Air Force Institute of Technology (AU), March 2000. ADA380275.
19. Jason W. Geitgey. *The Determination of Remaining Satellite Propellant Using Measured Moments of Inertia*. MS thesis, Air Force Institute of Technology (AU), June 2006. ADA453964.
20. Michael D. Griffin and James R. French. *Space Vehicle Design*. AIAA Education Series, Virginia, 2nd edition, 2004.
21. Michael S. Hines. *Fuel Estimation Using Dynamic Response*. MS thesis, Air Force Institute of Technology (AU), March 2007. ADA469309.
22. ByungMoon Kim, Efstathios Velenis, Patrick Kriengsire, and Tsiotras Panagiotis. *Designing a low-cost spacecraft simulator*, August 2003.

23. ByungMoon Kim, Efstathios Velenis, Patrick. Kriengsiri, and Panagiotis Tsiotras. "A Spacecraft Simulator for Research and Education," *Astrodynamics Specialists Conference*. pages 897–914. AIAA/AAS, July 2001.
24. Matthew B. Kimsal. *Design of a Space-Borne Autonomous Infrared Tracking System*. MS thesis, Air Force Institute of Technology (AU), March 2004. ADA425222.
25. Jack B. Kuipers. *Quaternions and Rotation Sequences*. Princeton University Press, New Jersey, 1999.
26. Saburo Matunaga, Keisuke Yoshihara, Takashi Takahashi, Shingo Tsurumi, and Ky-oichi ui. "Ground Experiment System for Dual-Manipulator-Based Capture of Damaged Satellites," *Proceedings of the IEEE International Conference on Intelligent Robots and Systems*. pages 1847–1852, 2000.
27. Maxon Motor. *EPOS Positioning Controller "Application Note 'CANopen Basic Information'"*, February edition, 2006.
28. Maxon Motor. *EPOS 70/10 "Getting Started"*, december edition, 2008.
29. Maxon Motor. *Maxon DC Motor and Maxon EC Motor "Key Information"*, May edition, 2009.
30. Maxon Motor. *Maxon EC 45 Order Number 136211 "Catalog Page"*, May edition, 2009.
31. Maxon Motor. *Maxon EPOS 70/10 Order Number 300583 "Catalog Page"*, may edition, 2009.
32. Maxon Motor. *Maxon HEDL 9140 Order Number 137959 "Catalog Page"*, may edition, 2009.
33. C. Douglas McFarland. *Near Real-Time Closed-Loop Optimal Control Feedback for Spacecraft Attitude Maneuvers*. MS thesis, Air Force Institute of Technology (AU), March 2009. ADA496781.
34. Katsuhiko Ogata. *Modern Control Engineering*. Prentice-Hall, New Jersey, 4th edition, 2002.
35. Biren Patel. RE: Mechanical Damping of the Rotor. [Received 2 Nov 09].

36. Biren Patel. RE: Tuning. [Received 17 Nov 09].
37. Mason A. Peck and Andrew R. Cavender. “An Airbearing-Based Testbed for Momentum-Control Systems and Spacecraft Line of Sight,” *Proceedings of the 13th AAS/AIAA Space Flight Mechanics Meeting*. AAS/AIAA, February 2003.
38. Burke Pond and Inna Sharf. “Experimental Demonstration of Flexible Manipulator Trajectory Optimization,” *Proceedings of the AIAA Guidance, Navigation, and Control Conference and Exhibit*. pages 1869–1876, 1999.
39. R. J. Richards. *An Introduction to Dynamics and Control*. Longman, London, 1979.
40. Neal R. Roach, Wayne C. Rohe, and Nathan F. Welty. *A Systems Engineering Approach to the Design of a Spacecraft Dynamics and Control Testbed*. MS thesis, Air Force Institute of Technology (AU), March 2008.
41. Marcello Romano and Brij N. Agrawal. “Acquisition, Tracking and Pointing Control of the Bifocal Relay Mirror Spacecraft”. *International Astronautical Federation Congress*, 53:509–519, October 2002.
42. George Sagnac. “Sur la Preuve de la Réalité de l’Ether Lumineux par l’Expérience de l’Interférographe Tournant”. *Comptes Rendus*, 157:1410–1413, December 1913.
43. H. C. Schubert and J. P. How. “Space Construction: an Experimental Testbed to Develop Enabling Technologies,” *Proceedings of the Conference on Telem manipulator and Telepresence Technologies IV*. pages 179–188, 1997.
44. Jana L. Schwartz and Christopher D. Hall. “The Distributed Spacecraft Attitude Control System Simulator: Development, Progress, Plans,” *Proceedings of the Flight Mechanics Symposium*. NASA, October 2003.
45. Jana L. Schwartz, Mason A. Peck, and Christopher D. Hall. “Historical Review of Spacecraft Simulators”. *Journal of Guidance, Control, and Dynamics*, 26(4):513–522, 2003.
46. Jerry J. Sellers. *Understanding Space: An Introduction to Astronautics*. The McGraw-Hill Companies, Inc., New York, 3rd edition, 2005.

47. Raymond A. Serway. *Physics For Scientists and Engineers*, volume 1. Saunders College, 4th edition, 1996.
48. Marcel J. Sidi. *Spacecraft Dynamics and Control*. Cambridge Aerospace Series 7. Cambridge University Press, Cambridge, 1997.
49. Jason E. Smith. *Attitude Model of a Reaction Wheel/Fixed Thruster Based Satellite Using Telemetry Data*. MS thesis, Air Force Institute of Technology (AU), March 2005. ADA437523.
50. John F. Wakerly. *Digital Design Principles and Practices*. Prentice-Hall, New Jersey, 2nd edition, 1994.
51. Bong Wie. *Space Vehicle Dynamics and Control*. AIAA Education Series, Virginia, 2nd edition, 2008.
52. William E. Wiesel. *Spaceflight Dynamics*. McGraw-Hill, 2nd edition, 1995.
53. John G. Ziegler and Nathaniel B. Nichols. “Optimum Settings for Automatic Controllers”. *Transactions of the ASME*, 64:759–768, 1942.

REPORT DOCUMENTATION PAGE			Form Approved OMB No. 0704-0188	
The public reporting burden for this collection of information is estimated to average 1 hour per response, including the time for reviewing instructions, searching existing data sources, gathering and maintaining the data needed, and completing and reviewing the collection of information. Send comments regarding this burden estimate or any other aspect of this collection of information, including suggestions for reducing this burden to Department of Defense, Washington Headquarters Services, Directorate for Information Operations and Reports (0704-0188), 1215 Jefferson Davis Highway, Suite 1204, Arlington, VA 22202-4302. Respondents should be aware that notwithstanding any other provision of law, no person shall be subject to any penalty for failing to comply with a collection of information if it does not display a currently valid OMB control number. PLEASE DO NOT RETURN YOUR FORM TO THE ABOVE ADDRESS.				
1. REPORT DATE (DD-MM-YYYY) 25-03-2010		2. REPORT TYPE Master's Thesis		3. DATES COVERED (From — To) Sep 2009 – Mar 2010
4. TITLE AND SUBTITLE Attitude Control of a Satellite Simulator Using Reaction Wheels and a PID Controller			5a. CONTRACT NUMBER	
			5b. GRANT NUMBER	
			5c. PROGRAM ELEMENT NUMBER	
6. AUTHOR(S) Snider, Ryan, E., Captain, USAF			5d. PROJECT NUMBER	
			5e. TASK NUMBER	
			5f. WORK UNIT NUMBER	
7. PERFORMING ORGANIZATION NAME(S) AND ADDRESS(ES) Air Force Institute of Technology Graduate School of Engineering and Management (AFIT/ENY) 2950 Hobson Way WPAFB OH 45433-7765			8. PERFORMING ORGANIZATION REPORT NUMBER AFIT/GAE/ENY/10-M24	
9. SPONSORING / MONITORING AGENCY NAME(S) AND ADDRESS(ES) AFRL/RVSV Attn: GN&C Group 3550 Aberdeen Avenue SE Bldg 472 Kirtland AFB NM 87117			10. SPONSOR/MONITOR'S ACRONYM(S)	
			11. SPONSOR/MONITOR'S REPORT NUMBER(S)	
12. DISTRIBUTION / AVAILABILITY STATEMENT APPROVED FOR PUBLIC RELEASE; DISTRIBUTION UNLIMITED				
13. SUPPLEMENTARY NOTES				
14. ABSTRACT Attitude requirements of a satellite are determined by its mission: telecommunications, optical imagery, and meteorology to name a few. A satellite's ability to orient its mission critical hardware (solar arrays, attitude sensors, etc.), as well as its mission specific payload, is incumbent upon the performance of the satellite's attitude control system (ACS). For a highly accurate ACS and for moderately fast maneuverability, reaction wheels are preferred because they allow continuous and smooth control while inducing the smallest possible disturbance torques. The objective of this research is to design, build, test, and evaluate the performance of a reaction wheel ACS on-board the Air Force Institute of Technology's (AFIT) second-generation satellite simulator, SimSat II. The reaction wheel ACS is evaluated against performance measures set forth by AFIT faculty; specifically, the ability to perform rest-to-rest maneuvers and withstand worst case disturbance torques. In all, the reaction wheel ACS proves it is capable of performing rest-to-rest maneuvers and withstanding disturbance torques. However, results conclude that theoretical predicted performance is unattainable. The performance of the reaction wheel ACS hinges upon its ability to command the reaction wheels at fixed interval timing. The inability of the test bed to execute fixed interval timing caused performance degradation.				
15. SUBJECT TERMS Attitude Control, Satellite Simulator, Reaction Wheels, PID Controller				
16. SECURITY CLASSIFICATION OF:			17. LIMITATION OF ABSTRACT UU	18. NUMBER OF PAGES 166
a. REPORT U	b. ABSTRACT U	c. THIS PAGE U		
			19a. NAME OF RESPONSIBLE PERSON Eric D. Swenson, Lt Col, USAF (ENY)	
			19b. TELEPHONE NUMBER (Include Area Code) (937) 255-3636, ext 7479; e-mail: eric.swenson@afit.edu	